Alma Mater Studiorum - Università di Bologna

DOTTORATO DI RICERCA IN

FISICA

Ciclo 35

Settore Concorsuale: 02/B1 - FISICA SPERIMENTALE DELLA MATERIA

Settore Scientifico Disciplinare: FIS/03 - FISICA DELLA MATERIA

OPTOELECTRONIC INVESTIGATION OF DEFECTS IN HYBRID METAL HALIDE PEROVSKITES

Presentata da: Giovanni Armaroli

Coordinatore Dottorato	**Supervisore**
Michele Cicoli	Daniela Cavalcoli

Esame finale anno 2023

Abstract

The growing demand for flexible and low-cost electronics has driven research towards the study of novel semiconducting materials to replace traditional semiconductors like silicon and germanium, which are limited by mechanical rigidity and high production cost. Some of the most promising semiconductors in this sense are metal halide perovskites (MHPs), which combine low-cost fabrication and solution processability with exceptional optoelectronic properties like high absorption coefficient, long charge carrier lifetime, and high mobility. These properties, combined with an impressive effort by many research groups around the world, have enabled the fabrication of solar cells with record-breaking efficiencies, and photodetectors with better performance than commercial ones. However, MHP devices are still affected by issues that are hindering their commercialization, such as degradation under humidity and illumination, ion migration, electronic defects, and limited resistance to mechanical stress. The aim of this thesis work is the experimental characterization of these phenomena. We investigated the effects of several factors, such as X-ray irradiation, exposure to environmental gases, and atmosphere during synthesis, on the optoelectronic properties of MHP single crystals. We achieved this by means of optical spectroscopy, electrical measurements, and chemical analyses. We identified the cause of mechanical delamination in MHP/silicon tandem solar cells by atomic force microscopy measurements. We characterized electronic defects and ion migration in MHP single crystals by applying for the first time the photo-induced current transient spectroscopy technique to this class of materials. This research allowed to gain insight into both intrinsic defects, like ion migration and electron trapping, and extrinsic defects, induced by X-ray irradiation, mechanical stress, and exposure to humidity. This research paves the way to the development of methods that heal and passivate these defects, enabling improved performance and stability of MHP optoelectronic devices.

Table of Contents

Introduction

Semiconductor devices are nowadays ubiquitous, playing a crucial role in our daily lives. Some of their most relevant applications include renewable energy generation, sensing, lighting, telecommunications, and consumer electronics. Currently, the most commonly employed semiconductors are inorganic materials such as silicon, germanium, gallium arsenide, and cadmium telluride. These materials provide stable and reliable performance, and their high cost of production has decreased over the years, thanks to the economy of scale. Nonetheless, they are still affected by some limitations. One of them is their limited mechanical flexibility. Inorganic semiconductors are rigid and brittle, and therefore unsuitable for being used in flexible electronics to produce, for instance, roll-up displays and wearable devices, which are increasingly in demand on the market. Another relevant limitation is their high cost of production. Despite the decrease in their manufacturing cost over the years, the processes needed for inorganic semiconductor production are inherently expensive in terms of energy use. In particular, they require high temperatures and high vacuum, which inevitably increase production cost.

These limitations have pushed both academic and industrial research towards the study of new semiconducting materials. Organic semiconductors have been found to provide a valid alternative to inorganic ones for specific applications, such as lighting, currently produced by light emitting diodes (LEDs). Organic LEDs (OLEDs) can be found nowadays in a variety of consumer electronic devices. Their organic nature also provides the possibility of creating flexible devices, such as LED displays. However, these materials are not achieving the same success in other important applications, like solar cells and photodetectors. Indeed, the maximum efficiency achieved by organic photovoltaics is still below 20% as of year 2022,[1] and organic detectors are afflicted by slow response times.[2]

Since the publication of two seminal papers in 2012,[3,4] a new field of research on hybrid organic-inorganic semiconductors has been growing at a rapid pace. In particular, researchers are focussing on hybrid metal halide perovskites (MHPs), which demonstrated outstanding performances in all sorts of optoelectronic devices where they were employed. These materials combine the simple and low-cost fabrication process of organic semiconductors, while maintaining remarkable photophysical properties, comparable to inorganic semiconductors, such as high mobility and long lifetime of charge carriers, and large absorption coefficient.[5,6] The main driving force for research and development on these materials is photovoltaics. As of year 2022, perovskite solar cells have reached 25.7% efficiency, and perovskite/silicon tandem solar cells have achieved 32.5% efficiency,[1] making MHPs the most promising semiconductors for next generation solar cells. However, their success is not limited to solar energy production, but extends to, LEDs,[7] lasers,[8] and photodetectors.[2,9] In particular, the latter application has seen a growing interest from the scientific community, as MHPs have demonstrated exceptional UV-Visible, X- and γ-ray detection performance.[2,6,10]

Despite this large technological success, MHP-based devices are still affected by issues that are hindering their commercialization. MHPs are highly reactive to water and oxygen molecules in the atmosphere,[11,12] leading to device instability and long term degradation when operated in air. Another source of instability is ion migration, which is active at room temperature for most MHP materials.[13] Moving ions cause hysteresis in the electrical characteristics of solar cells, slow down the response time to optoelectronic stimuli, and eventually lead to material degradation.[14] Scientists have already found ways to partially limit both issues, by engineering encapsulation techniques to protect MHPs from air molecules,[15] and by finding formulations and interlayer materials that hinder ion migration as much as possible.[16] However, achieving stable and market-ready optoelectronic devices based on MHPs still needs further efforts in research and development.

This thesis work focusses on the characterization of defects in MHP materials. The aim is achieving a better understanding of the physical and chemical processes that are currently hindering performance of MHP devices, causing degradation and instability. In Chapter 1, I discuss the main chemical and physical properties of MHPs, as well as their most relevant fields of application. In Chapter 2, I report the experimental methods followed during my work, describing the synthesis procedures, experimental setups, and data analysis methods. Chapter 3 contains the main experimental results achieved in this thesis work, which I briefly summarize here:

- Study of the effect of ionizing radiation on the photophysical properties of MHP single crystals.

- Identification of the weak interface causing delamination in perovskite/silicon tandem solar cells.
- Characterization of electronic defects and ion migration in 2-dimensional and 3-dimensional MHP single crystals by means of Photoinduced Current Transient Spectroscopy (PICTS).
- Study on the effect of environmental gases on electronic and ionic phenomena in MHP single crystals.
- Investigation of the impact of atmosphere during growth of MHP single crystals on their chemical and optoelectronic properties.

This work led to the publication of two scientific papers,[17,18] and two other manuscripts are currently in preparation. The work was carried out at the Department of Physics and Astronomy of the University of Bologna, and at the Insitut Néel and CEA of Grenoble, France.

Chapter 1

Properties and applications of metal halide perovskites

Metal halide perovskites (MHPs) are semiconducting materials that have proven to be excellent active layers for optoelectronic devices like solar cells, detectors, LEDs, and X-ray scintillators. Their high performances are complemented by the simple and low-cost fabrication process with respect to conventional semiconductors. This chapter provides a summary of MHPs state of the art, based on recent literature results. Sections 1.1 and 1.2 describe the structural and opto-electronic of metal halide perovskite. Sections 1.3 and 1.4 describe two of the main problems that affect MHPs, i.e., degradation and defects. Section 1.5 is a brief overview of their main applications in optoelectronic devices.

1.1 Structural properties

1.1.1 Crystal structure

Metal halide perovskites (MHPs) are a class of ionic materials with crystal structure AMX_3, where A is a monovalent cation, M is a divalent metallic cation, and X is a halogen monovalent anion. The unit cell is schematically represented in **Figure 1.1**. It is characterized by a $[MX_6]^{4-}$ octahedron, with the M atom at its core, surrounded by a cage of A atoms. The structure was found by Goldshmidt[19] to be stable only when $0.8 < t < 1$, where t is the Goldshmidt tolerance factor, defined as

$$t = \frac{r_A + r_X}{\sqrt{2}\,(r_B + r_X)} \tag{1.1}$$

where r_A, r_B, and r_X are the radii of the A, B, and X ions, respectively. Given the Goldschmidt rule, the large radii of the halogen anions (I^-, Br^-, or Cl^-) introduce strict constraints on the choice of A and B to form a MHP structure. Therefore, MHPs naturally form only with a small set of chemical elements. This is in contrast with the oxide perovskites (chemical formula ABO_3), where the smaller radius of the oxygen anion O_2^- allows for a broader choice of A and B ions.

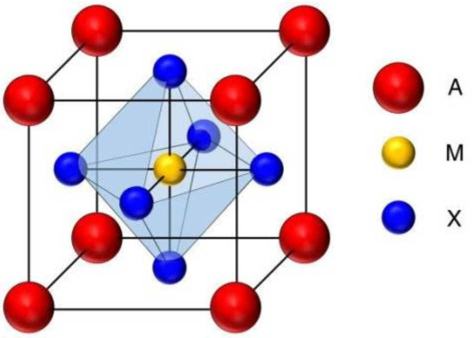

Figure 1.1 Crystal structure of a metal halide perovskite. A is the cation, M is the metallic atom, and X is the halogen anion. Image from ref.[20].

To date, only three A site cations were found to produce a stable MHP structure: Cs^+, $CH_3NH_3^+$ (i.e., methylammonium, MA), and $HC(NH_2)_2^+$ (i.e., formamidinium, FA). Cs is the only element in the first group of the periodic table that is large enough to sustain the perovskite structure, while MA and FA are the only organic cations that have a suitable size and charge distribution.[21] Cs-based MHPs are usually referred to as inorganic MHPs, while MA- and FA-based MHPs are named as *hybrid* metal halide perovskites, referring to their organic-inorganic nature. The use of bigger organic cations with respect to MA and FA, i.e., with a tolerance factor $t > 1$, leads to the formation of low-dimensional perovskites, as will be discussed in the following section.

The M metal in MHPs can be selected among alkaline earths, bivalent rare earths, and the heavier elements in the 14th group of the periodic table, i.e., Ge^{2+}, Sn^{2+}, and Pb^{2+}.[21] MHPs based on the latter three M elements are by far the most commonly studied. Among Ge, Sn, and Pb, the latter is notoriously the one that yields the most environmentally stable perovskite structure. Indeed, Ge and Sn have a higher tendency at oxidizing with respect to Pb, and thus at producing Ge and Sn vacancies, that eventually lead to material degradation.[22] For this reason, at the moment the most promising MHPs for real-life applications are Pb-based, although the concern about Pb toxicity is driving research towards enhancing the stability of Pb-free MHPs. The experimental results presented in this thesis work are entirely on Pb-based perovskites, therefore also this chapter will focus mainly on properties and applications of Pb-based perovskites.

1.1.2 Low-dimensional perovskites

When Cs, MA, and FA are replaced with bulkier cations, the Goldschmidt tolerance factor reaches values $t > 1$, and the 3-dimensional perovskite structure presented in the previous section is not stable anymore. In such conditions, the stable crystal structure is A_2MX_4, where A is the large organic cation, M is the metallic cation, and X is the halogen anion. Due to steric effects, the large cations confine the octahedra in 2-dimensions, forming what is called a *2-dimensional perovskite*. In this structure, layers of corner-sharing octahedra are separated by the organic cations, as shown in **Figure 1.2a** for the 2D perovskite BA_2PbI_4 (BA=butylammonium), to be compared with the 3D perovskite $MAPbI_3$ in **Figure 1.2b**.

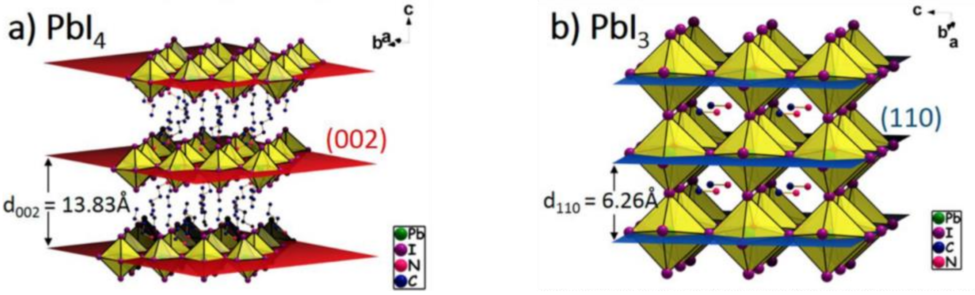

Figure 1.2 Crystal structure of **(a)** the 2D perovskite BA_2PbI_4 (BA=butylammonium), and **(b)** the 3D perovskite $MAPbI_3$. Adapted from ref.[23].

Between the 2D and the 3D crystal structure, there exist what are called quasi-2D perovskites. An example is $(BA)_2(MA)_{n-1}Pb_nI_{3n+1}$, which for $n = 1$ corresponds to the 2D perovskite BA_2PbI_4, and for $n = \infty$ to the 3D perovskite $MAPbI_3$. For intermediate values of n, the system crystallizes forming n layers of corner sharing octahedra separated by one layer of organic spacers.[23]

1.1.3 Structural phase transitions

A perovskite crystal, i.e., an infinite repetition in all three dimensions of the unit cell in **Figure 1.1**, is characterized by corner-sharing octahedra, kept together by M-X-M bonds. Such bonds are highly mobile, for this reason all perovskite materials undergo structural phase transitions under external stimuli, like temperature and pressure.[21] Phase transitions are characterized by a decrease of the M-X-M angle from 180°, i.e. the ideal cubic structure, to lower angles that cause a octahedra tilting. According to the nomenclature introduced by Stoumpos et al.,[24] the cubic phase is referred to as α phase, and occurs at high temperature. Lowering the temperature leads to a tetragonal phase, named β phase. Finally, the lowest temperature phase is the orthorhombic γ phase. As an example, **Figure 1.3a** shows four unit cells of a $CsPbI_3$ crystal in the cubic α phase. **Figure 1.3b-c** show the β and γ phases, which occur lowering the temperature below 260°C, and 175°C, respectively.[21] From the figure, it is clear how the M-X-M angle decreases moving from the α to the γ phase.

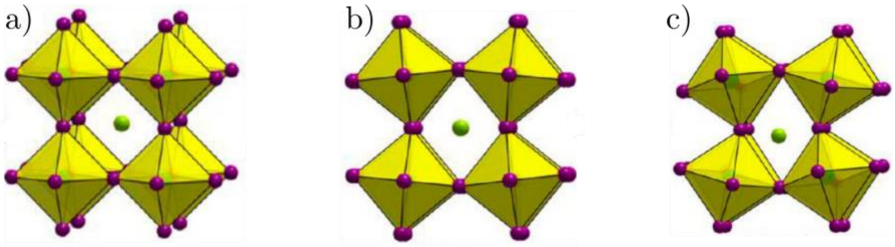

α-$CsPbI_3$ β-$CsPbI_3$ (260°C) γ-$CsPbI_3$ (175°C)

Figure 1.3 Phase transition in $CsPbI_3$. **a)** high-temperature α phase (cubic), **b)** middle-temperature β phase (tetragonal), **c)** low-temperature α phase (orthorhombic). Adapted from ref.[21].

Every MHP has different phase transition temperatures, due to the different chemical elements that compose them. For example, $MAPbBr_3$ crystallizes in the cubic α phase at room temperature, turns in the β phase at 235 K, and then undergoes two phase transitions to two orthorhombic phases, γ_1 and γ_2, at 149.3 K and 154.9 K, respectively.[25]

To date, no phase transition has been reported in literature for 2D MHPs. On the other hand, phase transitions were observed in quasi-2D MHPs, for example in $(PBA)_3Pb_2I_7$ (PBA = phenylethane boronic acid).[26]

1.2 Opto-electronic properties

1.2.1 Band structure

Figure 1.4a shows the band structure of $MAPbI_3$, calculated by Brivio et al. with the many body perturbation theory in the GW approximation, including spin-orbit coupling.[27] The direct character of the energy gap of $MAPbI_3$ is evident in this representation, as the valence band minimum (VBM) and conduction band maximum (CBM) occur at the same point of the

Brillouin zone. This property is shared among all MHPs, and it is one of the key features that enabled the high performance achieved in optoelectronic devices based on these materials. Indeed, a direct bandgap allows band-to-band electronic transitions to occur without assistance of phonons, which highly enhances efficiency of light absorption and emission processes.

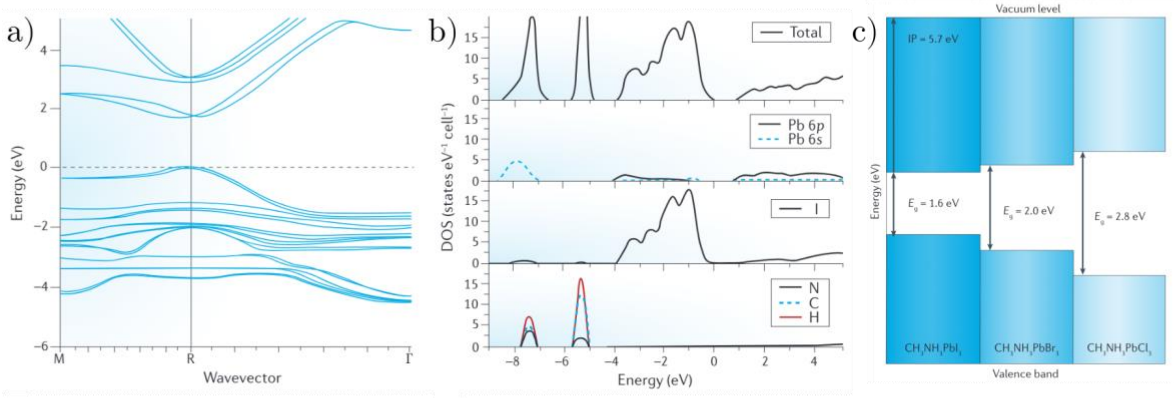

Figure 1.4 a) Band structure of $MAPbI_3$ calculated by many-body perturbation theory, which demonstrate the direct character of the bandgap. **b)** DFT-calculated projected density of states (DOS) of $MAPbI_3$ in the tetragonal phase. In addition to the total DOS, also the contributions from the single elements are shown. **c)** Fundamental bandgaps of $MAPbX_3$ (X=I, Br, Cl) calculated in the GW approximation. Adapted from ref.[27].

Figure 1.4b shows the total density of states (DOS) of $MAPbI_3$, as well as the contribution of the single chemical elements to each band. It is evident that the valence band arises mostly from the contribution of the *p*-states of the halogen (I), while the conduction band is mostly composed by Pb *p*-states. This is what is expected from ionic materials like MHPs: the main contribution to the valence band comes from the anion, and the main contribution to the conduction band comes from the cation.

The contribution from the organic cation only affects the electronic states several eV below the valence band. This indicates a weak interaction between the organic cation and the inorganic ions. However, this does not mean that the organic cation has little impact on the structural, and opto-electronic properties. As discussed in the previous section, the choice of the organic cation is essential to determine the crystal structure and phase transitions of the MHP. Moreover, changing the organic molecule allows to fine-tune the bandgap and to optimize the absorption of optoelectronic devices. For example, partly replacing MA with FA in solar cells allowed to exceed 20% efficiency.[28]

Figure 1.4c shows the calculated fundamental bandgaps of $MAPbX_3$, with X=I, Br, Cl. It is evident how, moving from the heaviest halide atom (I) to the lightest one (Cl), the bandgap increases from 1.6 to 2.8 eV. This property has been highly exploited to synthesize mixed compositions where the halide in a MHP is partly replaced by other halides to fine-tune the bandgap and other optoelectronic properties.

1.2.2 Optical absorption

When light with intensity I_0 impinges on a semiconductor slab, it gets absorbed, and the intensity exponentially decreases as a function of the depth z in the material, following the well-known Beer-Lambert law[29]

$$I(z) = I_0 e^{-\alpha(\lambda)\cdot z} \qquad 1.2$$

where $\alpha(\lambda)$ is the wavelength-dependent absorption coefficient. In all semiconductors α shows a step-like behaviour as a function of the impinging photon wavelength, with a steep rise at the wavelength corresponding to the bandgap energy. **Figure 1.5a** shows the absorption spectrum of $MAPbI_3$, compared with two of the most technologically-relevant inorganic semiconductors: GaAs and crystalline silicon. $MAPbI_3$ shows an absorption coefficient in the order of 10^5 cm^{-1}, i.e., one to two orders of magnitude higher than silicon, and slightly higher than the one of GaAs.[27] A high absorption coefficient is key for producing highly efficient thin film devices like solar cells and photodetectors, while keeping a low film thickness, favouring charge carrier extraction. As an example, based on Equation 1.2, an absorption coefficient of 10^5 cm^{-1} implies that nearly 100% of the visible light is captured within 300 nm of a $MAPbI_3$ slab. This has two important implications: (i) it is possible to absorb all impinging photons, even employing small quantities of raw material, reducing cost; (ii) if the diffusion length of charge carriers exceeds 300 nm, virtually all photogenerated carriers can be extracted at the contacts of the film, leading to high efficiencies. Another relevant feature that can be observed in these spectra is the high slope of the absorption onset, which is expected in a direct bandgap semiconductor like $MAPbI_3$. From such slope it is possible to extract the so-called Urbach Energy (E_U). Typically, low values of E_U are related to a high crystalline quality of the material (low defects density), which usually correlates with excellent transport properties, like large carrier mobility.[30] The Urbach Energy of $MAPbI_3$ was measured to be as low as 15 meV, comparable to that of 11 meV in Si and 8 meV in GaAs.

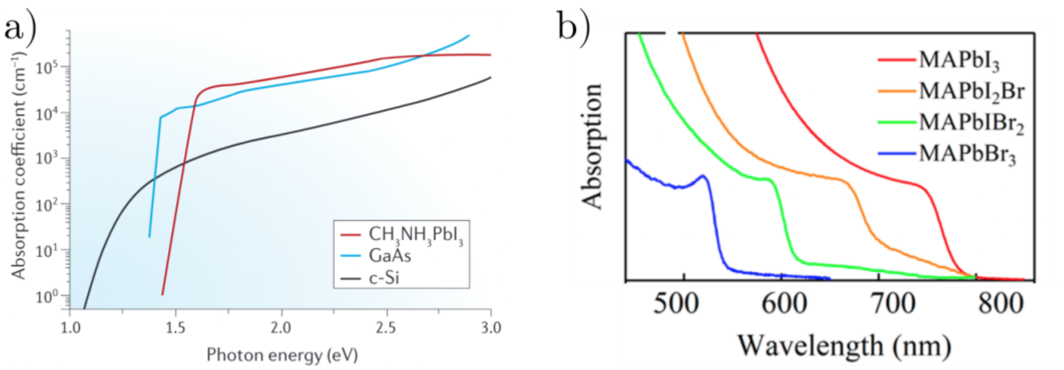

Figure 1.5 a) Absorption coefficient as a function of photon energy of $MAPbI_3$, GaAs, and crystalline silicon. Adapted from ref.[27] **b)** Absorption spectra of $MAPbI_3$, $MAPbBr_3$, and two mixed anion compositions $MAPbI_2Br$, $MAPbIBr_2$. Adapted from ref.[31].

As discussed in the previous Section, changing the halide atom in the MHP structure directly impacts the bandgap energy. This is reflected in the absorption spectra, as exemplified in **Figure 1.5b**, which shows the absorption spectrum of $MAPbI_3$, $MAPbBr_3$, and the mixed compositions $MAPbI_2Br$ and $MAPbIBr_2$. As iodine is progressively substituted with bromine, the bandgap increases, and, as a consequence, the absorption edge shifts to higher energies (lower wavelengths). It is also possible to observe a peak progressively appearing just above the absorption edge, as Br enters in the crystal structure. This is related to excitons, which have a higher binding energy in $MAPbBr_3$ than in $MAPbI_3$, and thus are observable in room-temperature absorption spectra.[32] Excitons in MHPs will be discussed in more detail in the following.

1.2.3 Photoluminescence

Photoluminescence (PL) is a physical process in which an electron in the valence band of a semiconductor is excited into the conduction band upon absorption of an above-gap photon, and then de-excites back to its ground state, emitting a photon via spontaneous emission. This process is typically observed only in direct bandgap semiconductors, since, to occur in indirect semiconductors, it requires the emission of a phonon, and thus is less probable.

Being direct bandgap semiconductors, all MHPs show good photoluminescence properties, with reported PL quantum yields up to 90%.[33] This makes MHPs promising active materials for fabrication of efficient LEDs and lasers.[34] The bandgap tunability discussed in the previous Section is a key feature also for light emitting devices, since it allows to tune the colour of the emitted light. As an example, **Figure 1.6a** shows the PL spectra of caesium lead halide perovskite nanocrystals in solution. Different stoichiometric ratios of the halide atoms (I, Br, Cl) allow to tune the bandgap of the nanocrystals, enabling PL emission in the whole visible range.

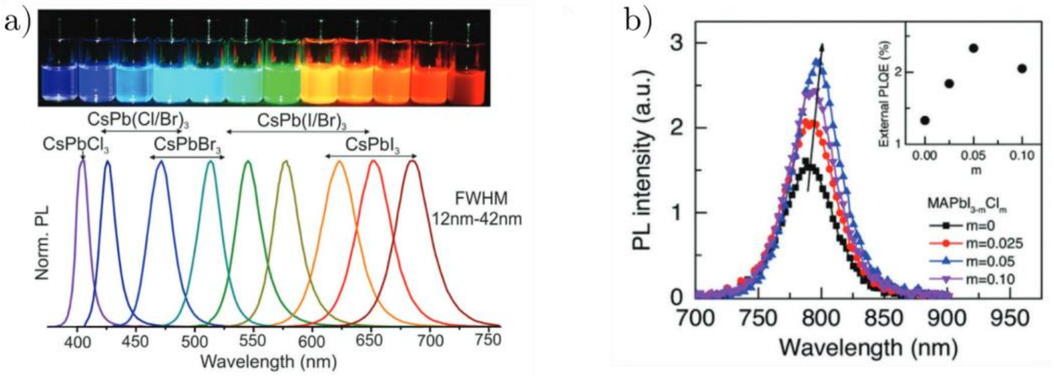

Figure 1.6 a) Photoluminescence spectra of caesium lead halide perovskite nanocrystals, in solution. Changing the stoichiometric ratios of the halide element allows to tune the PL emission in the whole visible range. Adapted from.[35]. **b)** PL spectra of $MAPbI_{3-m}Cl_m$ with different values of m. The inset shows the external PL quantum efficiency as a function of m. Adapted from ref.[36].

PL measurements are also used as an indication of material's quality. Typically, a brighter PL (i.e., a higher PL quantum efficiency) is indicative of better material's quality. This is because defects in semiconductors often act as non-radiative recombination centres, therefore, brighter PL is indicative of a less defective sample.[37] As an example, **Figure 1.6a** shows the PL spectra of $MAPbI_{3-m}Cl_m$ with different values of m, measured by Nan et al.[36] They found that addition of Cl with $m = 0.05$ maximizes the PL quantum efficiency, probably due to defect passivation by the chlorine atoms.

1.2.4 Surface Photovoltage

Any surface of a crystalline material, being an interruption of the periodicity of the lattice, often contains defects. Surfaces can present dangling bonds, steps and kinks, and can also contain adsorbed impurity atoms. These cause the formation surface-localized states within the bandgap of the semiconductor. The existence of such surface defect states induces charge transfer between the surface and the bulk, resulting in a change of the free carrier density at the surface. This causes the formation of a surface space charge region (SCR), i.e., a region with non-zero electric field. Therefore, even in dark conditions, the potential of the surface V_S differs from that in the bulk. This is represented in **Figure 1.7a** for a semiconductor with upward band bending at the surface, which implies the presence of electrons trapped at the surface states.

When above-gap light impinges on the surface, it creates electron-hole pairs, which are separated by the electric field in the SCR. In the example of **Figure 1.7b**, electrons are pushed towards the bulk, and holes towards the surface. Accumulated holes at the surface reduce the density of surface-trapped electrons, thus reducing the band bending (dashed line in **Figure 1.7b**). The surface photovoltage (SPV) is defined as the difference between the surface potential under illumination and in the dark (represented as a double arrow in figure).

$$SPV = V_S(light) - V_S(dark) \qquad 1.3$$

If electronic defect states exist at the surface, an SPV can be generated also by photons with energy equal to the energy jump between the valence band and the defect level, as represented in **Figure 1.7b**. An SPV can be generated also by other physical phenomena, e.g., an excitation of a trapped electron from a defect level to the conduction band. For a full treatment of the SPV theory, we refer the reader to the manuscripts of Kronik and Shapira.[38,39]

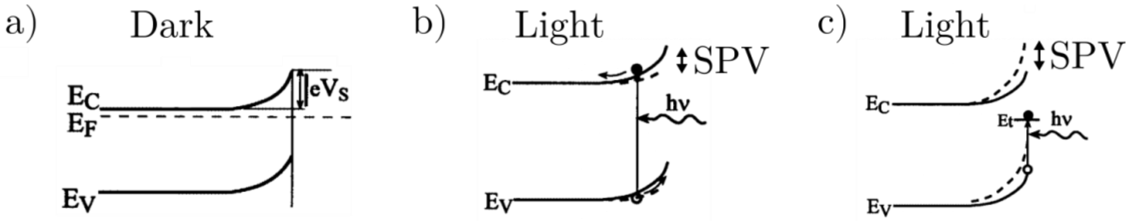

Figure 1.7 Band diagrams of the surface of a semiconductor. The vertical direction represents energy, the horizontal one space. On the left is represented the bulk, and on the right the surface. **a)** Band diagram in the dark, with the surface SCR inducing a surface potential V_S. **b)** Band diagram under illumination with photon of energy equal to the bandgap creating a electron-hole pair, then separated by the built-in electric field. **c)** Band diagram under illumination with photon of energy equal to the energy difference between the valence band and a surface defect state. In (b) and (c) solid and dashed lines represent the bands in the dark and under light, respectively. Adapted from ref.[38].

The experimental technique that consists of monitoring the SPV as a function of the impinging photon energy is called Surface Photovoltage Spectroscopy (SPS). SPS is a powerful surface-sensitive technique that can serve two purposes: characterizing surface defects, and investigate the absorption properties of semiconductors, to extract the energy gap, the Urbach energy, and other absorption parameters. Indeed, it is found that in the vicinity of the bandgap energy, if reflectivity variation near the absorption edge is less pronounced than transmittivity (which is often the case), the SPV is related to the absorption coefficient by the simple relation[40]

$$SPV \propto \frac{\alpha}{h\nu} \qquad 1.4$$

Where $h\nu$ is the photon energy. Thus, this technique is a remarkable tool to gather the whole absorbance spectrum of semiconducting crystals in a single measurement. This is typically not possible for single crystals with thickness above hundreds of microns, unless they are purposely thinned. Indeed, single crystal absorption measurements are typically performed with two separate measurements: transmittance below the bandgap and reflectance above the bandgap, as no transmitted light can be measured above the bandgap energy for thick samples.[41,42]

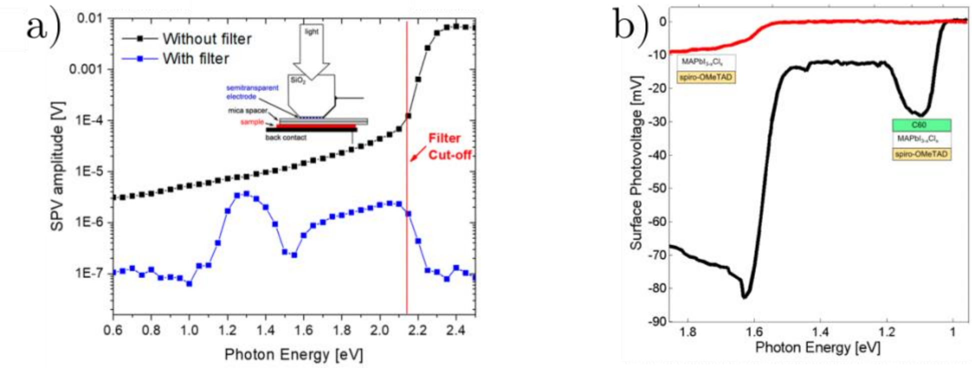

Figure 1.8 a) SPS on $MAPbBr_3$ thin films with and without a long-pass filter. The measurement with the filter reveals the existence of deep surface states. Adapted from ref.[43]. **b)** SPS on $MAPbI_{3-x}Cl_x$ on spiro-OMeTAD, with and without C60 top contact, revealing the appearance of a new spectral feature in the infrared region. Adapted from ref.[44].

SPS measurements were performed on MHPs by several research groups, mainly to investigate surface defect states in thin films. For example, Levine et al.[43] performed SPS on $MAPbBr_3$ thin films, and found the existence of deep surface states, employing a low pass filter to cut off the signal from above-gap transitions (**Figure 1.8a**). Barnea-Nehoshtan et al. used SPS to characterize the effect of different contact layers on the spectral features of $MAPbI_{3-x}Cl_x$, for solar cell applications (**Figure 1.8b**).[44] They found that C60 and other interlayer materials generate a spectral feature in the infrared region, which they assigned to a reduced effective bandgap at the grain boundaries.

1.2.5 Excitons in metal halide perovskites

An electron-hole pair in a semiconductor can form a hydrogen-like state due to mutual Coulombic interaction. This creates a quasi-particle referred to as *exciton*, characterized by hydrogen-like quantized states, with binding energies given by[29]

$$E_b = \frac{1}{n^2} \cdot \frac{\mu}{m_0 \varepsilon_r^2} \cdot R_0 \tag{1.5}$$

where n is a quantum number taking only integer values, denoting the different orbitals, m_0 is the electron mass, ε_r is the relative permittivity on the material, R_0 is the Rydberg unit of energy (≈ 13.6 eV), and μ is the reduced electron-hole effective mass $\mu^{-1} = m_e^{*\,-1} + m_h^{*\,-1}$. Depending on the material's properties, the ground state E_b can vary from values as low as 4.2 meV for GaAs, up to large values as 59 meV for ZnO.[29]

One of the clearest signs of the presence of excitons is the appearance in the absorption spectrum of a peak close to the absorption edge of the semiconductor. Such peak corresponds to the formation of excitons by light-induced electron hole pairs. Excitonic features can be observed at room temperature only if the exciton binding energy is larger than the thermal energy $k_B T$ at room temperature, with k_B the Boltzmann constant. Otherwise, thermal energy is enough to break the electron-hole bond, causing exciton dissociation.

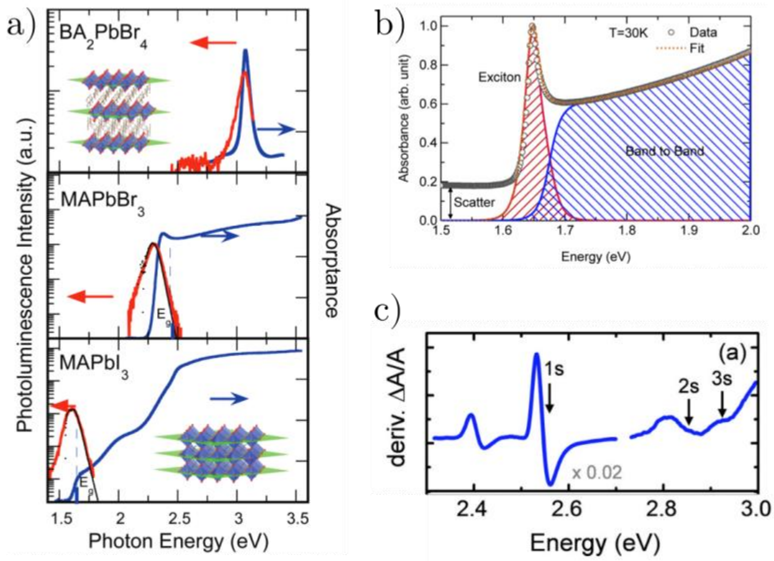

Figure 1.9 a) PL and absorption spectra of BA_2PbBr_4, $MAPbBr_3$, and $MAPbI_3$. From ref.[45]. **b)** Absorption spectrum of $MAPbI_3$ measured at 30 K, fitted by the band-to-band and exciton components. Adapted from ref.[46]. **c)** Derivative of the absorption spectrum of BA_2PbBr_4 measured at 5 K temperature, showing the 2s and 3s energy levels of the exciton, in addition to the ground state 1s state. Adapted from ref.[47].

Focussing on MHPs, at room temperature $MAPbI_3$ shows a step-like edge in the absorption spectrum, corresponding to band-to-band absorption, as shown in the bottom panel of **Figure 1.9a**. By substituting iodine with bromine, the dielectric constant increases, leading to an increased exciton binding energy. The mid panel of **Figure 1.9a** shows the room temperature absorption spectrum of $MAPbBr_3$, where the excitonic resonance is visible in correspondence of the absorption edge. Moving to 2D perovskites, the exciton binding energy increases even more, as shown by the top panel of **Figure 1.9a** for BA_2PbBr_4. This is due to the spatial and dielectric confinement that electron-hole pairs experience in 2D systems, leading to a further increase in the exciton binding energy. The absence of the excitonic resonance in $MAPbI_3$ is due to its low exciton binding energy, usually reported between 5 and 29 meV, i.e., lower or similar to $k_B T \approx 26$ meV at room temperature. Excitons also play a major role in determining the photoluminescence properties of MHPs. PL spectra of perovskites are invariably peaked closer to the excitonic resonance, rather than the band-to-band transition, as can be observed in **Figure 1.9a**. This is an indication that the most relevant contribution to the PL in MHPs comes exciton recombination, rather than free carrier recombination.[45]

Figure 1.9b, shows a low temperature (30 K) absorption spectrum of $MAPbI_3$, where the excitonic resonance is clearly visible, as thermal energy is not enough to dissociate the exciton at this temperature. In addition to the raw data, the authors overlaid the two band-to-band and excitonic components that well fit the absorption spectrum. Measurements at even lower temperatures allow to observe the excited states of the excitons from the absorption spectra. **Figure 1.9c** shows the derivative of the absorption spectrum of BA_2PbBr_4 measured at 5 K temperature, showing the 2s and 3s energy levels of the exciton, in addition to the 1s ground state.

Despite the clear evidence of the presence of excitons in MHPs, the measurement of their binding energy has proven to be a difficult task. Different techniques yield different values for the exciton binding energy. For example, for $MAPbI_3$, fitting of the absorption spectra leads to values between 5 and 29 meV, but ultrafast THz spectroscopy yields 50 meV. The cause of such mismatch is still not fully understood, and this topic is still under discussion among researchers.[32]

1.2.6 Free carrier transport properties

One of the main reasons why hybrid lead halide perovskites are receiving such high attention by the research community are their excellent electronic transport properties. **Figure 1.10** reports some of the most impressive figures of merit for electronic transport measured on MHP thin films or single crystals. **Figure 1.10a** shows the transient PL measurements of $MAPbI_{3-x}Cl_x$ thin films, by which Petrozza et al.[48] extracted an electron-hole diffusion length of more than 1µm. Considering perovskite solar cells have a typical thickness of a few hundreds of nanometres, this figure indicates that virtually all photoexcited carriers in the absorber can reach the collecting contacts before recombining. **Figure 1.10b** shows transient absorption measurements on $MAPbBr_3$ single crystals, revealing up to 1μs carrier lifetime, comparable to that of GaAs.[27]

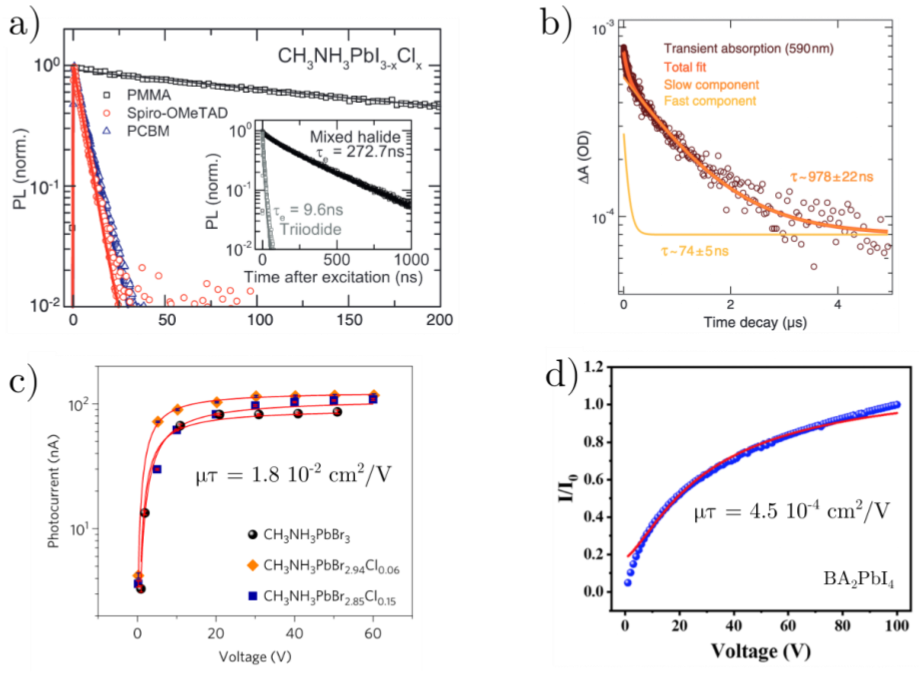

Figure 1.10 a) Transient photoluminescence measurements of a $MAPbI_{3-x}Cl_x$ thin film coated with PMMA, and with electron (PCBM) or hole (Spiro-OMeTAD) quencher layers. Adapted from ref.[48]. **b)** Transient absorption measurement of a $MAPbBr_3$ single crystal. Adapted from ref.[49]. **c)** Photocurrent versus voltage of a $MAPbBr_3$ single crystal with and without small amounts of chlorine in the structure. The extracted $\mu\tau$ value by the Hecht fit of the data. Adapted from ref.[50]. **d)** Photocurrent versus voltage of a BA_2PbBr_4 single crystal. The extracted $\mu\tau$ value by the Hecht fit of the data. Adapted from ref.[51].

Figure 1.10c shows the photocurrent versus voltage of $MAPbBr_3$ of a pure single crystal, and two single crystals with few percent Cl doping. By fitting these data to the Hecht equation, Wei et al. obtained a mobility-lifetime product $\mu\tau = 1.8\ 10^{-2}\ \mathrm{cm}^2/\mathrm{V}$.[50] This value exceeds by one order of magnitude the $\mu\tau$ of CdTe.[52]

2D perovskites, due to their peculiar multi-quantum well structure, suffer from poorer electrical performance. Indeed, the electrical transport is confined to the 2-dimensional perovskite sheets, while charge carriers cannot move into the insulating organic spacers. **Figure 1.10c** shows the photocurrent versus voltage curve of a 2D MHP BA_2PbI_4 single crystal, from which the authors extracted a $\mu\tau$ product of $4.5\ 10^{-4}\ \mathrm{cm}^2/\mathrm{V}$,[51] i.e. two orders of magnitude lower than what can be achieved with 3D MHPs like $MAPbBr_3$.

1.2.7 Ion migration

Experimental and computational evidence

One of the first indications of the presence of slow-moving charge carriers in MHPs was the observation of hysteresis in current-voltage (I-V) characteristics of MHP solar cells. **Figure 1.11a** shows a dark I-V curve of a $MAPbI_3$ solar cell measured at different scan rates, with arrows indicate the forward and backward scan direction. The amount of hysteresis decreases for lower scan rates, a typical behaviour of capacitive currents. This effect is commonly associated to ion migration in the perovskite layer, and accumulation at the contacts, creating a slow capacitive response. It was shown that specific contact materials can almost completely hinder hysteresis, implying that such effect is not only relative to the perovskite layer itself, but to the interaction of moving ions with the contact materials.[53]

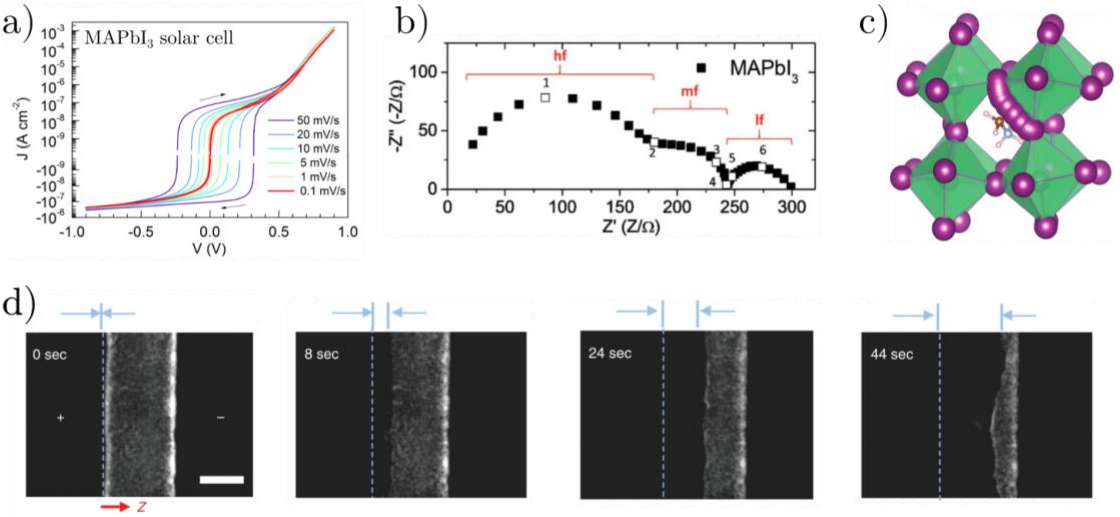

Figure 1.11 a) Dark I-V curve of a $MAPbI_3$ solar cell measured at different scan rates, showing scan-rate-dependent hysteresis. Adapted from ref.[53]. **b)** Nyquist plot of an impedance spectrum of a $MAPbI_3$ solar cell, showing high, medium, and low frequency (hf, mf, lf) features. Adapted from ref.[54]. **c)** First principles calculation of the migration pathway of an iodide vacancy in a $MAPbI_3$ unit cell. Adapted from ref.[55]. **d)** Time-dependent PL microscope images of a $MAPbI_{3-x}Cl_x$ thin film under an applied electric field. A dark wavefront is observed moving from the positive to the negative contact in a timescale of seconds. The scale bar represents 100 µm. Adapted from ref.[56].

Frequency-resolved measurements are often used to characterize ion migration in MHPs. **Figure 1.11b** shows an impedance spectroscopy measurement of a $MAPbI_3$ solar cell in the Nyquist representation (i.e., imaginary part of the impedance as a function of the real part). In this plot, frequency decreases moving from left to right, and each semi-circle can be considered as a physical process occurring in the device. The high frequency (HF) feature is usually attributed to the geometric capacitance and the electronic recombination resistance. About the attribution of the mid and low-frequency responses researchers are still debating, although their ionic nature is commonly accepted. Some attribute them to an ionic current in the MHP layer,[57] others to electronic currents that are modulated by the moving ions, which slow down injection and recombination processes.[54,58]

Ion migration has been investigated also by computational studies. **Figure 1.11c** shows the first principles calculation of the migration pathway of an iodide vacancy in a unit cell of $MAPbI_3$. In general, computational studies agree on the fact that the most mobile ionic species are related to halide atoms, and in particular to halide vacancies. Organic cation vacancies and interstitials are estimated to be less mobile than halides, while Pb is usually reported to be immobile, due to its large weight.[55,59]

In addition to DC and AC electrical measurements, ion migration has been investigated by various other techniques. An example is reported in **Figure 1.11d**, which shows a series of PL images of a $MAPbI_{3-x}Cl_x$ thin film with two coplanar contacts, acquired with a microscope while the film is under an applied bias.[56] Initially, PL emission occurs in the whole film. In a timescale of seconds, a dark wavefront appears at the positive contact side and moves towards the negative contact. This result was explained in terms of migration of positively charged iodine vacancies (V_I^+) towards the negative contact. During their motion, V_I^+ compensate the negative charge of iodine interstitials, reducing the hole density. Such reduction of doping and the creation of non-radiative recombination centres via redox reactions of V_I^+ with other elements causes the formation of the dark region, which moves at the same speed as the ionic specie. Therefore, this can be considered as a direct visualization of ionic motion in a MHP thin film. By these images, the authors were able to estimate V_I^+ to have a mobility of $9.1 \cdot 10^{-7}\ \mathrm{cm^2V^{-1}s^{-1}}$.

Determination of ionic diffusion parameters

Ion migration is a temperature-dependent process, where the higher the thermal energy, the faster and easier the ionic motion. The ionic diffusion coefficient exponentially increases with temperature, according to[52,60,61]

$$D = D_0 \exp\left(-\frac{E_a}{k_B T}\right) \tag{1.6}$$

Where D_0 is the diffusion coefficient at infinite temperature, and E_a is the activation energy for ionic motion. These are the two key parameters that characterize a moving ion inside a material.

The ionic conductivity can be expressed as $\sigma = nZe\mu$, where n is the volumetric charge density of ions, Z is their charge, e is the electronic charge, and μ is their mobility. The Nernst-Einstein relation links the mobility to the conductivity via $\mu = eD/k_BT$, so that the ionic conductivity can be expressed by[60]

$$\sigma = \frac{\sigma_0}{k_BT}\exp\left(-\frac{E_a}{k_BT}\right) \qquad 1.7$$

With $\sigma_0 = e^2T^mD_0$, where m is typically between 0 and 1.

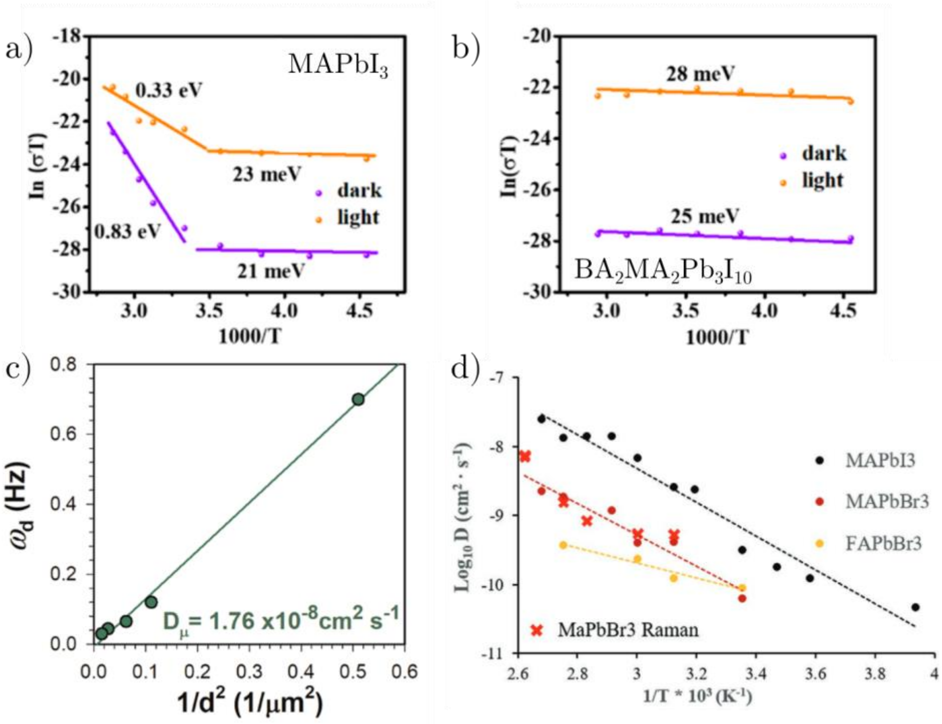

Figure 1.12 Conductivity versus temperature plot of **(a)** $MAPbI_3$ and **(b)** quasi-2D $BA_2MA_2Pb_3I_{10}$ single crystals in dark and light conditions. The activation energies are extracted by the Nernst-Einstein fit are reported for all the identified regimes. Adapted from ref.[62]. **c)** Characteristic frequency extracted by impedance spectroscopy as a function of $1/d^2$, with d the thickness of a $MAPbBr_3$ single crystal, yielding the diffusion coefficient of migrating ions. Reproduced from ref.[57]. **d)** Logarithm of the diffusion coefficient as a function of the reciprocal of temperature, extracted by NMR (dots) and Raman (red crosses) measurements for $MAPbI_3$, $MAPbBr_3$, and $FAPbBr_3$. Adapted from ref.[63].

Based on Equation 1.7, by fitting experimental data of $\ln(\sigma T)$ as a function of T^{-1} yields the activation energy for ion migration. This procedure is usually referred to as Nernst-Einstein fit, and it was widely adopted to estimate the activation energy for ionic motion in MHPs.[62,64–66] An example is shown in **Figure 1.12a-b** for single crystals of $MAPbI_3$, and quasi-2D $BA_2MA_2Pb_3I_{10}$ under dark and light conditions. Both samples show a low temperature region with small activation energy, between 20 and 30 meV. This is typically attributed to the activation energy of electronic carriers. $MAPbI_3$ also shows a second regime at high temperature, with a much higher slope, yielding an activation energy of 0.83 eV. This high temperature regime is attributed to ionic motion, according to Equation 1.7, and is observed in virtually any 3-dimensional MHP.[65,67] On the contrary, the quasi-2D perovskite does not show any evidence for an activation of ion migration, at least in the reported temperature range. This is commonly considered as evidence for the suppression of ion migration in 2D and quasi-2D perovskites, which explains their enhanced long term electrical stability with respect to 3D perovskites. Interestingly, under light, the activation energy for ion migration of $MAPbI_3$ is greatly reduced to 0.33 eV, implying that above-gap light excitation favours ion migration. This result was confirmed by many other research groups through a variety of experimental techniques.[68–71] An understanding of such light-induced ion migration is of fundamental importance for device applications, as it implies that solar cells and detectors are more prone to ion migration during their operation.

Ion migration can also be characterized by a variety of other techniques. **Figure 1.12c** shows the characteristic frequency of ionic motion extracted by impedance spectroscopy measurements as a function of $1/d^2$, with d the thickness of a $MAPbBr_3$ single crystal device. The linear fit of these data allowed the authors to extract a diffusion coefficient for migrating ions in $MAPbBr_3$ of $1.76 \cdot 10^{-8}\ \mathrm{cm}^2/\mathrm{s}$. **Figure 1.12d** shows the linear fit of the logarithm of the diffusion coefficient as a function of $1/T$ for $MAPbI_3$, $MAPbBr_3$, and $FAPbBr_3$ single crystals.[63] The diffusion coefficient was extracted via NMR measurements (dots) or Raman spectroscopy (red crosses). The authors claim that these diffusion data are related to migration of H^+ protons. Indeed, they propose that, in addition to the classical halogen and cation vacancies and interstitials, the MHP cation can release protons, which are able to migrate in the crystal with room temperature diffusivities in the range $10^{-9} - 10^{-10}\ \mathrm{cm}^2/\mathrm{s}$.[63]

1.3 Reactivity and degradation

One of the main aspects that is currently limiting the commercialization of MHP-based devices is their high reactivity to environmental gases such as oxygen and water, as well as to light and electrical potential. In this Section, I present a brief overview of literature results about the reactivity and degradation pathways of MHPs under environmental gases, illumination, and electrical potential.

1.3.1 Environmental reactivity

Water is one of the most damaging agents for the MHP structure, causing its irreversible degradation. It causes a decomposition of the MHP structure ABX_3 into its constituent components, according to the chemical reaction[11]

$$\mathrm{ABX_3} \xrightarrow{\mathrm{H_2O}} \mathrm{AX} + \mathrm{BX_2} \qquad 1.8$$

Which can be followed by further degradation reactions involving the AX an BX_2 products.[11] **Figure 1.13a** shows SEM images of a $MAPbI_3$ thin film before and after exposure to deionized water. The smooth surface of the film changes completely after water exposure, breaking into needle-like microcrystals. An XPS analysis of such samples by the authors showed that MA is completely washed away upon water exposure, leaving PbI_2 residuals, that form such needle-like structures.[72] This reaction occurs also upon exposure to moisture in the air, although with a much lower degradation rate.

Water molecules were also shown to be easily adsorbed on the surface of MHPs. An example is reported in **Figure 1.13b**, which shows the Fourier Transform Infrared (FTIR) spectrum of a $MAPbI_3$ in air and in vacuum. When the sample is exposed to standard air atmosphere, a feature at around 3500 cm^{-1} appears, which is a well-known spectral feature of the O-H stretch vibration.[73] The authors found, as opposed to the previously described degradation reaction, that this is a reversible process. Indeed, pumping vacuum after air exposure, or exposure to dry gases like N_2 or O_2, makes the feature disappear.

Even vacuum was found to trigger degradation reactions in MHPs. **Figure 1.13c** shows the time evolution of the X-ray diffraction (XRD) spectra of $MAPbI_3$ in dark and under 10^{-6} mbar high vacuum. After 24 hours the intensity of the $MAPbI_3$ peaks reduces, and after 12 hours a PbI_2 peak is already visible. The degradation reaction proposed by the authors is:[74]

$$\mathrm{CH_3NH_3PbI_3} \xrightarrow{\mathrm{vacuum}} \mathrm{CH_3NH_2} \uparrow + \mathrm{HI} \uparrow + \mathrm{PbI_2} + V_{\mathrm{I}}^{-} \qquad 1.9$$

where the upward arrows indicate volatile species that leave the perovskite structure.

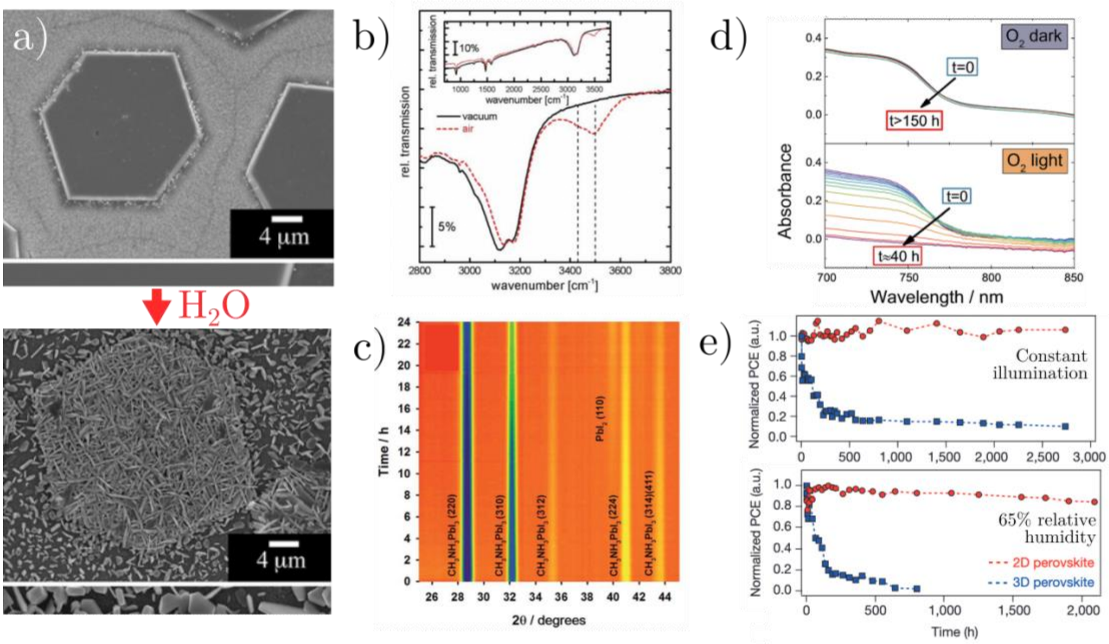

Figure 1.13 a) SEM images of $MAPbI_3$ thin films before (top) and after (bottom) contact with deionized water. Adapted from ref.[72]. **b)** FTIR spectrum of a $MAPbI_3$ thin film under vacuum (solid black line) and in air (dashed red line). Adapted from ref.[73]. **c)** Time-dependent XRD spectra of $MAPbI_3$ thin films under vacuum at 350 K. Each peak of the XRD spectra is labelled with the corresponding chemical species. Adapted from ref.[74]. **d)** Time evolution of the absorption spectra of $MAPbI_3$ thin films under oxygen atmosphere in dark (top) and 4.6 mW/cm^2 light (bottom) conditions. Adapted from ref.[12]. **e)** Time evolution of the power conversion efficiency of $MAPbI_3$ (blue dots) and quasi-2D $BA_2MA_3Pb_4I_{13}$ (red dots) solar cells under constant illumination (top) and 65% relative humidity (bottom). Adapted from ref.[75].

Oxygen is also found to strongly react with MHPs, but typically only when also light is present. **Figure 1.13d** shows the time evolution of the absorption spectra of $MAPbI_3$ thin films under oxygen in the dark (top), and under oxygen and light (bottom). In the former case, the spectra are stable, even after 150 h exposure to oxygen. However, after just 40 hours of exposure to oxygen and light, the absorption spectrum turns into the characteristic spectrum of PbI_2. The degradation reaction proposed for this process is:[12]

$$CH_3NH_3PbI_3 + \frac{1}{4}O_2 \xrightarrow{\text{light}} CH_3NH_2\uparrow + I_2\uparrow + PbI_2 + \frac{1}{2}H_2O \qquad 1.10$$

leading to the formation of lead iodide and also water *in situ*. It is plausible that the sudden acceleration of the degradation process observed at a certain point in time is related to a second degradation pathway caused by the water generated in situ.[12] In theory, the degradation reaction 1.10 could occur also in dark conditions, but it is not kinetically favoured, and therefore is triggered only with the additional energy carried by light.

2D and quasi-2D MHPs show enhanced stability with respect to their 3D counterparts. **Figure 1.13e** shows the time evolution of the power conversion efficiency (PCE) of $MAPbI_3$ and quasi-2D $BA_2MA_3Pb_4I_{13}$ solar cells under constant illumination and 65% relative humidity. The results show that the performance of the 2D perovskite solar cell is virtually unchanged after almost 3000 hours of constant illumination, while the 3D counterpart loses 80% of its efficiency already after 500 hours. The 2D solar cell also shows enhanced stability in the dark upon 65% relative humidity, with a PCE loss of less than 20% in 2000 hours, to be compared with the 100% loss in less than 1000 hours for the 3D counterpart. We note, however that 2D and quasi-2D MHP solar cells are limited by poorer optoelectronic performance, with record PCE of 22.3%, as of 2023.[76] A computational study by Yang et al.[77] suggests that the enhanced stability of 2D perovskites is due to the asymmetric surface properties of these materials. They calculated surface terminations of 2D perovskites to be more stable thanks to fewer dangling bonds and relaxation of surface hydrogen bonds.

1.3.2 Degradation under light

Light plays a key role in the degradation pathway of MHPs, causing major issues for the stability of optoelectronic devices that operate under illumination, like solar cells and photodetectors. **Figure 1.14a** shows the time-dependent XRD spectra of $MAPbI_3$ thin films under air without (top panel) and with (bottom panel) white illumination. In the dark, the film is stable, even more than under high vacuum conditions (compare with **Figure 1.13c**). However, upon white light exposure, it totally degrades in less than two hours. Initially, the structure turns into PbI_2, according to the degradation reaction 1.10. However, after some time, the PbI_2 signature disappears, until no more XRD peaks are visible after 20 hours. This effect was ascribed to the formation of amorphous lead salts, e.g. PbO, $Pb(OH)_2$, and $PbCO_3$, upon interaction of PbI_2 with oxygen and water.[74]

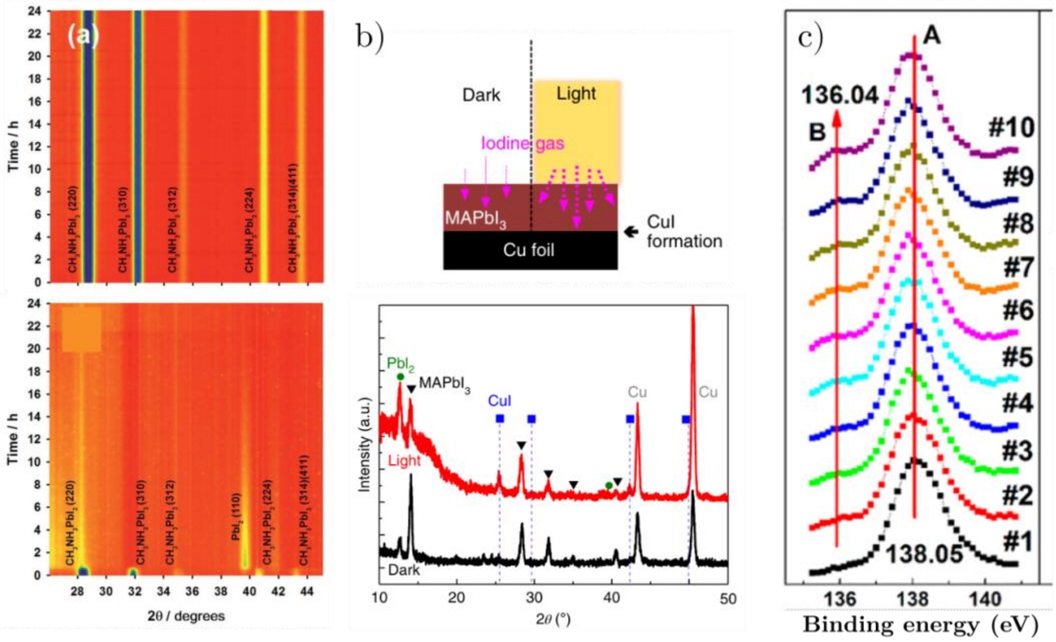

Figure 1.14 a) Time-dependent XRD spectra of $MAPbI_3$ thin films at 350 K, under air without (top) and with white illumination. Each peak of the XRD spectra is labelled with the corresponding chemical species. Adapted from ref.[74]. **b)** Schematic of the setup study of iodine penetration in $MAPbI_3$ thin film (top), and resulting XRD spectra of the Cu foil underlying the $MApbI_3$ film in the dark (black curve), and in air (red curve). Adapted from ref.[78]. **c)** Evolution of Pb4f peaks of a $MAPbBr_3$ single crystal under X-ray irradiation, monitored by 10 successive XPS scans. Adapted from ref.[79].

Another striking effect of light is related to its effect on ion migration. **Figure 1.14b** shows an interesting experiment carried out by Kim et al. to characterize this phenomenon.[78] The top panel shows the experimental setup: a $MAPbI_3$ thin film is deposited on a Cu foil and exposed to I_2 gas. Half of the film is exposed to light, and the other half is left in the dark. If iodine is able to penetrate through the film, it forms CuI in the copper foil, which can be detected by X-ray Diffraction (XRD). The bottom panel shows the resulting XRD of the Cu foil, the dark curve represents the part that remained in the dark, and the red curve the one exposed to light. In addition to the Cu and $MAPbI_3$ peaks, CuI is only visible in the part of the Cu foil exposed to light. I_2 penetrates through $MAPbI_3$ via iodine vacancies, therefore implying a higher concentration of iodine vacancies under light with respect to the dark. The reaction proposed by the authors to explain this phenomenon is the following

$$\mathrm{I} + \mathrm{h}^+ \rightleftharpoons \mathrm{I_i} + \mathrm{V_I^+} \tag{1.11}$$

Here, a neutral iodine atom in the lattice interacts with a photogenerated hole to form a neutral iodine interstitial and a positively charged iodide vacancy. In this picture, the photogenerated hole remains trapped at the iodine interstitial. A release of the hole and a recombination of vacancy and interstitial reverse the reaction.

MHPs are prone to degradation also under high energy photons like X-rays. **Figure 1.14c** shows the evolution of Pb4f peaks of a $MAPbBr_3$ single crystal under X-ray irradiation, monitored by 10 successive X-ray Photoelectron Spectroscopy (XPS) scans. The X-ray source in this case was the same X-ray tube used as photon source for the XPS apparatus. Importantly, the whole measurement is carried out under ultra-high vacuum (UHV). Upon X-ray exposure, a new peak appears at binding energy of 136.04 eV, which is assigned to metallic lead Pb^0. The degradation reaction proposed by the authors is

$$\mathrm{MAPbBr_3} \xrightarrow{\mathrm{X-rays,UHV}} \mathrm{MABr} + \mathrm{Pb^0} + \mathrm{Br_2} \uparrow \quad 1.12$$

This result, however, is not indicative of how the material reacts under real-world working conditions, i.e., in air. Indeed, as discussed above, degradation reactions of MHPs are totally different in air with respect to vacuum conditions. This motivated us to perform a study on the effects of X-ray exposure of $MAPbBr_3$ in ambient conditions, which will be presented in Chapter 3.

In mixed-halide MHPs, it was shown by several research groups that visible illumination induces segregation in the different phases that compose the overall structure. A typical example is $MAPbI_{3x}Br_{3-x}$ that under illumination forms iodine-rich and bromine-rich domains, leading to loss in device performance.[80]

An important aspect of light-induced degradation and ion migration is that experimental results up to now indicate that these effects are only visible when the light source contains photons with energy above-gap. For example, in their study using Time of Flight - Secondary Ion Mass Spectroscopy, Liu et al.[68] showed that light-induced ion migration was clearly visible in $MAPbI_3$ and $MAPbBr_3$ only when using white light, or LED light with above-gap energy, while no effect was observed using below-gap excitation.

1.3.3 Potential induced degradation

Another important degradation pathway for MHP-based devices is related to the application of an external electrical potential. The degradation mechanisms triggered by an electrical potential can be various. In the following we list the most commonly observed. It was shown that an external bias enhances the water-induced degradation described by Equation 1.8, as it causes the drift of vacancies formed in the reaction with water, thus speeding up the process.[81] Electrical potential can also cause the migration of halide interstitials inside the electrical contacts, inducing severe changes in the electrical characteristic of the devices.[82] Ni et al. found that this process occurs due to the interaction of the interstitials with the injected holes, and they were able to improve bias stability by introducing a hole-blocking layer between the MHP and contact layer.[83]

Potential-induced degradation is one of the key challenges to be overcome to produce electrically stable and reliable MHP-based device, and many research groups are currently focussing their attention on this issue.

1.4 Defects

Any real crystal always contains a certain amount of crystalline defects. Typical lattice defects are vacancies (missing atoms), interstitials (atoms occupying interstitial positions in the lattice), and complexes thereof. Defects can also consist of chemical impurities, atoms or molecules that do not belong to the ideal chemical composition of the crystal. From a band structure point of view, being interruptions of the ideal crystal symmetry, such defects introduce electronic states within the forbidden gap of the semiconductor.

Typically, defect states are classified as *shallow* and *deep*. Shallow states are hydrogenic impurities at which the electron weakly binds, forming an extended state. Instead, deep states are more localized, creating a tighter bond with the electrons. Therefore, the former are typically close to the band edges, and the latter are deeper inside the bandgap, hence the naming "shallow" and "deep". The activation energy (E_a) is defined as the energy difference between the defect state and the corresponding band. For conventional semiconductors like Si and GaAs, the threshold activation energy to distinguish between deep and shallow states is typically considered as twice the thermal energy at room temperature, i.e., $E_a \approx 0.05$ eV $\approx 2k_BT$.[84] This means that shallow states are thermally ionized at room temperature, i.e., they act as dopants. On the contrary, deep states are not ionized at room temperature, and for this reason are often referred to as *trap* states.

Deep states are often present in small concentration with respect to shallow ones. Despite this, their presence can be highly detrimental for the transport properties of the material, and for the performance of electronic devices. For example, the minority carrier recombination lifetime can be negatively affected even by small amounts of deep states, with detrimental effects on luminescence efficiency of light emitting devices, and excess currents in photodetectors.[84] Therefore, the study of deep states is of fundamental importance to achieve ultimate device performance, but it also needs highly sensitive techniques, that are able to probe even low concentrations of such impurities. In this Section, I will focus on the description of deep levels, as they were object of a substantial part of the experimental work that I carried out in this thesis work.

1.4.1 Physics of deep levels

Deep levels in thermal equilibrium

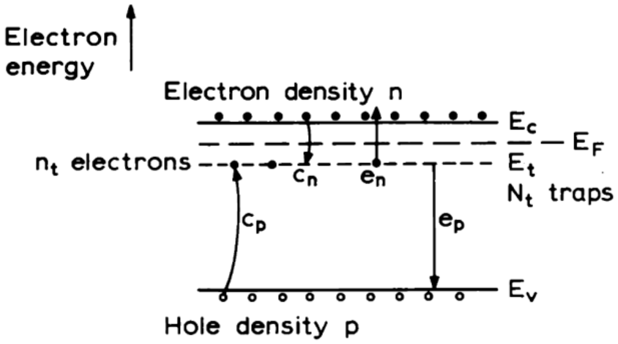

Figure 1.15 Capture and emission processes of electrons and holes from a deep state with energy E_t and of density N_t. Reproduced from ref.[84]

Electrons and holes can interact with a deep state by two possible processes: capture and emission. The former involves the carrier moving from its relative band to the trap state, the latter its emission from the trap state back to the relative band. These processes are characterized by the capture and emission rates for electrons (c_n, e_n) and holes (c_p, e_p), and are schematized in **Figure 1.15**. We will limit our treatment to electrons, but the same reasoning can be applied to holes. If n free electrons with average thermal velocity v_n are present in the conduction band, a trap state is exposed to a flux of nv_n free electrons. The trapping efficiency of the defect states is characterized by a capture cross section σ, which has physical dimensions of an area (typically measured in cm^2), similarly to the concept employed in nuclear physics. The capture rate is then defined as[84]

$$c_n = \sigma_n v_n n \tag{1.13}$$

We define N_t the total trap density, and n_t the density of occupied traps at any instant. The occupancy of the defect state is determined by competing capture and emission processes, which occur dynamically over time. At thermal equilibrium, the two processes must balance, so that[84]

$$e_n n_t = c_n(N_t - n_t) \tag{1.14}$$

We can now consider the Fermi-Dirac distribution function of a deep state at energy E_t, with degeneracy g_0 when empty, and g_1 when occupied by an electron. This allows to write Equation 1.14 as[84]

$$\frac{e_n}{c_n} = \frac{g_0}{g_1} \exp\left(\frac{E_t - E_F}{k_B T}\right) \tag{1.15}$$

Where E_F is the Fermi energy. Typically, $\frac{g_0}{g_1} \approx 1$, therefore, if $E_F > E_t$ the capture rate is larger than the emission rate, otherwise, if $E_F < E_t$, the opposite occurs. This indicates that in the former case, the deep state is occupied by electrons, and, in the latter, it is empty. The motivation for a dependence of emission and capture rates on the Fermi energy is that, according to Equation 1.13, the capture rate is determined by the free electron concentration in the conduction band. This quantity is dependent on the Fermi energy according to the Fermi-Dirac distribution:

$$n = N_c \exp\left(-\frac{E_c - E_F}{k_B T}\right) \tag{1.16}$$

where N_c is the effective density of states in the conduction band, and E_c is the energy of the conduction band edge. By substituting Equations 1.13 and 1.16 in Equation 1.15, we obtain an expression for the temperature-dependent emission rate

$$e_n(T) = \sigma_n v_n \frac{g_0}{g_1} N_c \exp\left(-\frac{E_c - E_F}{k_B T}\right) \tag{1.17}$$

If the effective mass of the charge carriers m^* is known, Equation 1.17 can be further developed, since $v_n = \left(\frac{3k_B T}{m^*}\right)^{1/2}$, and $N_c = 2M_c\left(\frac{2\pi m^* k_B T}{h^2}\right)^{3/2}$, where M_c is the number of conduction band minima, and h is Planck's constant. In general, one should also allow a temperature-dependent capture cross section, typically considered as an exponential in the form[84]

$$\sigma(T) = \sigma_\infty \exp\left(-\frac{\Delta E_\sigma}{k_B T}\right) \tag{1.18}$$

where σ_∞ is the capture cross section at infinite temperature, and ΔE_σ is the thermal activation energy that parametrizes the temperature dependence of σ. Thus, Equation 1.17 can be written as

$$e_n(T) = \gamma T^2 \sigma_{na} \exp\left(-\frac{E_{na}}{k_B T}\right) \tag{1.19}$$

where $\gamma = 2\sqrt{3} M_c (2\pi)^{2/3} k_B^2 m^* h^{-3}$ is a constant containing only fundamental constants and material's parameters. σ_{na} is the *apparent* cross section

$$\sigma_{na} = \frac{g_0}{g_1} \sigma_\infty \tag{1.20}$$

and E_{na} is the *apparent* activation energy of the defect state

$$E_{na} = (E_c - E_t) + \Delta E_\sigma \tag{1.21}$$

Equation 1.19 is the key equation for the experimental characterization of deep defect states. Indeed, the experimental data of the emission rate as a function of temperature can be plotted in the so-called *Arrhenius plot* as $\ln(e_n/T^2)$ as a function of $1/T$. This plot should produce a straight line, referred to as *trap signature*. By linear fitting the signature, it is possible to extract the apparent activation energy and apparent capture cross section as the slope and intercept of the curve, respectively. It is important to note that the activation energy and capture cross sections extracted by this method are only *apparent*, as they also contain other terms, according to Equations 1.20 and 1.21. Nonetheless, their values are often used to characterize and catalogue defects in a variety of semiconductors.[84]

Transient response: theory and experiments

The dynamic behaviour of the occupancy of a deep level is determined by competing emission and capture processes. Assuming an n-type semiconductor, electrons are emitted and holes are captured by the n_t states occupied by electrons, and electrons are captured and holes are emitted by the $N_t - n_t$ unoccupied states. This yields the differential equation[84]

$$\frac{\mathrm{d}n_t}{\mathrm{d}t} = (c_n + e_p)(N_t - n_t) - (e_n + c_p)n_t = a(N_t - n_t) - bn_t \tag{1.22}$$

Where $a = (c_n + e_p)$ and $b = (e_n + c_p)$ represent the sum of all electron gain and electron loss processes, respectively. The general solution of Equation 1.22 is[84]

$$n_t(t) = \frac{a}{a+b} N_t - \left\{\frac{a}{a+b} N_t - n_t(0)\right\} \exp[-(a+b)t] \tag{1.23}$$

Where $n_t(0)$ is the trap occupancy at time $t = 0$. The occupancy in steady state can be calculated by setting $t = \infty$, yielding $n_t(\infty) = \frac{a}{a+b} N_t$, so that Equation 1.23 can be written as

$$n_t(t) = n_t(\infty) - \{n_t(\infty) - n_t(0)\} \exp(-t/\tau) \qquad 1.24$$

where τ is the time constant given by $\tau^{-1} = (a + b) = e_n + c_n + e_p + c_p$. Equation 1.24 indicates that if a perturbation brings the trap concentration from equilibrium to a perturbed state with occupancy $n_t(0)$, the system will evolve exponentially returning back to the equilibrium concentration with a time constant $(a + b)^{-1}$, which takes into account all the emission and capture processes. It is important to note that in many cases one studies a system where one of the four processes dominates over the others. For example, if the dominant process is electron emission, then the time constant can be approximated to $\tau = e_n$.

The transient behaviour of Equation 1.24 is the basis of the experimental techniques that use time transient measurements to investigate deep levels. The most commonly used is Deep Level Transient Spectroscopy (DLTS), and its working principle is depicted in **Figure 1.16a**. This technique requires the use of a rectifying junction, either p-n or Schottky. Here, we will assume that the material contains only one type of deep level, acting as an electron trap. The capacitance of the junction is monitored over time (bottom panel in figure) while voltage pulses are applied to it (top panel). The steady state capacitance $C(\infty)$ corresponds to a reverse voltage $-V_r$. During the pulse excitation of length t_f, the voltage is abruptly increased up to near 0 V. This causes the collapse of the depletion region, with a consequent increase in the device capacitance. During the pulse, carriers are able to access the region that was previously depleted, and part of them are trapped by deep levels. After the pulse, the initial depletion region width is restored, but the capacitance initially reaches a lower value than the steady state $C(\infty)$, by a quantity ΔC_0. The reason is that the trapped carriers do not leave instantaneously the depletion region, causing an initial deficiency of electrical charges, which induce a lower capacitance. These trapped carriers are then thermally emitted from the deep levels, leading to a relaxation of the capacitance to its steady-state value $C(\infty)$. The resulting capacitance transient follows an exponential behaviour, which has the same time constant as the emission from the deep levels in the depletion region. The time dependence of the capacitance transient can be described by[84]

$$C(t, T) = C(\infty) + \Delta C_0 \exp(-t/\tau(T)) \qquad 1.25$$

where we made explicit the temperature dependence of τ, which is described by Equation 1.19. The DLTS procedure consists of measuring such capacitance transients as a function of temperature, so to obtain the temperature dependence of τ, which in this case describes an electron emission process, i.e., $\tau = e_n^{-1}$. This allows to reconstruct the Arrhenius plot, as described in the previous section, and to extract the trap parameters.

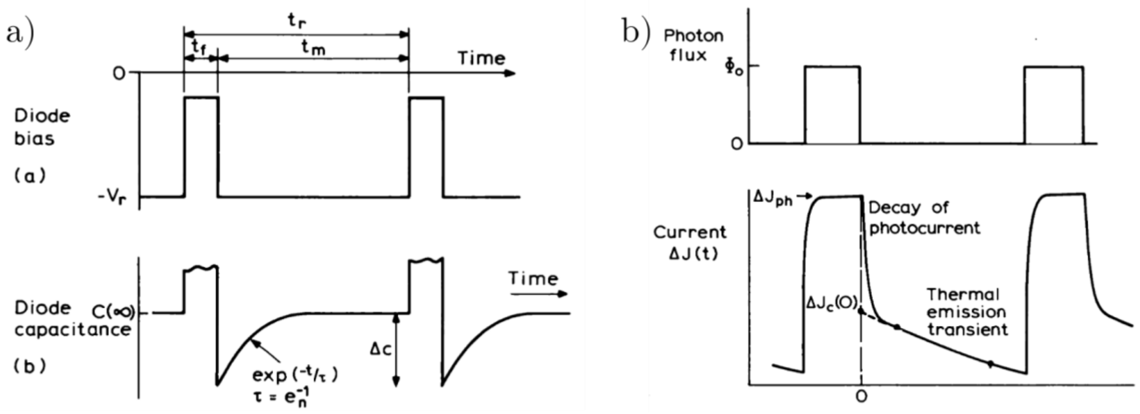

Figure 1.16 Schematic representation of **(a)** capacitive transients and **(b)** photocurrent transients, that are be used to investigate deep levels by DLTS and PICTS, respectively. The top panels represent the time dependence of the excitation, bias for capacitance, and light for photocurrent. Adapted from ref.[84]

A similar investigation can be carried out by measuring photocurrent transients as a function of temperature. In this case, the technique is referred to as Photoinduced Current Transient Spectroscopy (PICTS).[85,86] This technique presents more challenges in the data analysis with respect to DLTS, but it has two advantages: it can be performed also on Ohmic devices (i.e., a junction is not required), and, as opposed to DLTS, it can be performed on high resistivity materials (i.e. $\rho > 10^8$ Ωcm). The working principle of PICTS is depicted in **Figure 1.16b**. In this case, the excitation consists of pulses of light with flux Φ_0 (top panel in figure), which induce photocurrent transients (bottom panel). The photocurrent is collected thanks to an electric field E, which can be either applied by an external bias or be the built-in field of a depletion region. Also in this case, we will assume the presence of only one electron-trapping deep level. The light pulses cause the excitation of electrons from the valence to the conduction band, some of them are collected at the contacts, and others are trapped at deep levels. The equilibrium between generation, collection, and trapping leads to a steady-state photocurrent J_{ph}. When light is turned off, the current shows a first rapid drop due to band-to-band recombination of photo-excited carriers. Then, a slower transient appears, due to the injection in the conduction band of electrons that are thermally emitted by the deep levels, and give an additional contribution to the current. As for DLTS, this transient is an exponential with a characteristic time $\tau = e_n^{-1}$. The equation that describes the photocurrent transient is[84,86]

$$J(t,T) = J(\infty) + eE\mu_n\tau_n n_t(0)\frac{1}{\tau(T)}\exp(-t/\tau(T)) \qquad 1.26$$

where $J(\infty)$ is the steady-state dark current value, μ_n and τ_n are the electron mobility and lifetime. We note that in this case the emission time appears also in the pre-exponential factor, as opposed to the case of capacitive transients. In a similar fashion to DLTS, the PICTS procedure consists of performing photocurrent transient measurements as a function of temperature to reconstruct the Arrhenius plot of the deep level from the temperature dependence of τ.

Both DLTS and PICTS measurements are analysed using the so-called rate-window method, which will be described in detail in Chapter 2. For the moment, it suffices to say that this method allows to extract from the raw data a capacitance (for DLTS) or current (for PICTS) signal as a function of temperature. This is usually referred to as DLTS or PICTS spectrum, and it shows a peak for each deep level in the material. The peaks of these spectra shift in temperature by changing the time parameters used for the analysis, allowing to reconstruct the Arrhenius plot of the deep levels.

1.4.2 Defects in metal halide perovskites

Experimental and computational investigation of defects is one of the most active fields in the scientific research on MHPs. The reason is that defect identification and passivation is key to unlock the full potential of MHP-based optoelectronic devices like solar cells, detectors and LEDs.[87] This section contains a brief overview of some important results reported in the literature about defects in MHPs.

Many computational studies have focussed on the identification of the activation energy of electronic states introduced by common crystalline defects in MHPs. As an example, **Figure 1.17a** shows the position of defect levels in $MAPbI_3$ obtained by Meggiolaro et al.[88] via density functional theory (DFT) calculations. This particular study predicted that the only defects to introduce electronic states within the bandgap are the lead vacancy (V_{Pb}), and the iodine interstitial (I_i). All other defects introduce energy levels that lie within the conduction or valence band, and, therefore, are not expected to cause decrease in opto-electronic performance. Similar calculations can be found in the literature for virtually any MHP composition.[87,89,90]

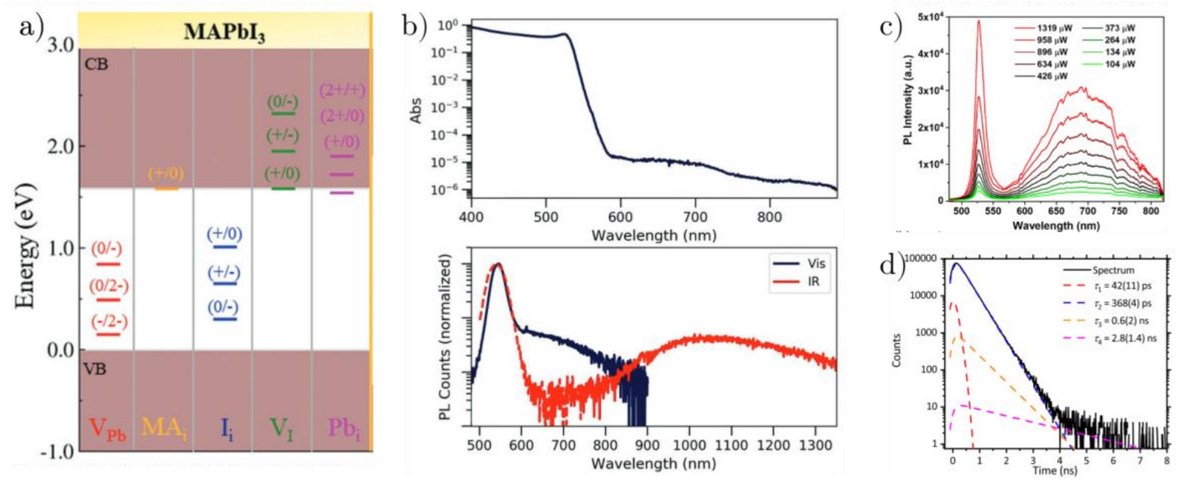

Figure 1.17 a) DFT-calculated position of the defect states introduced by the most stable defects in MAPbI$_3$. Adapted from ref.[89]. **b)** Absorption (top) and PL (bottom) spectra of MAPbBr$_3$, showing two emissive defect states, one around 700 and the other around 1100 nm. Adapted from ref.[89] **c)** PL spectrum of a PEA$_2$PbI$_4$ single crystal showing a defect-related sub-gap broadband emission. Adapted from ref.[90]. **d)** Positron annihilation lifetime spectrum of a MAPbI$_3$ single crystal, with the fitted positron lifetime components. Adapted from ref.[91].

Defects in MHPs have been observed by both absorption and photoluminescence measurements. **Figure 1.17b** shows the absorption spectrum (top panel in figure) of a MAPbBr$_3$ sample measured by Motti et al.[89] Observing the spectrum in semi-log scale reveals two absorption features with intensity 5 to 6 orders of magnitude lower than the band-to-band absorption edge. The features are both quite broad, the first one covers the range between 600 and 800 nm, the second one between 750 and 900 nm. The PL spectra in the visible and infrared of the same sample (bottom panel in figure) show two emissive bands centred at around 700 and 1100 nm. These were assigned by the authors to radiative recombination of trapped carriers.

Photoluminescence was also used to study trap states in 2D perovskites. As an example, **Figure 1.17c** shows the PL spectrum of a PEA$_2$PbI$_4$ single crystal. The narrow-band emission by exciton recombination is accompanied by a broadband sub-gap emission, which the authors attributed to defect-related luminescence centres.[90]

Figure 1.17d shows a recent result of defect characterization in MAPbI$_3$ single crystals by positron annihilation spectroscopy. This technique is able to probe positively charged vacancies in the lattice, which for MAPbI$_3$ correspond to MA and Pb vacancies. Positrons get trapped at these vacancies, and the measurement of their annihilation lifetime gives information on the defect type, and can indicate a minimum defect density.[91] The results showed evidence for trapping at Pb vacancies, while no trapping at MA vacancies was observed. The authors obtained a minimum lead vacancy defect concentration of $3 \cdot 10^{15}$ cm^{-3}.

Electrical characterization at room temperature

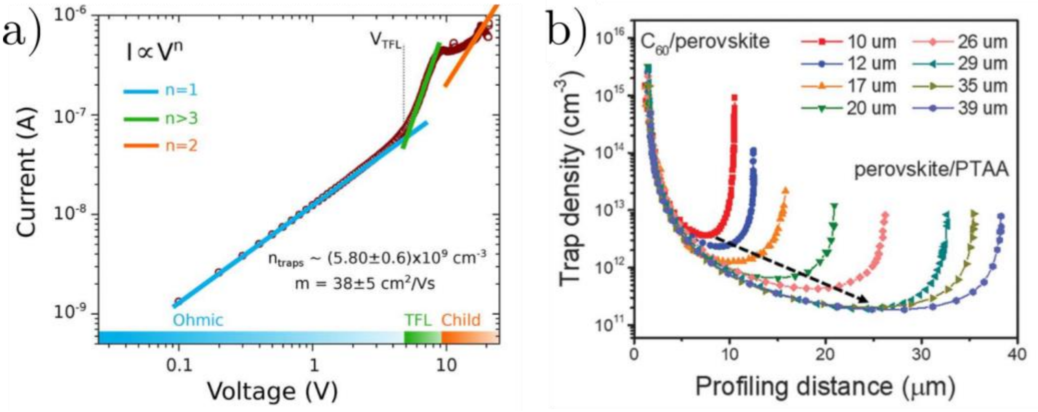

Figure 1.18 a) SCLC measurements of a $MAPbBr_3$ single crystal device, where the Ohmic, trap-filled limited and Child regimes are highlighted. In the graph are reported the obtained values of trap concentration and mobility. Adapted from ref.[49]. **b)** Results of capacitance-voltage profiling on $MAPbI_3$ thin films, showing the trap density as a function of the depth in the film, for different film thicknesses. Reproduced from ref.[92].

Two of the most widely adopted room-temperature techniques to characterize defects in MHPs are space-charge-limited current (SCLC) and capacitance-voltage profiling measurements. **Figure 1.18** shows two examples from literature.[49,92]

Figure 1.18a shows a SCLC measurement on a $MAPbBr_3$ single crystal. This technique should be performed using electron-only or hole-only electrical contacts, so that only one kind of charge carrier can flow in the circuit. At low voltages, the current-voltage (I-V) characteristic shows the expected Ohmic linear regime, with $I \propto V$. At around 5 volts, the current shows a non-linear dependence $I \propto V^n$, with $n > 3$. This regime is called *trap-filled limited* (TFL), and occurs when all the available trap states are filled by the injected carriers.[49] The onset voltage of such regime (V_{TFL}) is proportional to the trap concentration n_t. From this value the authors extrapolated an exceptionally low trap density of $n_t = 5.8 \cdot 10^9$ cm^{-3} for this $MAPbBr_3$ single crystal. For even higher voltages, the sample enters in a Child regime, with $n = 2$. From this regime it is possible to extract the carrier mobility, which in this case is 38 cm^2/Vs.

Capacitance-voltage (C-V) profiling consists of measuring the capacitance of a p-n or Schottky junction as a function of the applied voltage. As the reverse voltage increases, the depletion width increases, probing more and more in depth the material. In fact, from the reverse voltage it is possible to extract the depletion layer width, which corresponds to the depth probed within the semiconductor, usually named *profiling depth*. As the reverse voltage increases, also the capacitance changes. This is due to a change in geometric capacitance (the depletion width gets larger, so the geometric capacitance decreases), but also to the depletion of both free and trapped carriers. From the analysis of the capacitance-voltage curve it is then possible to extract the free carrier concentration and the trap concentration, which can then be plotted as a function of the profiling depth, for a spatially-resolved measurement. **Figure 1.18b** shows the result of a C-V profiling of $MAPbI_3$ thin films of different thickness.[92] The profiling depth values well match with the nominal thickness of the films, demonstrating the validity of the model. The authors found the interface with the contacts to show a 1 to 2 orders of magnitude higher trap concentration than the bulk. They also found thicker films to have a lower trap concentration, probably due to higher strain relaxation. In general, they calculated bulk the trap concentration in the range $10^{11} - 10^{13}\ \mathrm{cm}^{-3}$, and the interface trap concentration in the range $10^{13} - 10^{15}\ \mathrm{cm}^{-3}$.

The limit of room temperature techniques is that typically they only yield information on the overall trap density, without the possibility of discerning between the different traps. Also, they are not able to yield trap parameters such as the activation energy and capture cross section. Moreover, Siekmann et al.[93] recently published a review paper comparing many literature results on trap concentration measured by SCLC and C-V profiling, and found that most values fall close to the detection limits of the techniques. This suggests that most values reported in literature should be considered as an upper limit of trap concentration, rather than actual trap concentrations.

Temperature-dependent techniques

Temperature-dependent techniques constitute the most powerful and sensitive tools for defect characterization in semiconductors,[84] providing the possibility of discerning among different types of trap states, and determining their physical parameters. These techniques are frequently referred to as *defect spectroscopies*, where the “spectroscopy” term is referred to a sweep in temperature, instead of the more typical sweep in photon wavelength. Researchers have performed a variety of defect spectroscopy measurements on several MHPs devices. In the following, I will present a brief overview of the most relevant defect spectroscopy techniques, and how they have been applied to MHP devices.

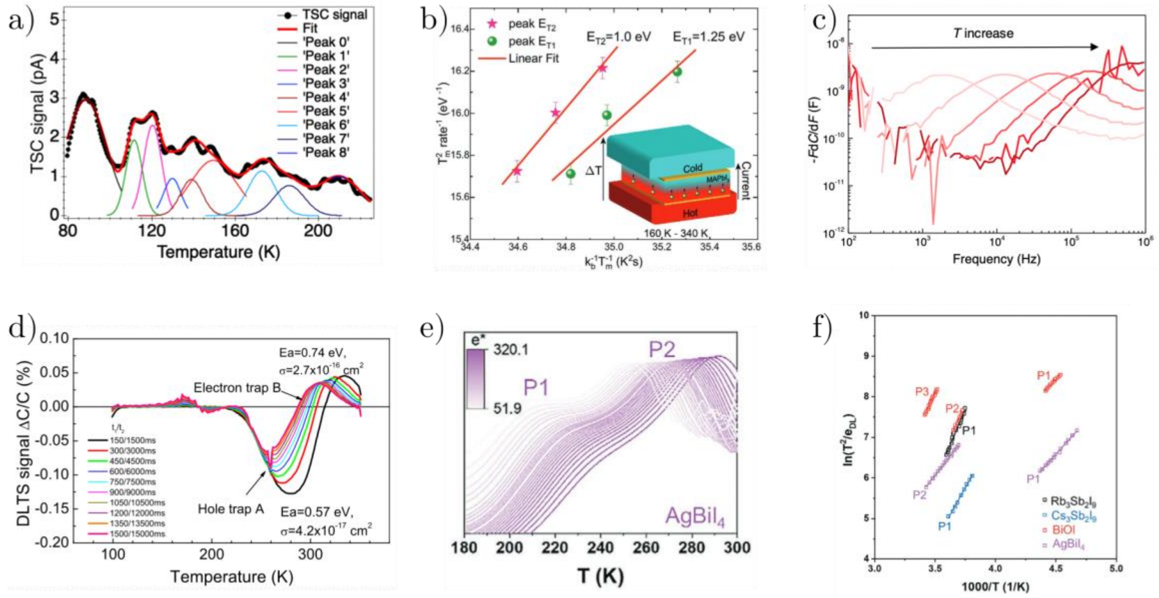

Figure 1.19 a) TSC spectrum of a $CsPbCl_3$ single crystal (black dots) with the fitting components (thin solid lines) and the total fit (thick red solid line). Reproduced from ref.[94]. **b)** Arrhenius plots of two trap states obtained by TEES measurements on a $MAPbI_3$ single crystal. The bottom right corner shows a schematic representation of the TEES measurement. Reproduced from ref.[95]. **c)** TAS spectra of a Cs-doped $FA_{0.9}MA_{0.1}PbI_xBr_{1-x}$ solar cell. Reproduced from ref.[96]. **d)** DLTS spectra of a $Cs_x(MA_{0.17}FA_{0.83})_{(1-x)}$ $Pb(I_{0.83}Br_{0.17})_3$ solar cell, identifying an electron trap state and a hole trap state. Reproduced from ref.[97] **e)** PICTS spectra of a solar cell based on $AgBiI_4$, a lead-free perovskite-inspired material (PIM). Reproduced from ref.[98]. **f)** Arrhenius plot extracted from the PICTS spectra in (e), as well as from the PICTS spectra of other PIMs. Reproduced from ref.[98].

One of the simplest and oldest temperature-dependent techniques is thermally-stimulated current (TSC). A sample with two electrical contacts is cooled down to cryogenic temperatures, and an above-gap optical excitation is used to fill its trap states. Being at low temperature, the defect states remain occupied, since carriers cannot be emitted. Then, a temperature ramp is started, while the dark current is monitored. As temperature increases, carriers are thermally emitted by the traps, generating peaks in the current versus temperature plot (the TSC spectrum). Each peak corresponds to a specific trap state, and, by analysing the peak location and height, it is possible to extract activation energy, capture cross section, and concentration of each trap state. **Figure 1.19a** shows the TSC spectrum of a $CsPbCl_3$ single crystal, fitted by nine different components, each corresponding to a different trap state.[94] One of the limitations of the TSC technique is that it relies on fitting procedures that contain many parameters, which may lead to large errors in the parameters estimation. Another limitation is that it needs low dark current background, so typically it is only suited for high resistivity materials, and loses sensitivity at high temperatures, where dark current increases.[84]

A similar technique to TSC was recently applied by Musiienko et al. on $MAPbI_3$ single crystals is thermoelectric effect spectroscopy (TEES).[95] A schematic of the TEES setup is represented in the inset of **Figure 1.19b**. As for TSC, the defect states in the sample are optically filled at cryogenic temperatures, then a temperature ramp is started with a fixed rate, while the dark current is monitored. A temperature gradient is set across the sample by the use of cold and hot fingers. As temperature increases, thermally de-trapped carriers move to the contacts due to the thermal gradient, via thermoelectric effect, producing peaks in the current. The sign of the peaks reveals if the traps are for electrons or holes, since the two charge carriers flow in opposite directions in a temperature gradient. Repeating the experiment with different heating rates allows to reconstruct the Arrhenius plots, as shown in **Figure 1.19b** for $MAPbI_3$, where the authors identified two trap levels. The method allows to extract activation energy, capture cross section, and concentration of the traps. One of the disadvantages of this method is that it requires to perform one temperature ramp for each point in the Arrhenius plot. This makes the measurement long to perform, especially to obtain Arrhenius plots with many points, which is required to obtain reliable trap parameters.[99] Typically, this method is applied to high resistivity materials, where DLTS is not applicable.[100]

A widely adopted method for defect characterization in MHPs is Thermal Admittance Spectroscopy (TAS). This method consists of measuring admittance (often also called *impedance*) spectra at different temperatures. An admittance spectrum consists of a measurement of the admittance (inverse of the impedance) of a device, typically via lock-in detection, as a function of the frequency ω of the oscillating voltage applied to it. An example is reported in **Figure 1.19c** for a Cs-doped $FA_{0.9}MA_{0.1}PbI_xBr_{1-x}$ solar cell.[96] From the admittance it is possible to obtain the device capacitance C, if an equivalent circuit that describes the system is known. The plot of $-\omega \mathrm{d}C/\mathrm{d}\omega$ as a function of ω yields peaks centred at the characteristic frequencies of trap emission. Such peaks shift with temperature, and allow to reconstruct the Arrhenius plots of the traps. The method allows to obtain activation energy, capture cross section, and concentration of the defects. However, it does not allow to distinguish between electron and hole traps.

Figure 1.19d shows DLTS spectra of a $Cs_x(MA_{0.17}FA_{0.83})_{(1-x)}Pb(I_{0.83}Br_{0.17})_3$ solar cell. It is possible to observe both positive and negative peaks in the spectra. If the doping of the semiconductor is known, from the sign of the DLTS peaks it is possible to extract if the relative trap is either for electrons or holes. In addition, DLTS allows to extract activation energy, capture cross section, and concentration of the defects. This technique is the most powerful one for defect characterization in semiconductors. However, it typically fails for high resistivity materials,[85,101] and can only be applied to devices with a rectifying junction.

Finally, **Figure 1.19e** shows recent results by Pecunia et al.[98] of a PICTS characterization on lead free perovskite-inspired materials (PIMs). In particular, the spectra show two defect states in a $AgBiI_4$ solar cell. **Figure 1.19f** shows the corresponding Arrhenius plots, along with those measured by the authors on other PIMs. PICTS allows to obtain activation energy, and capture cross section of the trap states. Also defect concentration can be extracted, although the procedure is more complicated than DLTS, as it requires additional optoelectronic measurements.[102] Historically, PICTS was used mainly to characterize high resistivity materials, such as CdTe and CdZnTe, where DLTS characterization fails.[101,103,104] We note that PIMs cannot be classified as perovskites from a crystallographic point of view, therefore, to date, no PICTS characterization on MHPs was ever reported in the literature. However, PICTS is promising technique for certain types of MHPs, especially bulk single crystals, that typically show high resistivity and are not suited for DLTS characterization. In this thesis work, we applied the PICTS technique for the first time to both 2D and 3D MHP single crystals.

1.4.3 Interplay between electronic defects and ionic motion

The mixed electronic/ionic nature of charge transport in MHPs introduces severe complication in the analysis and interpretation of temperature-dependent measurements. Since 2019, the two research groups of Carsten Deibel[105–108] and Bruno Ehrler[61,109–111] have been publishing research papers on DLTS and TAS measurements on MHP solar cells, interpreting the measured defect signatures in terms of ion migration, instead of electronic defects. This is based on the interpretation of the capacitance transients of DLTS as due to ion migration in the depletion region, instead of electron de-trapping. Such interpretation was already applied to DLTS measurements that were carried out in the ‘90s on inorganic semiconductors such as Si,[112] CdTe, and CdHgTe,[113] containing ionic mobile impurities. The physical model that was proposed is as follows. During a DLTS measurement, mobile ionic impurities respond to the bias pulses moving the in the depletion region. When the device is under reverse bias all ions are accumulated at the edge of the depletion region. During the bias pulse, the internal field is nullified, so that ions redistribute uniformly in the region that was previously depleted. In this regime, diffusion dominates, as there is no internal electric field. After the bias pulse is terminated, the electric field is re-established, and ions drift back to the edge of the depletion region. This ionic drift induces exponential capacitive transients that can appear completely identical to the ones observed upon emission of carriers from electronic defect states. The characteristic time of the exponential decay can be described by[61,106,113]

$$\frac{1}{\tau} = e_t = \frac{e^2 N_D}{\varepsilon\varepsilon_0 k_B T} D = \frac{e^2 N_D}{\varepsilon\varepsilon_0 k_B T} D_0 \exp\left(-\frac{E_a}{k_B T}\right) \qquad 1.27$$

where N_D is the doping density of the semiconductor, which can be estimated by analysis of the C-V characteristics of the diode. D is the diffusion coefficient of the ionic species, whose temperature dependence was made explicit by means of Equation 1.6. In this picture, e_t represents a *migration rate*, rather than an emission rate. Equation 1.27 yields an Arrhenius behaviour of e_t, comparable to that of the emission rate of trapped carriers, described by Equation 1.19. By fitting such Arrhenius plot, it is possible to extract the parameters for ion diffusion: the diffusion coefficient at infinite temperature D_0 and the activation energy for ion migration E_a. Finally, by the height of the DLTS peaks, it is possible to extract the concentration of the ionic impurities. When DLTS measurements yield ion migration parameters according to this model, the technique is renamed Transient Ion Drift (TID). **Figure 1.20a** shows an example of a TID measurement characterizing Cu migration in a Si sample.[112] This measurement allowed the authors to extract the diffusion coefficient of such impurity as a function of temperature, and well fits with results obtained by other techniques on similar samples.

The similarities of the exponential capacitive transients to the Arrhenius behaviour of e_t for both electronic defects and ion migration can complicate the assignment of the features observed in mixed electronic/ionic conductors. However, a distinction between the two physical phenomena can be achieved by performing a reverse-DLTS (r-DLTS) measurement. This consists of a DLTS measurement where the order of the voltage pulses represented in **Figure 1.16a** is reversed. In this way, the analysed capacitive transient is relative to the ion *diffusion*, rather than its drift, as it occurs when the internal field of the depletion region is nullified. Since the drift time constant is typically equal or greater than the diffusion time constant, if ion migration is the dominant phenomenon, we expect $\tau_{DLTS} \geq \tau_{r-DLTS}$. In samples where electron trapping and de-trapping are the dominant processes, DLTS measurements yields the time constant for carrier *de-trapping*, while r-DLTS for carrier *trapping*. Since trapping is typically a much faster process than de-trapping, in this case we expect $\tau_{DLTS} \ll \tau_{r-DLTS}$,[106,112] i.e., the opposite of the case where ion migration dominates.

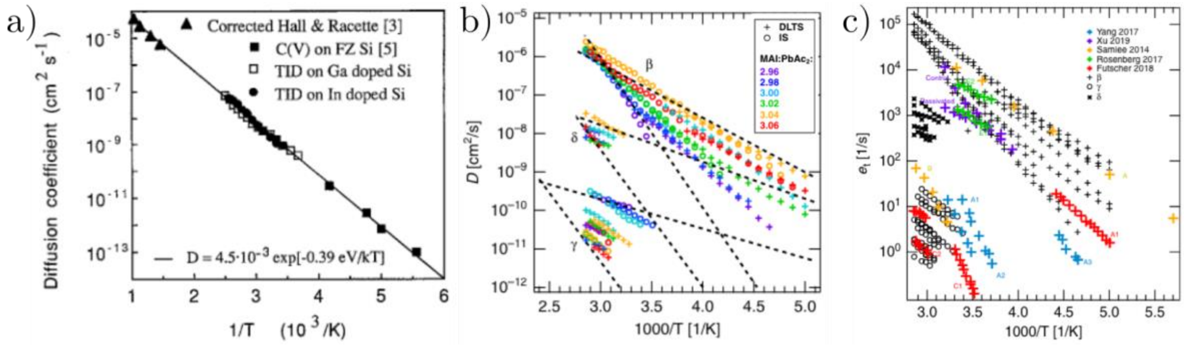

Figure 1.20 a) Diffusion coefficient of Cu in Si as a function of temperature measured by TID, along with a comparison with literature results obtained by different techniques (triangles and filled squares). Reproduced from ref.[112]. **b)** Diffusion coefficient as a function of temperature measured by DLTS (TID) and TAS on $MAPbI_3$ solar cells grown with different stoichiometric ratios $MAI:PbAc_2$. Adapted from ref.[106]. **c)** Comparison of migration rates reported in literature by DLTS and TAS measurements with the TID results by Reichert et al.[106], showing virtually all results fall under the same three categories. Reproduced from ref.[106].

The groups of Deibel and Ehrler performed this test on MHP samples, and found that for virtually any MHP composition the result was $\tau_{DLTS} \geq \tau_{r-DLTS}$, implying an ionic nature of the capacitive transients in MHP solar cells. **Figure 1.20b** shows the results of Reichert et al.[106] of the TID characterization on $MAPbI_3$ solar cells, yielding the diffusion coefficients as a function of temperature of three migrating ionic species, labelled β, γ, and δ.[106] The authors repeated the experiments with different stoichiometries of the $MAPbI_3$ precursors, in order to purposedly create MA and I vacancies. Based on these results they attributed β to V_{MA}^-, γ to MA_i^+, and δ to I_i^-. It is important to note that these charged species also introduce electronic defects in the material. However, they are also able to move inside the perovskite lattice, and the above-mentioned results show that such motion completely hides the signals coming from the electronic defects. In the same paper, Reichert et al. compared their TID signatures with the DLTS signals measured by various research groups on solar cells based on a variety of MHPs. This comparison is reported in **Figure 1.20c.** They found that virtually all trap signatures reported in literature and assigned to electronic defects well match with their ion migration signatures β, γ, and δ. Based on this, they suggest that most signatures that were previously attributed to defect states are more likely related to migrating ions. Several recent publications from other groups, who performed a comparison of DLTS and r-DLTS measurements, confirmed this conclusion.[114–118] However, we note that this interpretation is still not widely accepted, and several research groups still interpret defect spectroscopy signatures as originating from electronic defect states.[83,119,120]

In a recent review paper,[121] C. Deibel and M. Futscher generalized their results on DLTS, proposing that all defect spectroscopy techniques, when applied to MHPs, are more likely to yield ion migration parameters, rather than electronic defect ones. Among these techniques, in addition to DLTS, they included TAS, PICTS, Intensity Modulated Photocurrent Spectroscopy (IMPS), and others. However, they did not enter in the details of how ionic motion can affect light-modulated techniques like PICTS and IMPS, whose working mechanism is completely different with respect to voltage-modulated techniques like DLTS. In this thesis work, we found that, indeed, PICTS characterizes ionic motion rather than electronic defects, at least in 3D MHPs, and we developed a model to explain the underlying physical origin of this effect.

1.5 Applications

As discussed above, MHPs show great promise as active materials in a variety of optoelectronic devices. In this section I will focus on the two main applications involved in this thesis work, i.e., solar cells and photodetectors.

1.5.1 Solar cells

Solar cells are probably the strongest driving force towards research in MHPs. The record efficiency of perovskite solar cells (PSCs) has shown a steep increase from 14.1% in 2013 up to 25.5% in 2022.[1] What enabled such steep growth were the exceptional optoelectronic properties of MHPs, combined with materials engineering (morphology, compositional tuning, control of grain size and orientation), and defect management (passivation, engineering of extracting layers).[87]

In PSCs, the photo-generated electrons and holes are generated in the perovskite layer, which is considered as intrinsic (i.e. with no doping), and are then collected at the two contacts. To maximize charge extraction, one contact material has the conduction band (CB) edge aligned with the perovskite CB edge, to efficiently collect electrons, and the other has the valence band (VB) edge aligned with the perovskite VB edge, to efficiently collect holes. The former contact is often called electron transport layer (ETL), and the latter hole transport layer (HTL). **Figure 1.21a** shows a schematic (left panel) and the band diagram (right panel) of the PSC that recently achieved the record efficiency of 25.5%.[122] In this particular structure, the perovskite composition is $FAPbI_3$:0.38$MDACl_2$ (where $MDACl_2$ is methylenediamine dihydrochloride) with a small amount of KI doping, the ETL consist of a SnO_2 thin film, while the HTL of a Spiro-OMeTAD thin film. In this work, the authors improved the ETL/perovskite interface by introducing a coherent interlayer formed by a Cl-containing $FAPbI_3$ perovskite precursor.

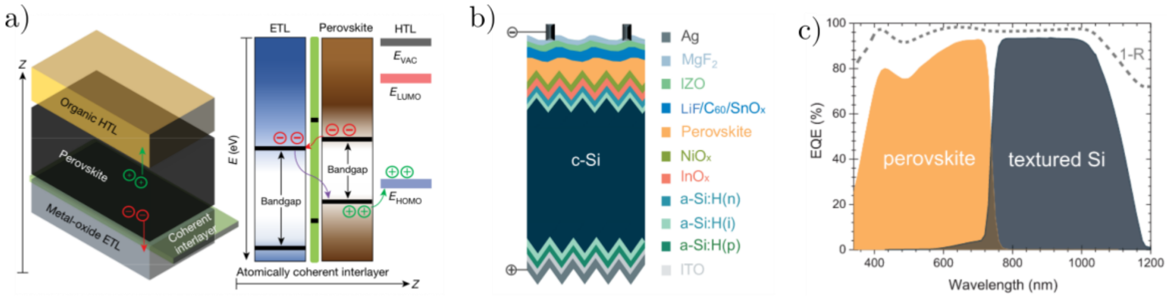

Figure 1.21 a) Schematic of the layers composing the perovskite solar cell achieving record efficiency of 25.5% efficiency. Reproduced from ref.[122]. **b)** Schematic of the layers composing a Si/perovskite tandem solar cell with certified efficiency of 25.7%. Reproduced from ref.[123] **c)** External quantum efficiency spectra of the perovskite (orange area) and textured Si (black area) layers. Reproduced from ref.[123].

MHPs show also great promise as top cells for tandem solar cells. Perovskite/Silicon tandem solar cells achieved record efficiencies as high as 32.5%.[1] **Figure 1.21b** shows the structure of a perovskite/Silicon tandem solar cell fabricated at the KAUST Solar Center.[123] The bottom part of the cell consists of a textured Silicon heterojunction solar cell, the top part is a $Cs_{0.05}MA_{0.15}FA_{0.8}PbI_{2.25}Br_{0.75}$ perovskite solar cell with NiO_x as HTL, and a stack of $LiF/C_{60}/SnO_x$ as ETL. The advantage of a perovskite/Si tandem solar cell is represented in **Figure 1.21c**, showing the external quantum efficiency spectra of the Si cell (black area), and perovskite cell (orange area). The Si cell efficiently harvests photon energies in the infrared part of the spectrum, while the perovskite cell harvests the visible photon energies. A combination of the two in a tandem solar cell allows to enhance the overall photo-conversion efficiency by gathering a larger portion of the solar spectrum. Complicated structures, consisting of a stack of several layers like the ones of tandem solar cells, are typically prone to thermal and mechanical issues under working conditions. For example, strain and mismatch of thermal expansion coefficients of the different layers can lead to problems like delamination of the solar cell. In this work, we investigated the delamination problem in perovskite/Si tandems, to identify the interface causing this effect.

1.5.2 Photo-detectors

Photon detection is at the basis of modern technologies like telecommunications, LIDARs, industrial inspection, medical imaging, internet of things, and many others. MHPs have proven to be excellent active material for photo-detection applications in a broad wavelength range, from the near-infrared up to γ-rays. MHP photodetectors are typically found in both thin film and single crystal form.

Figure 1.22a shows the detectivity spectrum of a thin film photodetector with narrowband response based on $MAPbI_2Br$.[124] MHP thin film photodetectors usually present the same architecture as MHP solar cells, i.e. a junction with ETL and HTL extraction layers. The inset of **Figure 1.22a** shows the architecture of this particular device.

An important field of photo-detection where MHPs show promising results is ionizing radiation detection (i.e. UV, X-rays and γ-rays). **Figure 1.22b** shows the linear attenuation coefficient as a function of photon wavelengths for two widely adopted inorganic semiconductors for ionizing radiation detection (Si and CdTe), compared with that of $MAPbBr_3$ and PEA_2PbBr_4. This parameter is related to the material's stopping power of high-energy photons. The comparison demonstrates that the two MHPs have similar stopping power to CdTe for both soft and hard X-rays, and, on average, one order of magnitude higher than commercially available Si. The main reason for such a high attenuation coefficient of MHPs is the presence of a heavy element like Pb in the perovskite structure. This, combined with the excellent opto-electronic properties of MHPs, allowed X-ray detectors to reach record sensitivities of up to 10^5 $\mu CGy^{-1}cm^{-2}$ with both thin film and single crystal detectors.[2] This value tops the record sensitivities achieved by organic solar cells by one order of magnitude, and the one of commercially available poly-CdZnTe detectors by more than 2 orders of magnitude.[2] Such record sensitivities have been achieved by devices based on 3D perovskites like $MAPbBr_3$[50] and $MAPbI_3$.[125] We note, however, that such high sensitivity is possibly related to photoconductive gain effect.[2,126,127] This allows to attain high sensitivity, but, at the same time, increases the response time, posing a significant obstacle for applications that require fast response times, such as imaging.

Recent studies showed also promising results on 2D perovskite materials such as PEA_2PbBr_4. **Figure 1.22c** shows the photocurrent response of a PEA_2PbBr_4 thin film detector to 150 keV hard X-rays.[128] This device showed a sensitivity of 806 $\mu CGy^{-1}cm^{-2}$, more than two orders of magnitude lower than that achieved by the best 3D MHP devices, however it achieved an extremely low limit of detection (LoD) of 42 nGy/s, thanks to its low dark current.

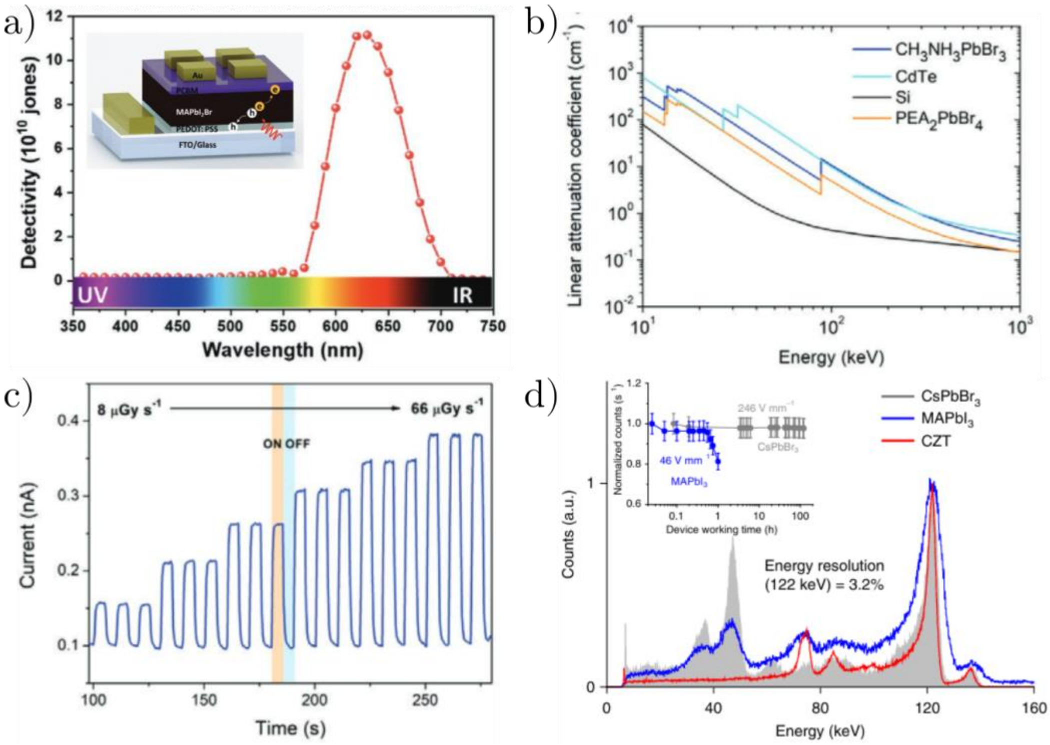

Figure 1.22 a) Detectivity spectrum of a narrowband thin film photodetector based on $MAPbI_2Br$. Adapted from ref.[124]. **b)** Linear attenuation coefficient as a function of photon energy for CdTe, Si, $MAPbBr_3$, and PEA_2PbBr_4. Reproduced from ref.[128]. **c)** Photocurrent response of a PEA_2PbBr_4 thin film to X-ray radiation for different dose-rates. Reproduced from ref.[128]. **d)** γ-ray spectrum of a ^{57}Co source measured by CdZnTe, $MAPbI_3$, and $CsPbBr_3$ detectors. The inset shows the temporal stability of the response of the two MHP detectors. Reproduced from ref.[10].

Moving to even higher photon energies, **Figure 1.22d** shows the γ-ray spectrum of a ^{57}Co source measured by CdZnTe, $MAPbI_3$, and $CsPbBr_3$ single crystal detectors.[10] In general the all-inorganic MHP $CsPbBr_3$ shows better spectral response than the hybrid counterpart $MAPbI_3$, with performance comparable to commercial detectors, at least in specific spectral regions. Inorganic MHPs also show better long-term stability under constant γ-ray irradiation (see inset in the top left corner of the figure).

Due to the above-discussed large interest in ionizing radiation detection applications for MHPs, part of this thesis work was to characterize the effects of ionizing radiation on the photophysical properties and electronic defects of both 2D and 3D MHPs.

Chapter 2

Materials and methods

This chapter describes the experimental details of this thesis work. The first section explains the procedures for hybrid lead halide perovskite single crystal synthesis and device fabrication. The following sections describe the main experimental setups used in this work: Surface Photovoltage and Photoluminescence Spectroscopy, X-ray irradiation, Kelvin Probe Force Microscopy, and Photoinduced Current Transient Spectroscopy.

2.1 Synthesis and fabrication

In this thesis work, I focussed on the investigation of the optoelectronic properties of Br-based lead halide perovskites. I started by synthesizing methylammonium (MA) lead bromide ($MAPbBr_3$) single crystals, and phenethylammonium (PEA) lead bromide (PEA_2PbBr_4) single crystals. The latter falls in the category of "2-dimensional" perovskites. Both the synthesis and fabrication procedures were carried out at the Department of Physics and Astronomy (DIFA) of the University of Bologna and at Néel Institute (CNRS) and LITEN (CEA) in Grenoble, France. $MAPbBr_3$ synthesis was carried out in both institutes, while PEA_2PbBr_4 synthesis only at DIFA.

2.1.1 $MAPbBr_3$ single crystal synthesis

The crystal growth procedure for $MAPbBr_3$ single crystals follows the inverse temperature crystallization (ITC) procedure developed by Saidaminov et al.[129]. This procedure comes from the observation that methylammonium lead trihalide perovskites show a solubility decrease with increasing temperature inside specific solvents. Such behaviour is the opposite of the one observed in most materials, where crystallization occurs upon cooling rather than heating of the solution, hence the name of *inverse* temperature crystallization. $MAPbBr_3$ shows ITC behaviour when dissolved in *N,N* dimethylformamide (DMF), while for $MAPbI_3$ it was observed in γ-butyrolactone (GBL) or dimethylsulphoxide (DMSO)[129]. When perovskite precursors are dissolved in the appropriate solvent, spontaneous nucleation occurs upon heating, and perovskite crystals precipitate out of solution. The ITC method allows obtaining millimeter-scale single crystals, typically within 2 to 4 hours.

Single crystals of $MAPbBr_3$ (MA = CH_3NH_3) are synthesized from a solution of methylammonium bromide (MABr) and lead bromide ($PbBr_2$) powders dissolved in *N,N*-dimethylformamide (DMF), at a concentration of 1 mol/L in a 1:1 molar ratio. To fully dissolve the powders, the solution is stirred for 4 hours. It is then filtered by using a 0.22 µm PTFE filter to remove any insoluble particles. **Table 2.1** lists the purity and provider of the chemicals used for $MAPbBr_3$ single crystal synthesis in the two institutes where the procedure was carried out. The solution temperature during crystal growth was controlled by a Torrey Pines Scientific HP60A programmable hotplate at DIFA and by a ColdPlate programmable Peltier controller at Institut Néel/CEA.

	DIFA (Bologna)	Néel/CEA (Grenoble)
$PbBr_2$	≥ *98%* (Merck)	≥ *99.999%*, ultradry (Alfa Aesar)
MABr	≥ *99%*, anhydrous (Merck)	≥ *99.99%* , anhydrous (Greatcell Solar)
DMF	*99.8%*, anhydrous (Merck)	*99.8%*, Extra Dry over Molecular Sieve (Acros Organics)

Table 2.1 Precursors and solvents used for $MAPbBr_3$ single crystal synthesis in the two institutes where the growth procedure was carried out.

The crystal growth was carried out using two protocols, as reported by Amari et al.[130]: *unseeded* and *seeded* protocol.

Unseeded protocol

The unseeded protocol is schematized in **Figure 2.1**. The precursor solution, contained in a closed vial, is placed in an oil bath on a hotplate. A feedback thermocouple is placed inside the oil bath to monitor the temperature of the vial. The temperature of the solution is abruptly increased from room temperature to 85°C.

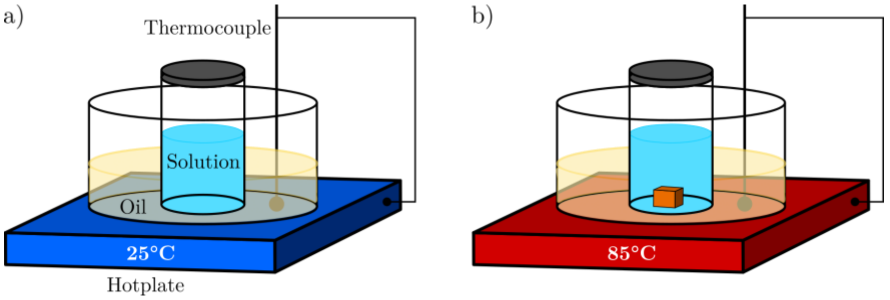

Figure 2.1 Unseeded synthesis procedure. a) The solution is placed in an oil bath on top of a hotplate with thermocouple feedback. b) The solution is abruptly heated up to 85°C and perovskite crystals precipitate at the bottom of the solution.

This causes the solubility to rapidly drop and crystallization is favoured. Typically, crystals first appear at the air-solution interface, which acts as a preferential nucleation site. Such small crystals are referred to as *seeds*. When seeds reach a critical mass, they precipitate at the bottom of the vial and continue their growth process. Typically, after 2 to 4 hours the crystal faces orthogonal to the growth direction reach dimensions of 2x2 up to 8x8 mm^2. When a crystal reaches the desired size, it can removed from the solution employing tweezers.

This process has the advantage of being relatively fast and easy to perform. On the other hand, it provides very little control over the outcome of the growth process. This is due to the quality of the seeds that spontaneously nucleate in the solution and have a strong impact on the final crystal quality. If a seed contains strain, it will propagate it to the single crystal. If a seed is polycrystalline, it will generate a polycrystal rather than a single crystal. Due to such uncertainty about the seed quality, the unseeded protocol suffers from poor reproducibility as far as crystal quality is concerned. Amari et al.[130] found that, among 30 crystals grown by this method, half of them were polycrystals. Among the single crystals, they found by polarized light microscopy that half of them were heavily strained. Thus, only one crystal out of four was found to be a single crystal without relevant strain.

Seeded protocol

The seeded protocol was proposed by Amari et al.[130] as an alternative and more reproducible method to the unseeded one. The idea behind this protocol is to externally provide a seed for the crystal growth rather than relying on the spontaneous formation of a seed in the solution. The first step of the procedure is to perform an unseeded growth as described in the previous paragraph. The seeds that form in the solution are removed before they grow larger than approximately 1x1 mm^2. The seeds are then inspected and only the ones with good crystal quality are kept (single-crystalline, with cubic shape and sharp edges). Ideally, one should also check under cross-polarized light that the seed does not contain internal strain.

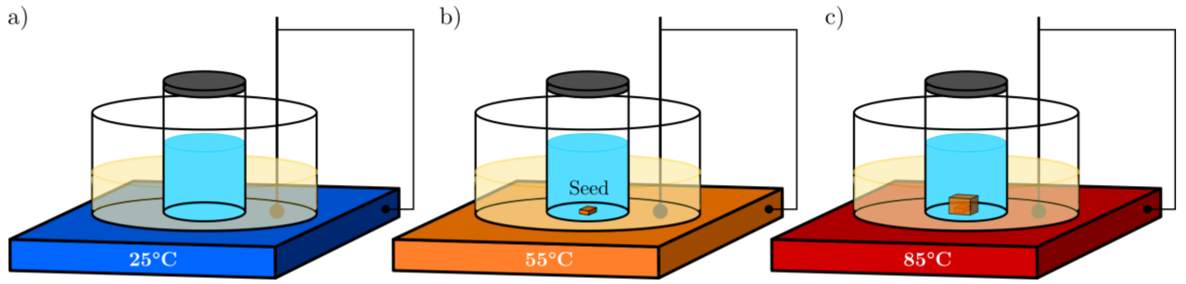

Figure 2.2 Seeded synthesis procedure. **a)** The solution is placed in an oil bath on top of hotplate with thermocouple feedback. **b)** The solution is heated up to 55°C and single crystal seed of controlled quality coming from a previous unseeded growth is placed in the solution. **c)** The seed acts as a nucleation site and a single crystal grows around it.

The following steps of the protocol are shown in **Figure 2.2**. A new solution is put on the hotplate at room temperature, being careful that the solution-air meniscus is slightly above the oil level. This causes the meniscus to be slightly colder than the rest of the solution and hinders the unwanted spontaneous nucleation of new seeds at the meniscus. The solution is heated up to 55°C and one of the previously grown seeds is placed inside the solution. At such temperature, the seed is in a metastable state where it is only slightly dissolved by the solvent. The temperature is then brought up to 65°C. A temperature ramp of 5°C/h with a setpoint of 85°C is set on the hotplate. During the ramp, the seed acts as a preferential nucleation site and thus it increases in size. Despite this, spontaneous nucleation in other parts of the solution may still occur, leading to the formation of other small crystals. After 4 hours the procedure is complete and the single crystal can be extracted from the solution.

Figure 2.3 summarizes the temperature profiles as a function of time for the unseeded and seeded procedures. It is clear how the unseeded procedure is much easier to carry out as it involves fewer steps. As discussed above, this comes at the cost of lower reproducibility in crystal quality. It is worth noting that in some situations the seeded protocol, due to its higher complexity, is not experimentally possible to carry out. In such cases, the unseeded protocol is the only one available.

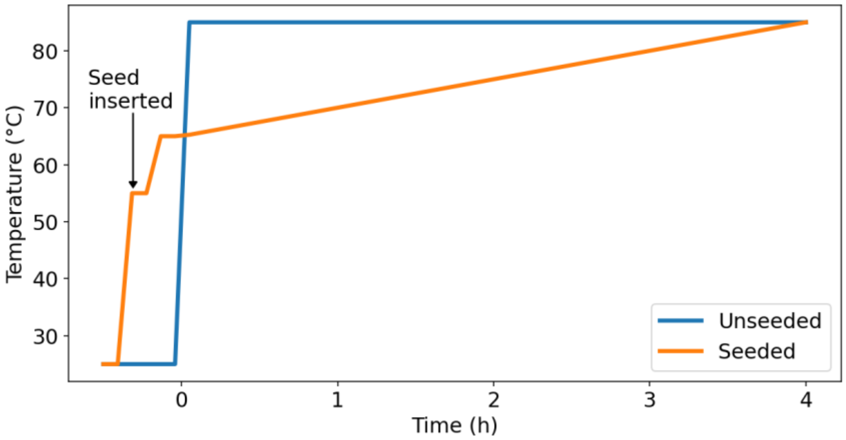

Figure 2.3 Temperature profiles for unseeded (blue curve) and seeded (orange curve) procedures. The arrow indicates the point in time when the seed is placed inside the solution.

Figure 2.4a shows an optical microscope image of a typical single crystal grown at DIFA. Inside the crystal, it is possible to clearly distinguish the seed from which the growth started. Typical $MAPbBr_3$ crystals have dimensions from 4x4 up to 8x8 mm^2 in the plane perpendicular to the growth direction and 1-2 mm in the growth direction.

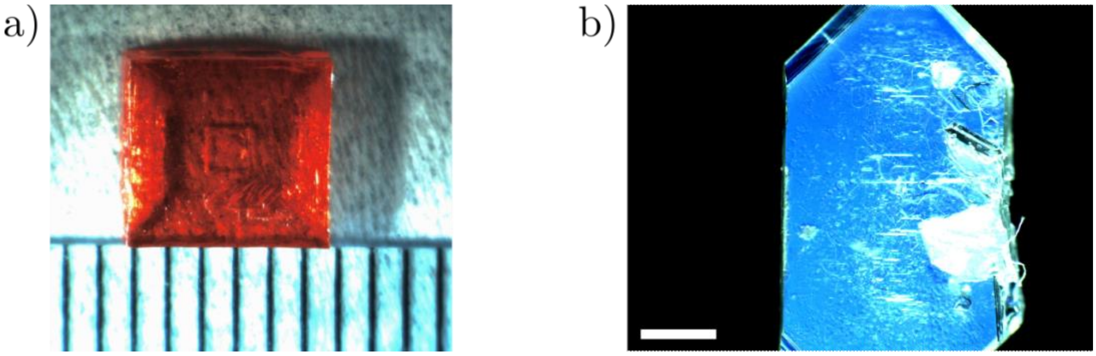

Figure 2.4 a) Optical microscope image of a $MAPbBr_3$ single crystal grown at DIFA using the seeded protocol. In the middle of the crystal, it is possible to observe the original seed. The spacing between the black ticks at the bottom is 1 mm. **b)** Dark field optical microscope image of a PEA_2PbBr_4 single crystal grown at DIFA. The white scalebar length is 0.5 mm.

2.1.2 PEA_2PbBr_4 single crystal synthesis

The growth of PEA_2PbBr_4 single crystal is performed from a solution consisting of phenethylammonium bromide (PEABr) and $PbBr_2$ dissolved in DMF with 1mol/L molarity, and in a 1:1 molar ratio. PEABr was purchased from Merck with purity >98%; for $PbBr_2$ and DMF the reader is referred to **Table 2.1**. The precursors are dissolved in DMF by stirring for 4 hours, and the solution is then filtered with a 0.22µm PTFE filter.

The crystal growth follows the slow evaporation method, as the ITC method is not applicable to this perovskite. The solution is placed under a chemical hood, in a glass vial covered with a cap. The cap contains small holes to allow the solution to evaporate and exit from the vial. The procedure consists of letting the solution evaporate, until the precursor concentration increases above saturation. At this point, spontaneous nucleation occurs, leading to the formation of crystal seeds that act as nucleation point for millimeter-scale crystals. The evaporation rate can be controlled by the number and size of the holes on the vial's cap. The more and the larger the holes, the faster the evaporation. The final crystal quality will increase if the evaporation process occurs with a slow rate. A typical duration for high-quality crystal growth is 3 weeks. The solution should be monitored on a daily basis to avoid letting the crystals grow too much and blend with each other. When crystals reach the desired size, they can be extracted from solution with tweezers. **Figure 2.4b** shows a dark field optical microscope image of a PEA_2PbBr_4 single crystal synthesized at DIFA. The typical crystal size for this material is from 1x1 to 5x5 mm^2 in the plane perpendicular to the growth direction, and hundreds of µm in the growth direction.

2.1.3 Atmosphere control in hybrid perovskite synthesis

As discussed in Chapter 1, hybrid lead halide perovskites are highly sensitive to environmental gases, especially water vapour and oxygen. In this thesis work, I carried out a systematic study on the impact of the growth atmosphere on the chemical and electrical properties of $MAPbBr_3$ single crystals. The purpose was to produce single crystals grown in a dry environment, with the lowest possible levels of oxygen and water, and in a standard laboratory environment with exposure to environmental oxygen and humidity. In the following, I will refer to the first category as *dry* samples and to the second one as *wet* samples. The synthesis of single crystals for this particular study was carried out at Institut Néel and CEA in Grenoble. In the following, I briefly explain the procedures for single crystal growth in the dry and wet conditions.

Figure 2.5 MBraun UNIlab Pro glovebox used for $MAPbBr_3$ single crystal synthesis in a controlled atmosphere.

Dry condition

Crystals of the dry condition were synthesized inside an argon-filled glovebox MBraun UNIlab Pro in LITEN (CEA), shown in **Figure 2.5**. The glovebox allows to measure in real time the water and oxygen concentrations in the working environment. For this work, the ranges of H_2O and O_2 concentration in the glovebox stayed always in the 1-5 ppm and 1-8 ppm range, respectively. The precursors and solvents used were the ones reported in **Table 2.1**, and they were opened and stored in the glovebox without ever being exposed to the external environment. This ensures that neither the precursors nor the atmosphere of growth contained any relevant amount of oxygen or water.

Wet condition

Crystals of the wet condition were synthesized under a chemical hood in the air. The relative humidity of the room was monitored by a humidity sensor and stayed in the range of 30-50% for the whole duration of the growth period. This corresponds to about 9,500-16,000 ppm H_2O concentration at a temperature of about 20 °C, i.e. about four orders of magnitude higher than in the dry condition. The oxygen concentration in the air is estimated to be about 210,000 ppm in standard environmental condition, i.e. five orders of magnitude higher than in the dry condition. The same precursors and solvents as for the dry condition were used. These were opened and stored in the air, and therefore exposed to environmental gases. It is important to note that perovskite precursors are highly hygroscopic, therefore they can easily incorporate water in such conditions. $PbBr_2$ by Alfa Aesar is sold in small glass flasks of 5 grams to protect it from air exposure before use. For crystal growth in this condition, the flasks were opened and $PbBr_2$ was exposed to air for around 24 hours before starting the growth procedure.

It is important to note that, for this study, all samples were grown by the unseeded protocol. The reason is that the setup for controlled seed-assisted growth was not available inside the glovebox.

2.1.4 Post-synthesis procedures

When single crystals are extracted from the growth solution, part of the solution remains attached to the crystal surface. Single crystals can then be dried either by using clean paper or by blowing dry nitrogen gas on them. Both methods cause fast solvent removal, which in turn, leads to the precipitation on the single crystal surface of additional microcrystals upon drying solution. Surface quality is key for many experimental techniques. Indeed, in optical measurements, high surface roughness could cause unwanted effects such as light diffusion, while in electrical measurements a highly defective crystal/electrode interface might severely affect the band structure in the vicinity of the electrical contact. Therefore, it is important to remove such imperfections to obtain smooth and clean crystal facets. In this thesis work, two methods were applied to smooth out the surface after synthesis: chemical etching and polishing. The chemical etching was performed on the crystals grown in DIFA, while polishing to those grown in Institut Néel/CEA.

Chemical etching

This procedure consists of partially dissolving the crystal surface using a solvent for the perovskite crystal, in this case DMF. It is based on the fact that irregularities and asperities tend to dissolve quicker than other parts of a surface. Therefore, with mild exposure to the solvent, it is possible to dissolve the microcrystals on the surface while leaving intact the main facets of the crystal. We found direct exposure to pure DMF even for a few seconds is too aggressive on the crystal surface. Therefore, we opted for dilutions of DMF in chlorobenzene (CB), an anti-solvent for the perovskite. After the growth, the crystals are pulled out of the solution, and quickly dried with a tissue wipe. Then, they are immediately dipped in six vials with decreasing DMF concentration for around 5-10 seconds. **Table 2.2** reports the DMF:CB ratios of the six solutions used for this process, with decreasing DMF concentration from step 1 to step 6. We note that the last two solutions contain only CB because their purpose is just to wash the crystal from any residual impurity without dissolving it. Because of this, the crystal can be kept in solution 5 and 6 for as long as needed.

	Step 1	Step 2	Step 3	Step 4	Step 5	Step 6
DMF:CB ratio	1:4	1:4	1:9	1:40	Only CB	Only CB

Table 2.2 DMF to CB ratio of the 6 solutions used for the chemical etching post-growth procedure. The crystal is kept for 5-10 seconds in each solution before moving to the next.

This method has the advantage of not putting the surface of the crystal in contact with any other substance that may chemically react with it (as in the case of polishing). On the other hand, it sometimes fails at fully removing the microcrystals at the surface, depending on their size.

Polishing

While etching is a chemical method, the polishing method is a physical one, where the sample surface is shaped by means of mechanical forces. Polishing is a standard procedure in the manufacturing process of classical semiconductors such as silicon.

The polishing protocol used for samples in this work runs as follows. The single crystal is fixed with silicone glue (Elkem Silicones CAF 4) on a flat glass surface, which is then glued to an aluminium piston (**Figure 2.6**). A concentric metallic handle encapsulates the piston allowing the user to move it and keep the piston weight on the crystal constant. If the crystal was grown with the seeded protocol, firstly the seed side is polished. The glue should only be in contact with one of the faces, while the lateral faces should remain untouched.

Figure 2.6 Picture of a $MAPbBr_3$ single crystal glued to the support for polishing, at CEA, Grenoble. Courtesy of Javier Mayén Guillén.

The exposed crystal face is polished by rubbing for 30 to 60 seconds against five different polishing disks of decreasing roughness. Solvents are also used to slightly dissolve the surface during the rubbing process. **Table 2.3** reports the disks and solvents or pastes used in the various polishing steps. All disks and pastes were purchased from PRESI[131]. In the first three steps, SiC disks are used (P400, P2400 and P4000) and isopropyl alcohol (IPA), a mild perovskite solvent, is sprayed on the disks. In these steps, both chemical and mechanical polishing take place. P400

SiC disk was only used for very uneven surfaces (seed side mainly). In the last steps (RAM and NT), diamond pastes containing diamond microcrystals with average size of 1µm or ¼ µm are used to obtain an optical-grade surface. At a later stage of the thesis work, the polishing procedure was simplified and the first three steps were replaced by a single step with P1200 SiC disk and IPA solvent. The results in optoelectronic performance with this procedure were unchanged with respect to the previous one. The crystal is then carefully removed from the support. The process is repeated for the other side (non-seeded side). After polishing both sides, the crystal is put in a toluene bath overnight to wash away any impurity from the process, then cleaned one last time with toluene.

Step	Polishing disk	Solvent/paste
1	P400	IPA
2	P2400	IPA
3	P4000	IPA
4	RAM	1 µm diamond paste
5	NT	¼ µm diamond paste

Table 2.3 Polishing disks and solvents/pastes used in the various steps for $MAPbBr_3$ single crystal polishing. All disks and pastes were purchased from PRESI.

The advantage compared to the etching method is that, in addition to removing microcrystals at the surface, polishing allows obtaining optical-grade surfaces, with roughness below 100 nm. Polishing also allows shaping the crystal faces: if two opposite faces of the crystal did not grow parallelly, it allows to make them parallel.

2.1.5 Electrical contacts deposition

Thermal evaporation

Electrical contacts on $MAPbBr_3$ and PEA_2PbBr_4 single crystals were deposited both at DIFA and Insitut Neél/CEA by thermal evaporation, a physical vapour deposition technique. Thermal evaporation is carried out inside an *evaporator*, a system consisting of a heater stage in a vacuum chamber, where the sample and the metal to be deposited are placed, vacuum pumps and various sensors and controllers that allow to monitor all the relevant physical parameters during the process. A schematic representation of the evaporation setup is shown in **Figure 2.7a**. The source of the metallic material to be evaporated is typically a tungsten rod plated with the metal of choice, or a tungsten basket containing a certain amount of the metal. The source is mounted between two metallic contacts connected to a current source, that allows to heat up the rod by Joule effect. The sample is mounted upside down on a sample holder directly above the source. Vacuum is then pumped into the chamber by a combined system of rotary and turbomolecular pumps. The pressure is monitored by Pirani and Penning gauges. The evaporation process can start when the pressure is in the range of 2-4 10^{-6} mbar. The source is heated until the melting point of the metal. At this point the metal starts to evaporate, its atoms are emitted from the rod in every direction and deposit in the whole chamber. The high vacuum in the chamber ensures that the atoms follow a straight-line path. A quartz microbalance inside the chamber allows monitoring the evaporation rate and the total deposited thickness. The sample is initially covered from the flux of metallic atoms by a shutter, which is opened when the microbalance measures a constant evaporation rate.

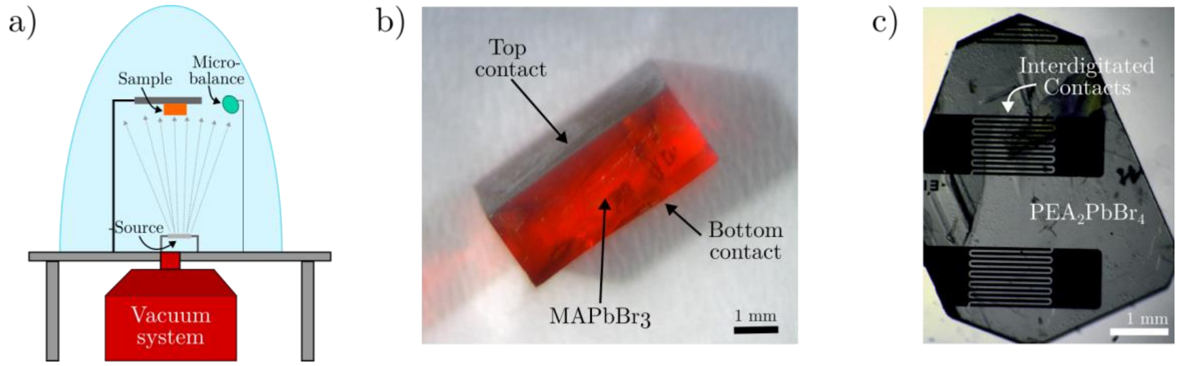

Figure 2.7 a) Schematic of the evaporation setup. **b)** Optical microscope picture of a $MAPbBr_3$ single crystal in side-view after a Cr evaporation. **c)** Optical microscope picture of a PEA_2PbBr_4 single crystal with interdigitated gold electrodes.

Electrical contacts on $MAPbBr_3$

The metal of choice for contacts on $MAPbBr_3$ was chromium (Cr). This material oxidizes during the evaporation process and forms chromium oxide CrO_x. Such oxide layer was shown to form a chemically stable contact with $MAPbBr_3$ and also to provide good ohmic behaviour[132]. The source of choice for this work was a Cr plated tungsten rod of 2 inches length (by Kurt J. Lesker Company). Cr contacts are deposited on two opposite sides of $MAPbBr_3$ single crystals by performing two subsequent evaporations. To avoid the metal layer to deposit also on the sides of the crystal, physical masks are placed on top of the crystal before mounting in the evaporator. The physical masks consist of either Kapton tape covering the sides of the crystal or metallic plates with holes of the right diameter covering the exposed surface. Since the devices are used for opto-electronic characterization, one of the two contacts needs to be semi-transparent to allow light to penetrate through the contact and reach the crystal. In the following, the semi-transparent contact will be referred to as the *top* contact, while the other as the *bottom* contact. The top contact is typically 20-30 nm thick, while the bottom contact is 70-100 nm. **Figure 2.7b** shows an optical microscope image of a $MAPbBr_3$ single crystal in side-view where the Cr top electrode is visible.

Electrical contacts on PEA_2PbBr_4

The metal of choice for contacts on PEA_2PbBr_4 single crystals was gold (Au), which we found shows good ohmic behaviour on this material. Due to the large resistivity and low charge carrier mobility of 2D perovskites in the direction perpendicular to the organic spacers,[133] we found that the top-bottom configuration was not suitable for efficient charge collection in these samples. Therefore, we opted for a planar configuration with interdigitated electrodes. The metallic source for evaporation are Au filaments placed in a tungsten basket. During the evaporation the sample is covered by a physical mask with the desired interdigitated geometry. In this work, we used masks produced by Ossila with 1x1.3 cm^2 dimensions and channel width of 40µm. **Figure 2.7c** shows an optical microscope image of a PEA_2PbBr_4 single crystal after Au contact evaporation.

2.1.6 Sample mounting for cryogenic measurements

When performing cryogenic measurements, the sample is in thermal contact with a cold finger that is cooled and heated according to the setpoint temperature. The sample temperature is measured by a sensor placed on the cold finger, close to the sample. Therefore, the thermal contact between the cold finger and the sample needs to be as good as possible to minimize temperature mismatch between the two, which leads to a systematic error in the sample temperature reading.

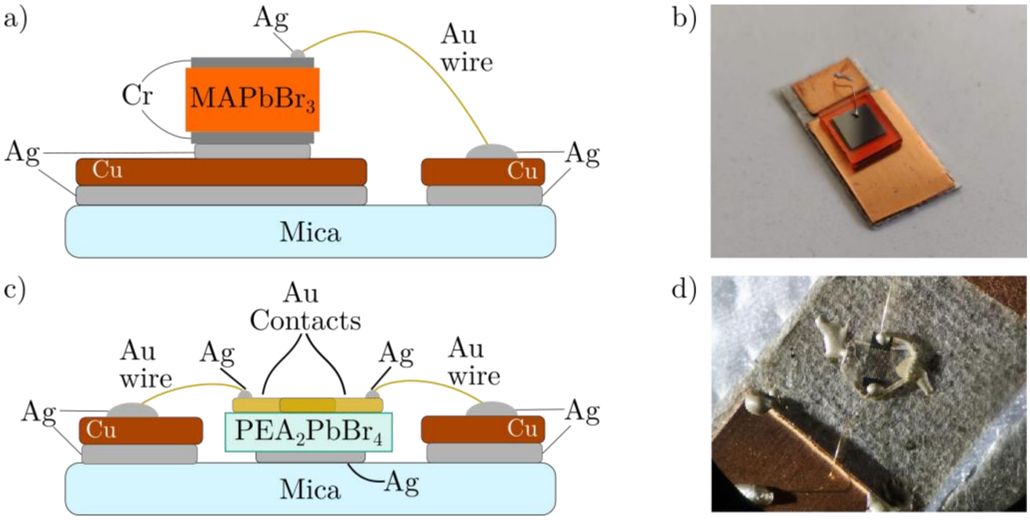

Figure 2.8 Schematic representations (**a** and **c**), and pictures (**b** and **d**) of the device structure for cryogenic measurements of $MAPbBr_3$ and PEA2PbBr4 single crystals, respectively.

$MAPbBr_3$ crystals

Figure 2.8a-b shows a schematic representation and a picture of the device structure for cryogenic measurements on $MAPbBr_3$ crystals. The chosen substrate is a PELCO mica sheet grade V5 of thickness 250 µm, cut to an area of approximately 2×1 cm^2. Mica is an electrical insulator, an essential property to avoid short circuits in the device, but at the same time it is a decent thermal conductor, with thermal conductivity of around 0.75 $Wm^{-1}K^{-1}$. Combined with the low thickness of the substrate, this allows to minimize the thermal impedance of the device. Two copper sheets, one bigger than the other, are cut and glued on the mica substrate with a bi-component epoxy silver paste (Chemtronics CW2400). A metallic epoxy is chosen over other kinds of glue to maximize thermal conductivity. The bottom contact of the crystal is glued to the bigger Cu pad with the same silver paste. In this step, special attention is paid to ensure that the silver paste contacts only the Cr film and not the perovskite material. Finally, a copper or gold wire is glued by silver paste to the top Cr contact on one side and to the smaller Cu pad on the other side. In this geometry, the electrical signal from the top and bottom contacts can be extracted from the two copper pads, using metallic probes.

PEA_2PbBr_4 crystals

Figure 2.8c-d shows a schematic representation and a picture of the device structure for cryogenic measurements on PEA_2PbBr_4 crystals. The substrate and epoxy silver paste of choice are the same as for $MAPbBr_3$ samples. The bottom of the crystal is fixed to the substrate by epoxy silver paste, to ensure good thermal contact and mechanical stability during measurements. The two Au pads of the interdigitated contacts are connected by gold wires to copper pads, fixed to the substrate by silver paste.

2.2 Surface photovoltage spectroscopy

Surface photovoltage spectroscopy (SPS) is a powerful optoelectronic technique that can give insight on surface defects and excitonic states in semiconducting samples. It consists of measuring the surface photovoltage (SPV) between the sample surface and a reference electrode as a function of the incident photon wavelength. SPS measurements in this work were carried out at DIFA. In the following, I describe the experimental setup and the measurement protocol followed in this thesis work.

2.2.1 Experimental setup

The experimental apparatus for SPS measurements is schematized in **Figure 2.9**.[134] A 150W Xenon Arc Lamp (Thorlabs SLS 401) is used as a broadband light source and aligned in front of the entrance slit of a SPEX 500M monochromator. The monochromator contains a grating (600 grooves/mm) that allows to separate the impinging white light in all its wavelength components. The beam then reaches the output slit of the monochromator, which allows only a small monochromatic portion of the beam to exit. The grating is mounted on a motorized rotating axis, which allows to turn it, modifying the output wavelength λ. The output beam of a monochromator always shows spectral broadening, i.e. it contains other wavelengths that are spread in an interval $\Delta\lambda$ around λ. The main contribution to the spectral broadening comes from the width input and output slits and for this specific monochromator it is given by

$$\Delta\lambda = 1.6\,\frac{\mathrm{nm}}{\mathrm{mm}}\cdot w \qquad 2.1$$

where w is the width of the two slits, which should be set to the same value. In this thesis work the width w was always set to 1mm, leading to 1.6 nm spectral broadening.

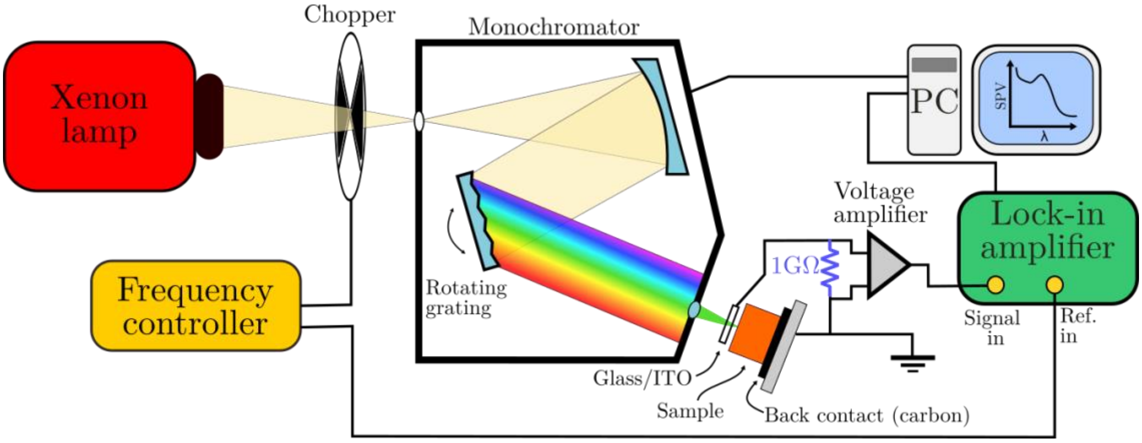

Figure 2.9 Schematic representation of the experimental setup for Surface Photovoltage Spectroscopy measurements.

The output beam is focussed on the sample by a lens with 20 mm focal length. The beam shape impinging on the sample is a rectangle of approximately 10 mm by 0.5 mm, where the latter can vary depending on slit aperture and sample position with respect to the lens focal distance. The sample is attached to a metallic holder by conductive carbon tape, that also acts as back contact and is set to ground. The surface photovoltage signal is collected in the Metal-Insulator-Semiconductor (MIS) configuration. A transparent indium tin oxide (ITO) thin film deposited on glass acts as a metal electrode and it is placed at a distance of around 0.5 mm from the sample surface. Air acts as an insulating layer between ITO and the semiconducting sample, forming a capacitor structure.

The ITO layer and the ground electrode are connected through a 1GΩ resistor. When light hits the sample, it induces a change in surface work function, which in turn causes an electron flow between ITO and ground, through the resistor. The electrical potential drop across the resistor is amplified by a Femto DLPVA voltage amplifier and then sent as input to a Stanford Research Systems SR830 lock-in amplifier. The Xenon lamp light is modulated in time by an optical chopper at a frequency fixed by a controller. A signal with the same frequency is sent from the controller to the reference input of the lock-in amplifier.

The system is controlled by a custom LabView software that allows to monitor the SPV signal measured by the lock-in amplifier as a function of the wavelength impinging on the sample. The software allows to set the initial and final wavelength, a wavelength step, and the time delay between each step. The SPV spectrum is shown live on the monitor during the acquisition.

In this work, the settings used for the data acquisition are the following:

- Slit aperture: 1 mm
- Chopper frequency: 20 Hz
- Delay time between points: 5 s (with lock-in time constant of 1 s)

All measurements were performed in air and at room temperature.

2.2.2 Measurement protocol and data analysis

The optical power output of the Xenon lamp is not constant as a function of wavelength. This can introduce features in the SPV spectrum which are not relative to the sample properties. To overcome this problem, the acquired signal spectrum $S(\lambda)$ has to be normalized by the photon flux spectrum $\Phi(\lambda)$ of the lamp (in units of photons/s). A sensor is used to measure the incident power spectrum $P(\lambda)$ (in units of W), and the flux is calculated as $\Phi(\lambda) = P(\lambda)/E$, where $E = hc/\lambda$ is the photon energy. The SPV signal is then calculated as:

$$SPV(\lambda) = \frac{S\,(\lambda)}{\mathrm{P}(\lambda)/(\mathrm{hc}/\lambda)} = \frac{S(\lambda)}{\Phi(\lambda)} \qquad 2.2$$

The use of the flux instead of the power for normalization comes from the assumption that what determines the SPV is the number of photons on the sample, not their energy.

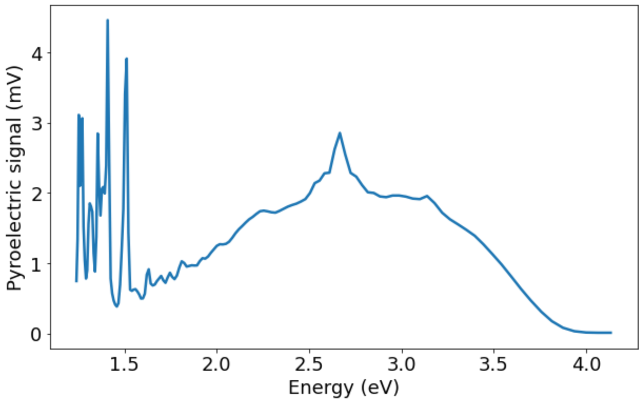

Figure 2.10 Spectrum of the Xenon lamp of the SPS setup acquired by a pyroelectric sensor.

After each session of SPS measurements, the lamp spectrum is acquired via a Scitec Instruments LT Q2 pyroelectric sensor placed at the output of the monochromator and connected to the lock-in amplifier. Pyroelectric sensors show a constant responsivity as a function of wavelength, so the spectrum measured with this setup reflects the real lamp spectrum. **Figure 2.10** shows a typical example of a Xenon lamp spectrum acquired by the pyroelectric sensor. Alternatively, a silicon photodiode can be used, but in this case the sensor responsivity is wavelength-dependent and the acquired signal has to be divided by the responsivity curve provided by the photodiode manufacturer. It is relevant to note that the lamp spectrum may change over time, therefore it is good practice to measure the lamp spectrum before or after each SPS session.

2.3 Photoluminescence spectroscopy

Photoluminescence (PL) spectroscopy is a widely used optical technique that allows to determine the optical band gap of a semiconductor, and can also give insight surface quality and defective states in the material. In this work, PL measurements were carried out at DIFA.

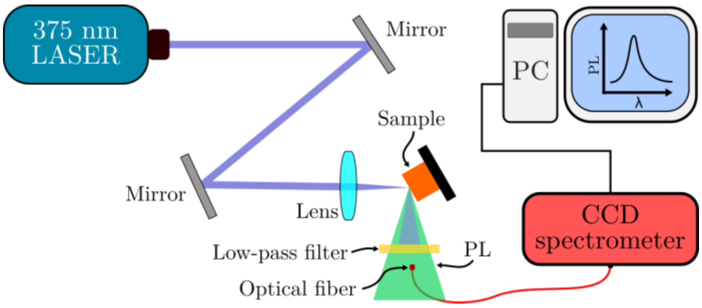

Figure 2.11 Schematic representation of the experimental setup for photoluminescence spectroscopy.

The experimental apparatus for PL spectroscopy is schematised in **Figure 2.11**. A 375 nm PicoQuant diode laser set at 100 μW power and pulsed at 100 MHz is used as optical excitation. Two mirrors deflect the laser beam on a lens that focuses the beam on the sample surface, placed at a 45° angle with respect to the incident beam. The PL is emitted by the sample together with the reflected laser light. A 400 nm long-pass filter is used to reject the reflected laser beam. After the filter, an optical fibre collects the PL signal and sends it to a CCD spectrometer (Thorlabs CCS200/M). A Thorlabs software allows to acquire, plot, and save the data from the spectrometer. To improve the signal-to-noise ratio, several consecutive spectra are averaged together during an integration time of typically 1-2 seconds. All measurements are performed in air and at room temperature.

2.4 X-ray irradiation

As discussed in Chapter 1, one of the promising applications for lead halide perovskites is the detection of ionizing radiation. For this reason, in this thesis work several measurements were performed before and after X-ray irradiation or as a function of X-ray dose deposited on the samples. X-ray irradiation in this work was carried out at DIFA. In this section, I describe the physical quantities used to describe X-ray doses, the setup for X-ray irradiation, and the experimental procedure for radiation hardness measurements.

2.4.1 Dosimetric quantities

Absorbed dose

In the international system of units (SI), the unit of measure for radiation dose is the gray (Gy). One gray corresponds to one joule of ionizing radiation energy absorbed by one kg of matter.

$$1\ \mathrm{Gy} = \frac{1\ \mathrm{J}}{1\ \mathrm{kg}} \qquad 2.3$$

Alternatively, in the cgs system, the unit of measure of radiation dose is the rad, where 1 rad = 0.01 Gy.

KERMA

KERMA is an acronym for kinetic energy released per unit mass. This quantity is applicable to non-charged ionising radiation particles such as photons and neutrons. It is defined as the average kinetic energy ($\overline{E_k}$) transferred by such particles to charged particles in the medium (e.g. electrons) per unit mass[135].

$$K = \frac{\mathrm{d}\overline{E_k}}{\mathrm{d}m} \qquad 2.4$$

The unit of measure is the gray, defined as in Equation 2.4, although KERMA and absorbed dose do not coincide in general. Calibration of radiation sensors is commonly performed using *air KERMA*, which corresponds to KERMA where dry air is used as a medium. The unit of air KERMA is the *gray air KERMA* ($\mathrm{Gy_{air}}$). In the following, all radiation doses will be expressed in $\mathrm{Gy_{air}}$, but they will simply be referred to as Gy for simplicity.

2.4.2 Experimental setup

In this work, a tungsten (W) target X-ray tube is used for X-ray irradiation of the samples (Hamamatsu Microfocus L12161-07). In this device, a cathode, heated by a current I_c flowing through it, thermally emits electrons. These are accelerated towards a target anode made of W metal by a voltage V_a. As a result of the interaction with the high energy electrons, X-rays are emitted by W atoms in the target. X-rays exit the tube through a beryllium window forming a diverging X-ray beam.

The X-ray tube was set at $V_a = 150$ kV and $I_c = 500$ μA. The sample to be irradiated was placed at 9 cm from the tube. By a previous calibration with a commercial detector, such settings result in a dose rate of 72 mGy/s. **Figure 2.12a** shows a schematic representation of the setup, and **Figure 2.12b** shows a simulation of the emission spectrum of the W-target X-ray tube.

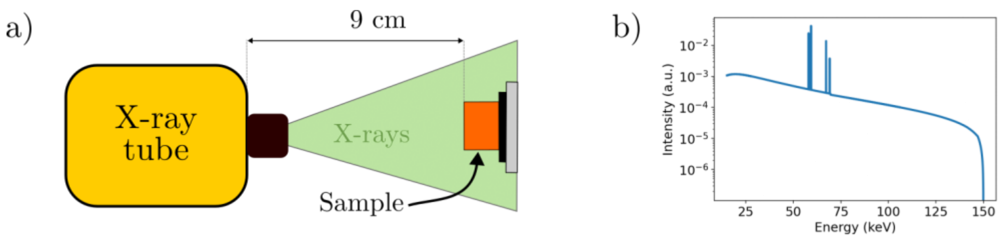

Figure 2.12 a) Schematic representation of the experimental setup for X-ray irradiation. **b)** Simulation of the W-target X-ray tube spectrum operated at an accelerating voltage of 150 keV.

2.4.3 Radiation hardness measurements

Radiation hardness measurements are typically performed on materials, devices and equipment that will be exposed to ionizing radiation during their operation lifetime. These tests allow to determine how much ionizing radiation dose the sample can withstand before changing its properties.

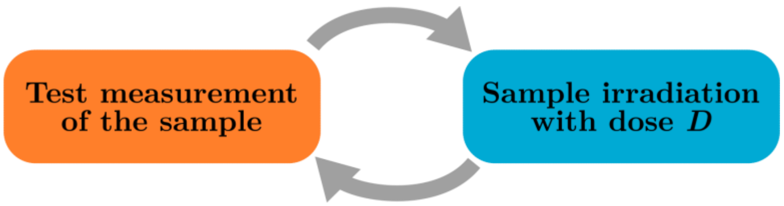

Figure 2.13 Schematic of a radiation hardness measurement. The sample is continuously irradiated and then tested. The process is repeated until the target total dose is reached.

As schematized in **Figure 2.13**, a radiation hardness measurement. First, the sample is measured in a pristine condition. Then, an ionising radiation dose D is deposited on the sample and the test measurement is repeated after irradiation. The process is repeated N times, until the target total dose $D_{tot} = N \cdot D$ is reached.

2.5 Kelvin probe force microscopy

Kelvin probe force microscopy (KPFM) is a powerful kind of atomic force microscopy (AFM) that allows to acquire nanometre-resolution maps of the work function (WF) of a semiconducting sample. In addition, it also allows to parallelly acquire morphology maps of the sample's surface. KPFM measurements in this work were carried out at DIFA. In the following, I describe the experimental setup for KPFM measurements, as well as the procedure followed to obtain reliable absolute work function values.

2.5.1 Experimental setup

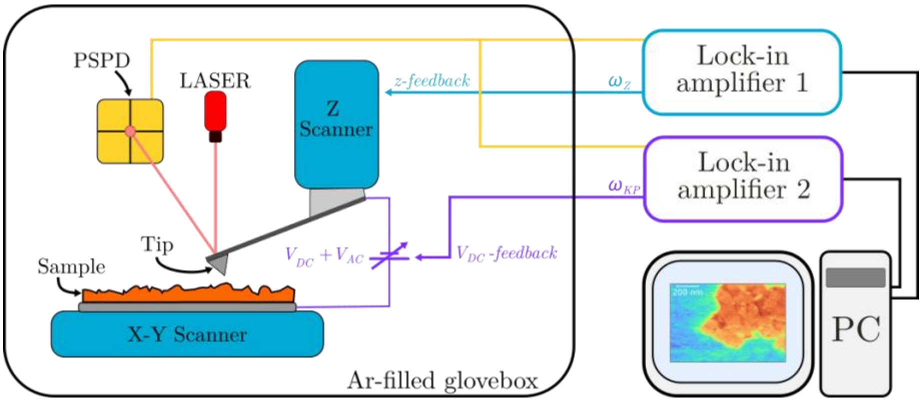

Figure 2.14 Schematic representation of the experimental setup for KPFM measurements in argon atmosphere.

Figure 2.14 shows a schematic representation of the KPFM setup. The sample under study is fixed on a X-Y scanner that moves in the horizontal plane with nanometre precision, thanks to piezoelectric actuators. A very sharp tip with radius of around 10 nm attached to a cantilever is connected to a piezoelectric Z scanner that allows to adjust its vertical position with sub-nanometre resolution. The tip is placed at a distance of a few nanometres from the sample's surface and its vertical position is modulated by the Z scanner at a frequency ω_Z. Visible laser light aligned with the tip position is reflected by the cantilever onto a position-sensitive photodetector (PSPD), that allows to monitor the tip height. The PSPD signal is sent to a lock-in amplifier, locked on the reference frequency ω_Z. As the tip moves on the sample's surface, its oscillation amplitude measured by the lock-in amplifier changes with the morphology, due to changes in the sample-tip interactions. A feedback system offsets the Z position of the tip in order to keep constant the tip oscillation amplitude, and thus the sample-tip distance. The offset from the feedback system is recorded as a function of the X and Y positions, yielding a map of the sample's morphology.

At the same time, a voltage source applies between the sample and the tip a potential difference, which is sum of a DC offset (V_{DC}) and an AC modulation (V_{AC}), at a frequency $\omega_{KP} \neq \omega_Z$. Such modulation results in an additional tip oscillation recorded by the PSPD, relative to tip-sample electrostatic interactions. The PSPD Signal is also sent to a second lock-in amplifier, locked on ω_{KP}. In a similar fashion to the case of morphology mapping, a feedback system offsets V_{DC} in order to maintain constant the oscillation amplitude measured by the second lock-in amplifier. Recording such offset as a function of X and Y, yields a map of the sample's surface potential. These values can be converted to work function values upon multiplication by the electron charge e.

The atomic force microscope model in this setup is a Park System NX10. The tip is a NSC36/CrAu-B tip (Mikromasch, k=2 N/m). The whole setup is enclosed in an argon-filled glovebox that allows to maintain a dry atmosphere during measurements to avoid sample degradation. Samples were fabricated in glovebox at KAUST (Saudi Arabia), shipped to DIFA in sealed plastic bags, which were opened inside the glovebox.

2.5.2 Tip work function calibration

To accurately measure the sample's work function, it is essential to know the tip work function. Indeed, the measured KPFM potential corresponds to the difference between the sample and the tip work functions. The sample's work function is then calculated as

$$WF_{sample} = WF_{measured} + WF_{tip}. \qquad 2.5$$

To measure the tip work function, I performed a KPFM map on an Indium Tin Oxide (ITO) thin film sample with known work function of $WF_{ITO} = -5.0 \pm 0.1$ eV. **Figure 2.15a** shows the measured KPFM map. In **Figure 2.15b,** all pixel values of the map are plotted in a histogram representing the distribution of KPFM potential. The distribution fits a Gaussian profile, as shown by the red solid curve. The measured KPFM potential was considered as the mean of the Gaussian distribution, $V_{meas} = -0.11$ V. Finally, the tip work function was calculated as

$$WF_{tip} = WF_{ITO} - eV_{meas} = -4.9 \pm 0.1 \text{ eV} \qquad 2.6$$

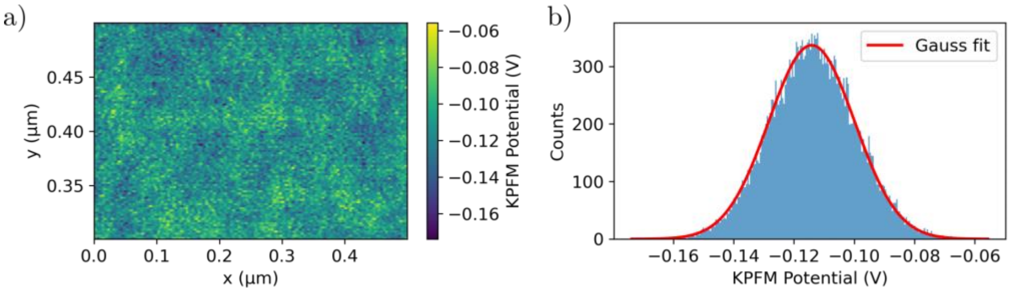

Figure 2.15 a) KPFM map of the reference ITO sample. **b)** Distribution of KPFM potential values extracted from the map. The red solid line is a gaussian fit of the data.

2.6 Photoinduced current transient spectroscopy (PICTS)

Photoinduced current transient spectroscopy (PICTS) is an experimental technique used since the 80's to characterise electronic defects in high-resistivity semiconductors [85,86,102]. It consists of measuring photocurrent transients as a function of temperature. The data are then analysed to extract relevant parameters such as activation energy and capture cross-section of the defects. One of the key achievements of this thesis work was the implementation of the PICTS experimental setup, as well as the development of an original code for fast and reliable analysis of the data. This work was carried out at DIFA. In the following, I describe the experimental setup, the theory behind the data analysis, and how the data analysis has been implemented.

2.6.1 Experimental setup

The experimental setup for PICTS measurements is shown in **Figure 2.16**. The description is divided into subsections regarding the different aspects of the setup.

Temperature control

The device, as described in Section 2.1.6, is mounted inside a Janis VPF-800 cryostat. A rotary vacuum pump connected to the cryostat allows to pump 10^{-3} mbar vacuum, which avoids condensation at cryogenic temperatures and ensures better thermal isolation from the outer environment. An inlet allows to pour liquid nitrogen (LN_2) in a Dewar hosted inside the cryostat. The LN_2 bath is put in thermal contact with a copper cold finger, where the sample is mounted. Between the LN_2 bath and the cold finger, inside a copper enclosure, is mounted a resistive heating element, electrically connected to two wires soldered to an output socket at the top of the cryostat. This is connected to a Lakeshore 331 temperature controller, that allows to heat up the heating element by Joule effect, flowing a current through it.

Temperature inside the cryostat is monitored by two temperature sensors. The first one is a thermocouple mounted close to the heating element, the second one is a silicon diode sensor (Lakeshore DT-670) mounted on the back of the cold finger, close to the sample mounting position. Both sensors are connected to the exterior by output sockets, which are connected to the temperature controller. The first sensor serves as a quick feedback that readily responds to temperature changes caused by the heating element. The second sensor, instead, provides reliable reading of the sample temperature. The temperature controller sets the cold finger temperature via a PID (Proportional Integral Derivative) feedback. This balances the cooling action of LN_2 with the heat produced by the controlled current flow through the heating element, allowing to reach the desired setpoint temperature. The Lakeshore 331 controller also allows to perform linear temperature ramps, with a configurable rate expressed in K/min. This feature is key, since all PICTS measurements are performed during temperature ramps. A custom LabView software, interfaced with the temperature controller, allows to remotely set all the relevant temperature parameters.

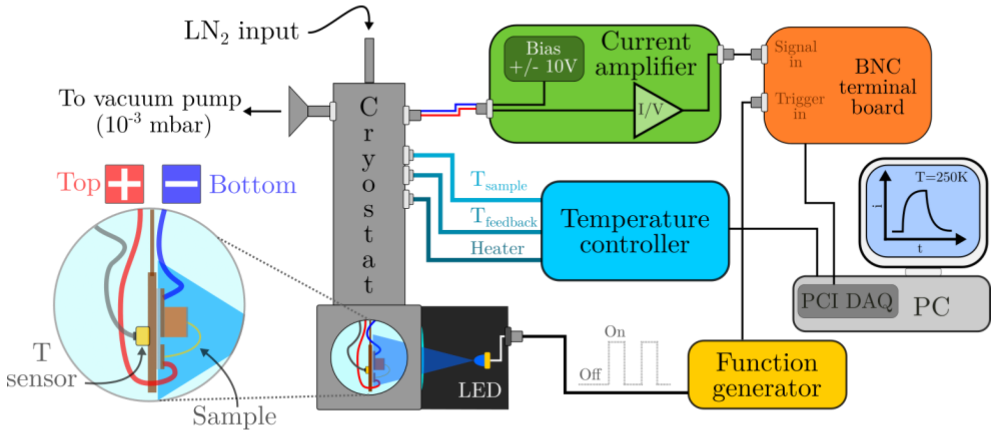

Figure 2.16 Schematic representation of the experimental setup for PICTS measurements.

Electrical signal acquisition

The sample is placed on the cold finger, which is covered by Apiezon® H or N grease to improve thermal contact. Two copper clamps are screwed on the two electrical contacts of the device. Two copper wires, soldered to the clamps, bring the electrical signal to an output BNC at the top of the cryostat. The top contact of the device is always connected to the core of the BNC, and the bottom contact to the shield. A picture of the cryostat cold finger is shown in

Figure 2.17, with labels indicating the different components. A BNC cable connects this output to a Femto DLPCA-200 transimpedance current amplifier. This device allows to bias the sample with a configurable voltage between -10 and 10 V, and to amplify the output current. The gain can be set by the user in the range $10^3 – 10^{11}$ V/A. The maximum output voltage is 10V, and a LED indicator labelled as *overload* turns on when this value is exceeded. A 10 Hz low-pass filter can also be enabled. In this thesis work, this filter was used on slow transients with 0.2 Hz modulation, in order to reduce the noise. The output signal of the amplifier is sent to a BNC 2120 terminal board by National Instruments. This is connected to a National Instruments PCI-6013 digital acquisition board (DAQ) mounted inside a PC. The LabView software is interfaced with the DAQ and allows to set the data acquisition parameters, monitor the measurement, and save the data for later analysis. This software saves the data in a TDMS format, which can be easily read by LabView-based softwares, as well as by other programming languages.

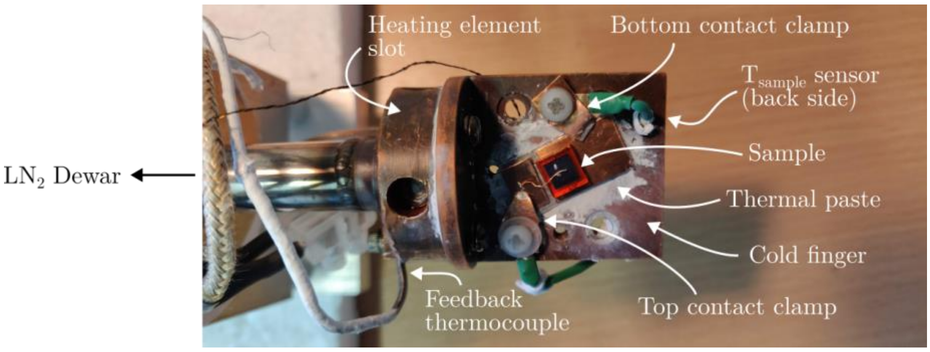

Figure 2.17 Picture of the cryostat cold finger with a mounted sample. Labels indicate the different components.

Optical stimulation

The sample in the cryostat is optically accessible via a glass window. A LED of suitable wavelength (typically above the energy gap of the sample) is placed in front of the window, inside a dark enclosure. A GW Instek MFG-2110 function generator provides a square-wave voltage signal to the LED, turning it on and off with configurable frequency and duty cycle. A square-wave reference signal with the same frequency is sent to the DAQ as trigger. To linearise the optical response of the LED with respect to the applied voltage, a resistor is connected in series to the LED. In this work, two LED models were used: a 475 nm blue LED (OSRAM Oslon LBCRBP) for $MAPbBr_3$ samples, and a 365 nm UV LED (Würth Elektronik WL-SUMW SMT) for PEA_2PbBr_4 samples. The light intensity of the LEDs was calibrated using a commercial silicon photodiode (Hamamatsu S2281-01), and was 3 mW/cm^2 on $MAPbBr_3$, and 1.4 mW/cm^2 on PEA_2PbBr_4.

Measurement protocol

A complete description of the measurement protocol can be found in Appendix A. It illustrates a typical procedure for PICTS measurements, using the experimental setup at the Department of Physics and Astronomy of Bologna.

2.6.2 Data analysis

The double-gate rate window method

Defect spectroscopy techniques like DLTS and PICTS can be analysed using two possible approaches. The first one consists of fitting the decay transients at each temperature to a multi-exponential curve of the form $\sum_{i=1}^{N} A_i e^{-t/\tau_i}$, where N is the number of processes that have to be fitted, and A_i and τ_i are the amplitude and characteristic time of each process. This method has been used for analysis of DLTS signals in inorganic semiconductors [136,137] and, recently, in halide perovskites [61,109,138]. This system has the disadvantage of relying on the quality of exponential fits. These can be disturbed by several phenomena, such as non-exponential components, or signals with a number of components N that is too high to yield reliable fitting parameters. The second method is called *rate window* method, which is a numerical one, that does not rely on fitting. In this thesis work, the rate window method was chosen. It will be described in the following, based on the work of Balland et al.[86].

Let's assume an ideal photocurrent transient as shown in **Figure 2.18**. The current is initially in the dark state $i(\infty)$. At time A, light turns on. Between A and B, photogenerated carriers reach equilibrium with their corresponding band. Between B and C, trapping by defect states causes a slower transient behaviour until a stationary state is reached and the current stabilizes at $i(0)$. At time D, light is turned off. Current rapidly drops between D and E due to band-to-band recombination. Between E and F, thermal emission of carriers from defect states introduces a slow transient behaviour. The latter is the signal of interest for PICTS measurements. It is assumed that the E-F time range is long enough for traps to release all carriers, so that current at time t_∞ is the dark current $i(\infty)$.

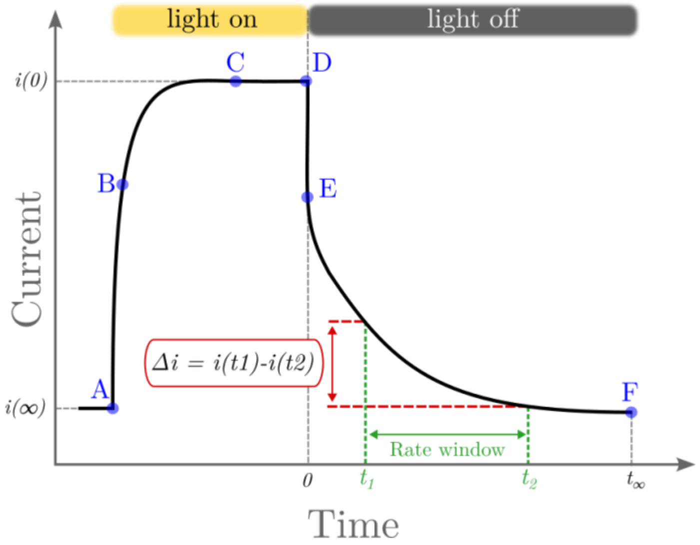

Figure 2.18 Schematic representation of the double-gate rate window method on an ideal photocurrent transient. Points A, B, C, D and E represent the key points in time where different phenomena take place, as described in the text.

As discussed in Chapter 1, the current decay related to de-trapping of electrons from a single trap state, is described by an exponential decay in the form

$$i(t) = i(\infty) + eAE\mu_n\tau_n n_t(0)\frac{1}{\tau_t}\exp\left(-\frac{t}{\tau_t}\right) \tag{2.7}$$

where the variable τ_t represents the characteristic time for trap emission from the energy level, which depends on temperature according to the Arrhenius equation

$$\frac{1}{\tau_t} = e_t = \sigma v_n N_c \exp\left(-\frac{E_a}{kT}\right) \tag{2.8}$$

where e_t is the emission rate. The relevant trap parameters that can be extracted by PICTS are the activation energy of the defect E_a and its capture cross section σ. Expressing the temperature dependence of v_n and N_c allows to formulate the expression that is key for defect level characterization, as it defines the so-called *Arrhenius plot.*

$$\ln\left(\frac{T^2}{e_t}\right) = \gamma\sigma + \frac{E_a}{kT} \tag{2.9}$$

where γ contains universal constants and the effective mass of the semiconductor under study.

The simplest form of the rate window method is the double-gate method, schematized in **Figure 2.18**. It consists of choosing two time instants t_1 and t_2, called *gates*, that define a rate window of duration $t_2 - t_1$. The PICTS signal for such rate window is defined as the difference between current at time t_1 and time t_2, calculated as a function of temperature:

$$\Delta i(T) = i(t_1, T) - i(t_2, T) \tag{2.10}$$

By combining Equations 2.7 and 2.10, it can be found that the $\Delta i(T)$ shows a maximum at temperature T_m, which, through Equation 2.8, corresponds to a specific emission rate $e_t(T_m)$. The condition for the maximum can be found by maximizing the $\Delta i(T)$ function, which yields

$$e_t(t_2 - t_1) = \ln\left(\frac{e_t t_2 - 1}{e_t t_1 - 1}\right) \qquad 2.11$$

where e_t is calculated at temperature T_m. Equation 2.11 is key for relating theory (through e_t) and experiment (through t_1 and t_2). Indeed, once the rate window is chosen by setting t_1 and t_2, the corresponding emission rate is fixed by this equation. This is a transcendental equation and can be solved numerically to find e_t. Equation 2.11 is obtained assuming the initial filling $n_t(0)$ is constant over the whole temperature range, which can be achieved using high-intensity photoexcitation that saturates all traps. In the case of low-intensity excitation, the condition becomes $e_t = \ln\left(\frac{t_2}{t_1}\right)/(t_2 - t_1)$, which is the same as the one used for DLTS analyses.

To better understand this procedure, we present in Figure **2.19** an example on simulated current transients. Figure **2.19**a shows a series of transients that simulate the emission from a single trap state with $E_a = 0.5$ eV and $\sigma = 10^{-19}$ cm^2 in the temperature range 350-500 K, based on Equations 2.7 and 2.8. For better visualisation, all transients have been normalised between 0 and 1. As expected, based on Equation 2.8, the characteristic time of the current decays decreases with temperature, i.e. emission from the trap is faster at higher temperature. Figure **2.19**b shows selected transients at three different temperatures. In this example, the two gates are chosen as $t_1 = 0.1$ s and $t_2 = 0.2$ s, which are represented as vertical dashed the lines. The corresponding Δi values are represented as two-sided arrows. Figure **2.19**c shows the PICTS spectrum, i.e. the plot of Δi as a function of temperature. Coloured dots on the spectrum represent the Δi values obtained for the three selected transients of Figure **2.19**b. As expected from theory, the spectrum shows a maximum at a specific temperature. From the spectrum it is possible to extract the two values e_t and T_m. The former is calculated solving Equation 2.11 for $t_1 = 0.1$ s and $t_2 = 0.2$ s, the latter by locating the maximum of the spectrum. This yields $e_t = 14.4$ Hz and $T_m = 422.4$ K.

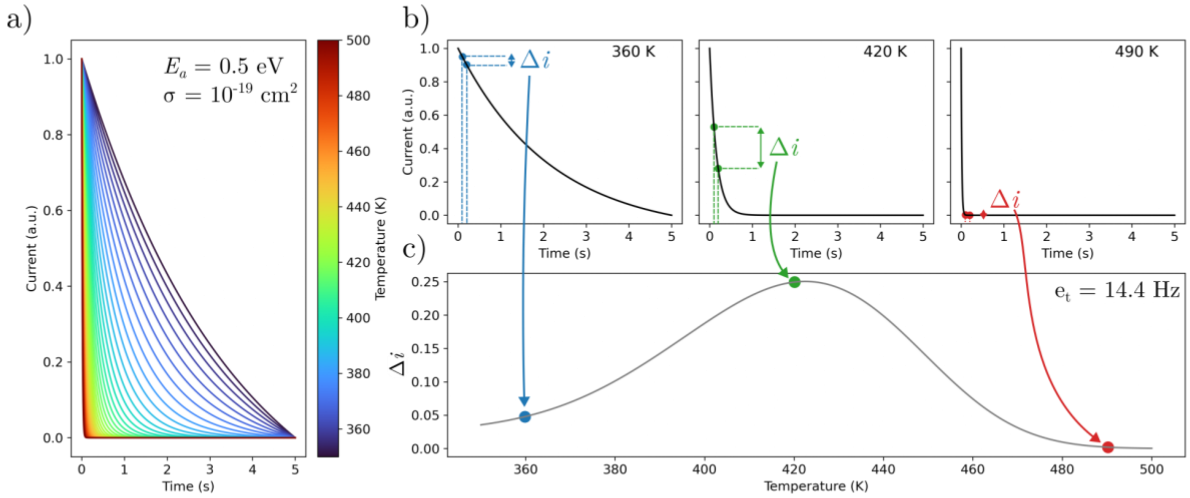

Figure 2.19 a) Simulated current transients for a single defect state with $E_a = 0.5$ eV and $\sigma = 10^{-19}$ cm^2 in there 350-500 K temperature range. **b)** Selected transients from (a) at three different temperatures. For all three, the same rate window is selected, with $t_1 = 0.1$ s and $t_2 = 0.2$ s. The corresponding Δi values are indicated by two-sided arrows. **c)** The PICTS spectrum consists of a plot of the Δi values as a function of temperature. Coloured dots indicate the specific Δi values calculated from the transients in (b). This spectrum is relative to the rate window $e_t = 14.4$ Hz, determined by the t_1 and t_2 values.

The method above allows to extract a single $e_t(T_m)$. However, based Equation 2.9, this is not enough to extract the two trap parameters E_a and σ, wich are unknown. By repeating the process with different rate windows, one can find a set of $e_t(T_m)$ values that reconstruct the Arrhenius plot. Finally, by a linear fit of $\ln\left(\frac{T^2}{e_t}\right)$ versus $1/T$, one can extract E_a and σ.

In the double-gate rate window procedure, it is common practice [84,86] to hold constant the ratio t_2/t_1, defined as

$$\beta = \frac{t_2}{t_1} \qquad 2.12$$

where typically $1.5 < \beta < 4$. This parameter is rarely chosen greater than 4, because this produces large rate windows that decrease sensitivity. Most commonly used values are $2 < \beta < 3$. To produce further rate windows, t_1 is shifted along the time axis by an arbitrary quantity. For each t_1 value, the corresponding t_2 is fixed by β, according to Equation 2.12.

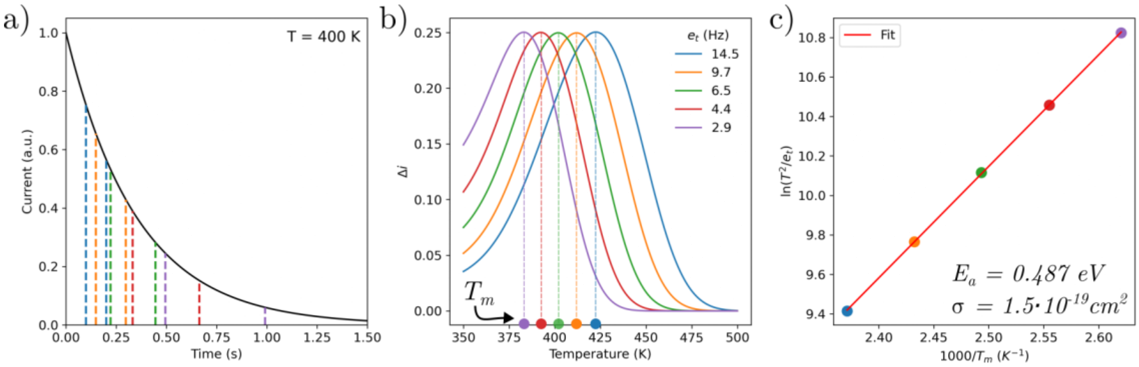

Figure 2.20 a) Current transient decay at $T = 400$ K of the same simulation as in **Figure 2.19**. Couples of vertical dashed lines of different colour represent the five rate windows chosen for this analysis. **b)** calculated PICTS spectra are represented with the same colours as their corresponding rate window in (a). Coloured dots on the x-axis represent the T_m values. **c)** Arrhenius plot produced from values of e_t and T_m extracted from (b). Each point has the same colour as its corresponding spectrum and rate window in (a) and (b). The red solid line represents a linear fit to the points.

Figure 2.20 shows an example of such procedure, based on the same data as **Figure 2.19**. **Figure 2.20a** shows the transient corresponding to $T = 400$ K, and five rate windows, each represented as a couple of vertical dashed lines of the same colour, indicating t_1 and t_2. In this case $\beta = 2$ was used. **Figure 2.20b** Shows the corresponding PICTS spectra, one for each rate window (the spectrum colours are the same as the corresponding rate window colours in **Figure 2.20a**). From each spectrum it is possible to extract e_t (indicated in the legend), and T_m (shown as coloured dots on the x-axis). Finally, these values are plotted on an Arrhenius plot, as shown in **Figure 2.20c** (each point has the same colour as its corresponding spectrum and rate window in the two previous figures). The scatter points fall nicely on a straight line, as expected from Equation 2.9. A linear fit, shown as a solid red line, allows to extract E_a and σ from the slope and intercept, respectively. The fit yields $E_a = 0.487$ eV and $\sigma = 1.5 \cdot 10^{-19} cm^2$, which nicely agree with the real values of 0.5 eV and $1 \cdot 10^{-19} cm^2$. An even better agreement can be achieved by increasing the number of rate windows, as will be shown in the following section.

In principle, the PICTS technique also allows to estimate the trap concentration N_t, assuming that light excitation is high enough to saturate all traps, so that, in Equation 2.7, $n_t(0) = N_t$. If a high value of β (>4) is chosen, then the following approximation holds: $\tau_t(T_m) \approx t_1$. This allows to approximate the height of the PICTS peak as [102]:

$$\Delta i(T_m) = q\left(\frac{Ld^*}{l}\right) V\mu_n\tau_n N_t/(\exp(1)\cdot t_1) \tag{2.13}$$

where $L \cdot l$ is the illuminated area, d^* is the excited layer thickness and V is the applied voltage. By knowing $\mu_n \tau_n$ in the whole temperature range and d^*, it is possible to estimate N_t. However, this is often an experimental challenge that only yields a rough estimation of the trap concentration. Indeed, measuring a reliable value of $\mu_n \tau_n$ in a large temperature range may be experimentally complicated, and for estimating d^* temperature-dependent measurements of the absorption coefficient of the material are needed.

The normalized double-gate method

The theory reported above assumes that the mobility μ_n and lifetime τ_n of carriers appearing in Equation 2.7 are temperature-independent. This is often not the case, and such dependence may introduce artefacts in the spectra, that complicate the analysis. To overcome this issue, a possible approach is to normalise all transients by the photocurrent value $i_{photo} = i_0 - i_\infty$, i.e.

$$i_{norm}(t) = \frac{i(t) - i_\infty}{i_{photo}} \qquad 2.14$$

here, the dark current is also subtracted to remove the dark current baseline. This procedure removes from $i(t)$ the pre-exponential factor containing the $\mu_n \tau_n$ product, and any temperature dependence that it carries. Then, the double-gate analysis as described above can be applied to $i_{norm}(t)$. Since this signal does not contain information on the preexponential factor, it is not possible to extract the trap concentration from it.

In this thesis work, most PICTS spectra were obtained with the normalized double-gate method, since all samples showed a temperature of dependence of the mobility-lifetime product.

The four-gate and integral rate window method

The four-gate rate window method was introduced by Balland at al.[86] to improve the spectral resolution of PICTS with respect to the double gate method. However, we found this method tends to introduce noise and artefacts in the PICTS results, so we only used the double-gate method for all results reported in this thesis. Nonetheless, with our setup, it is possible to perform measurements also in this mode, so we describe it in Appendix B for completeness. In this Appendix we also report the integral PICTS methods, which can be applied to both double-gate and four-gate techniques. These methods were recently used by Pecunia et al.[98] to analyse their PICTS results on perovskite-inspired materials. We found this technique to reduce noise, but to negatively affect resolution of PICTS signals, so we never employed it on the data shown in this thesis.

2.6.3 Analysis implementation

In this thesis work, I implemented the PICTS data analysis by coding a python library that is available at the GitHub repository https://github.com/gioarma/mylib. All functions used for this analysis are inside the `PICTS.py` submodule. This library allows to import the data that come from the data acquisition setup, visualize them, extract the relevant parameters, and finally export the results for further analyses and comparisons. One of the most useful features contained in this library is the automatic rate window generation, that will be briefly discussed below.

Automatic rate window generation – the PICTS map

The choice of a set of rate windows is typically performed arbitrarily by the experimentalist. Indeed, the rules described in the previous section are not enough to uniquely define a set of rate windows, and the choice of several parameters is left to the user. This can lead to a selection of rate windows that is only a portion of the whole Arrhenius space available from the raw data, causing loss of information. To overcome this issue, I implemented a method for automatic rate window generation. This removes some of the arbitrariness in the process, and leads to a more robust and reliable method to extract PICTS parameters.

This method is implemented in the `picts_map` function of the python library. The user has to specify the following parameters:

- `t1_min`: the t_1 value of the first rate window. It should be chosen as close as possible to $t = 0$, while avoiding the first rapid decay related to band-to-band recombination (i.e. at point E in **Figure 2.18**)
- `beta`: as defined by Equation 2.12. It is typically chosen between 1.5 and 4.
- `t1_shift`: a time value that indicates the time shift between different rate windows.

Based on these parameters, the software automatically generates a set of rate windows that covers the largest time range possible between $t = 0$ and the end of the transient. The time shift between rate windows can be either linear or exponential. In the linear case, the t_1 values are calculated as $t_{1,min} + t_{1,shift} \cdot i$, where i is an integer ranging from 0 to the maximum number of rate windows allowed by the data and the parameters of choice. In the exponential case, the

t_1 values are calculated as $t_{1,min} \cdot \exp(t_{1,shift} \cdot i)$. The latter method is more suited for PICTS, as it follows the exponential shift of the emission rate with temperature predicted by the theory.

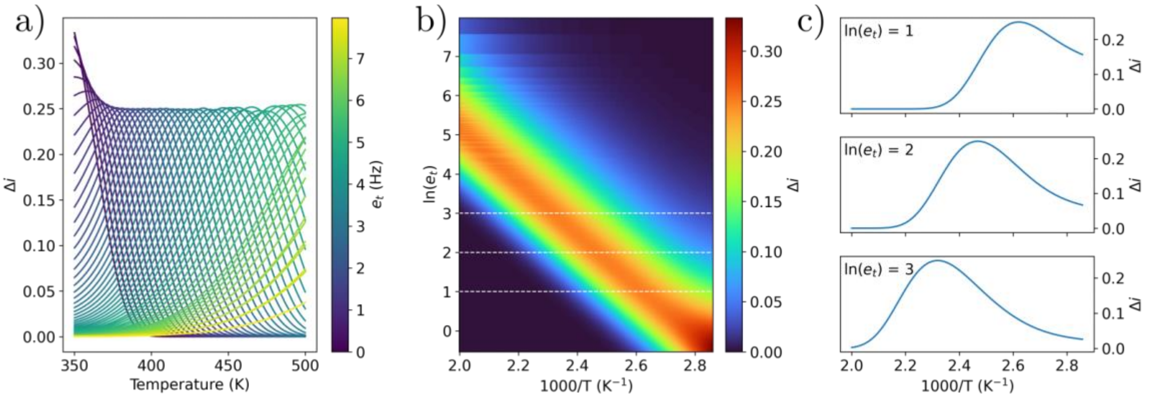

Figure 2.21 a) PICTS spectra of the simulated transients shown **Figure 2.19**, obtained by the automatic rate window generation of the `picts_map` function. **b)** PICTS map representation of the spectra shown in (a). **c)** Horizontal profiles of the PICTS map extracted at the values of $\ln(e_t) = \{1, 2, 3\}$, represented by white dashed lines in (b).

Figure 2.21 shows the application of this procedure to the simulated data of **Figure 2.19**. As shown in **Figure 2.21a**, this method produces a large number of PICTS spectra (here only 1/5 of them are shown, for allowing to distinguish among curves of different spectra). Such visualization is not ideal, as it is difficult to interpret. Therefore, we opted for a colormap visualization, as shown in **Figure 2.21b**, where the PICTS signal (Δi) is plotted as a function of inverse temperature on the x-axis and the logarithm of the emission rate on the y-axis. This is referred to as the *PICTS map*. With a rainbow colour map as the one chosen here, trap signatures appear as red lines with negative-slope. A PICTS map can therefore be regarded as a “3D Arrhenius plot”, as the quantities on the x and y axis are already the ones shown in an Arrhenius plot (see **Figure 2.20c** for reference). The PICTS map still contains all information on the original spectra, e.g. **Figure 2.21c** shows three horizontal profiles of the map for $\ln(e_t) = \{1, 2, 3\}$, represented by white dashed lines in **Figure 2.21b**.

Another advantage of this method is to yield a large number of data points to produce the Arrhenius plot of a trap. This allows for better linear fit accuracy, and thus for better trap parameter estimation. For example, the map in **Figure 2.21b** allowed to obtain an Arrhenius plot with 18 points, compared to the 5 points of **Figure 2.20c**. The result is a fitted activation energy of 0.499 eV, with an error 0.2% on the real value of 0.5 eV. This is to be compared with the 2.6% error obtained with the 5-point Arrhenius plot reported in the previous section.

Analysis procedure

In the following, I briefly describe a typical procedure for analysis of PICTS data using the `PICTS.py` module. Each step has a dedicated function, so the procedure will be described by explaining how each function works.

- `read_transients`. Imports the data contained in the TDMS file saved by the LabView acquisition software. It allows to rescale the data based on the amplifier gain used for the measurement (voltage/current conversion).
- `normalize_transients`. Allows to normalize all transients between 0 and 1. This is normally done as most samples in this thesis work show temperature-dependent mobility-lifetime product.
- `picts_map`. Generates the PICTS map, as described in the previous paragraphs. The rate window generation method is normally the exponential one.
- `map_fit`. Allows to perform an Arrhenius fit on all trap signatures visible in the map. To overcome the issues introduced by noise in the determination of T_m, a gaussian fit is performed on the peaks and T_m is taken as the temperature of the gaussian maximum. This function returns the gaussian fits, the Arrhenius datapoints and their fit, and the trap parameters E_a and σ.
- `save_arrhenius`. Allows to export the Arrhenius fits and the trap parameters as CSV files for further analysis.

These are complemented by plotting functions that return interactive plots. Interactivity is key, as it allows, if necessary, to check one by one all curves at each stage of the analysis, and to accurately select the best parameters for the Arrhenius fitting procedure.

Chapter 3

Experimental results

This chapter contains the main experimental results of this thesis work. The focus of my research was on defects in metal halide perovskite (MHP) materials and devices. My studies focussed on two topics: intrinsic defects, and extrinsic defects. To the first category belong the investigation of electronic defects in 2-dimensional MHPs single crystals and of ion migration phenomena in 3-dimensional MHP single crystals. To the extrinsic defects category belong studies on the impact on MHP devices of external factors like X-ray irradiation, mechanical stress, or exposure to oxygen and moisture. In the first section, I report the results of a study on the effects of X-ray irradiation on the optoelectronic properties of MHP single crystals. In the second section, I show the results of an investigation of delamination phenomena on silicon/perovskite tandem solar cells. In the third and fourth sections, I show how electronic defects and ion migration can be characterized in 2-D and 3-D MHPs by means of photo-induced current transient spectroscopy. The last two sections focus on the impact of moisture on the optoelectronic properties and performance of MHP single crystals, both during growth and in-operando.

3.1 Impact of X-ray irradiation on the optoelectronic properties of hybrid lead halide perovskites

In this section, I report the results of a radiation hardness study performed on $MAPbBr_3$ single crystals. In this study, SPS and PL spectroscopy allowed to investigate the modifications induced by X-ray irradiation on the opto-electronic properties of the material. X-ray photoelectron spectroscopy allowed to determine the chemical origin of such modification. The study focussed on the effects of X-ray irradiation in air, a condition that was missing in the published literature, that mainly focussed on such effects under vacuum atmosphere. This work was carried out in collaboration with researchers at the CNR of Bologna: Francesco Borgatti (CNR-ISMN), Alessandro Kovtun (CNR-ISOF), Gabriele Calabrese (CNR-IMM), and Silvia Milita (CNR-IMM). The results were published in December 2021 on ACS Applied Materials and Interfaces [17].

Part of this section is reprinted with permission from reference [17]. Copyright 2021 American Chemical Society.

3.1.1 Introduction

Despite the large interest for metal halide perovskites (MHPs) as X-ray detectors described in Chapter 1, the effect of strong and prolonged irradiation by X-rays on these materials is still not clarified. Only a few studies on ionizing radiation effects have been published on the topic. Xu et al.[139] have investigated gamma radiation effects in $MAPbBr_3$, finding relevant structural modifications after high dose irradiation (in the kGy range). Other studies reported surface degradation with formation of metallic lead on $MAPbBr_3$ after X-ray[79] or electron[140] irradiation. On the other hand, other groups reported MHP solar cell operation to be stable even after high dose irradiation, demonstrating an excellent radiation hardness of these devices.[141,142] The study here presented aims to assess the effects of X-ray irradiation in the range of interest for diagnostic applications (up to hundreds of Gy) on the optoelectronic properties of $MAPbBr_3$ single crystals.

3.1.2 Optical characterization

To evaluate the effects of X-ray irradiation on the optical absorption properties of a $MAPbBr_3$ single crystal, we collected SPS spectra on the as-grown sample and after each step of irradiation with a fixed X-ray dose of 40 Gy. The evolution of the SPS spectrum with the cumulated dose is presented in **Figure 3.1a**. The spectrum of the pristine sample (black curve) shows the typical Wannier-Mott excitonic peak (here referred to as T1) generally observed in the absorption spectrum of this material.[45,143] T1 disappears as soon as the first X-ray dose is delivered, revealing the band-to-band absorption edge and a new peak at lower energies (T2), which increases proportionally to the absorbed dose. This effect cannot be ascribed to sample aging, as demonstrated by the consistency in time of the SPS spectra of a control sample (**Figure 3.1b**), which was not exposed to X-ray radiation. The time intervals between successive acquisitions for the control sample were chosen to be the same as for the irradiated sample. This effect is reversible in a timescale of 1 week of storage in dark conditions inside a desiccator with less than 20% humidity (gray curve in **Figure 3.1a**). **Figure 3.1c** shows the evolution with X-ray dose of the PL spectrum. The PL lineshape is not affected by X-ray exposure, indicating that T2 states are not emissive. The PL intensity instead is significantly affected, with a drop by more than 60%, to be compared with a less than 20% drop in the control sample (**Figure 3.1d**). The decrease in PL intensity is consistent with the quenching of the excitonic peak T1. Indeed, in this material, PL at room temperature arises mainly from the recombination of the Wannier-Mott exciton ground state.[32,45,144] In contrast with SPS, the PL intensity after 1 week (gray curve in Figure 1c) only shows a partial recovery of about 20%, indicating that the photophysical properties of the material are not fully recovered.

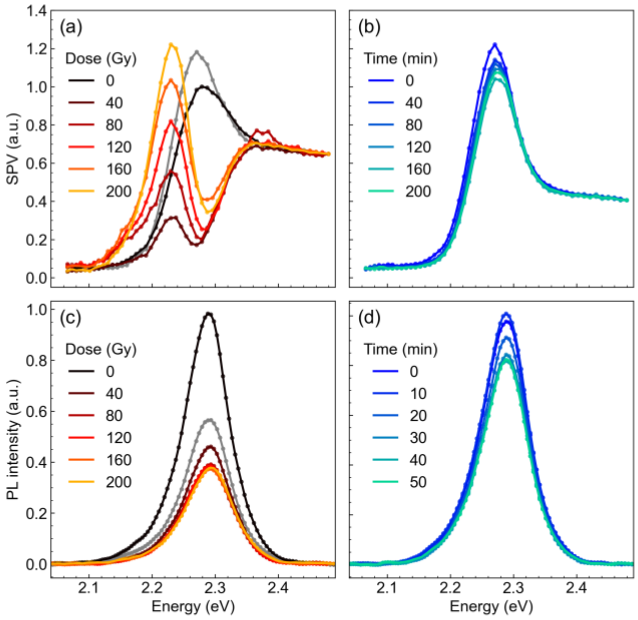

Figure 3.1 (a,b) Surface photovoltage and **(c,d)** photoluminescence spectra of an $MAPbBr_3$ single crystal as a function of X-ray dose for the irradiated sample **(a,c)** and as a function of time for the control sample **(b,d)**. The gray curves in **(a,c)** show the SPS and PL spectra after 1 week of storage. Reprinted with permission from reference[17]. Copyright 2021 American Chemical Society.

According to Sestu et al.[145], and given the direct proportionality between the SPV signal and the absorption coefficient α, we analyzed our SPS spectra by means of Elliott's formula.[146] This formula describes the absorption spectrum of a direct bandgap semiconductor as the sum of two terms: excitonic absorption (characterized by the binding energy E_b) and band-to-band absorption (characterized by the energy gap E_g). Both contributions are phenomenologically convoluted with a gaussian function $g(E)$ of width Γ, yielding the following equation:

$$\alpha(\hbar\omega) = \mu_{cv}^2\sqrt{E_b}\left[2a_x E_b g\left(\frac{\hbar\omega - (E_g - E_b)}{\Gamma}\right) + \int_{E_g}^{\infty} g\left(\frac{\hbar\omega - E}{\Gamma}\right)\cdot\frac{1 + b(E - E_g)}{1 - \exp\left(-2\pi\sqrt{\frac{E_b}{E - E_g}}\right)}\right] \tag{3.1}$$

where μ_{cv}^2 is the transition dipole moment and $b\left(E - E_g\right) = 10\left(\frac{m^2E}{\hbar^4}\right)c_{np}$, with m being the electronic mass, $\hbar$ being the reduced Planck's constant, and c_{np} accounting for nonparabolic conduction and valence bands: $E(k) = \frac{\hbar^2k^2}{2m} - c_{np}k^4$, with k being the electronic wavevector. We set $b = 0.91\ eV^{-1}$, based on typical parameters for MAPbBr$_3$.[145] We introduced the a_x parameter as a scaling factor for the excitonic component with respect to the continuum one, accounting for the scaling of the T2 peak with X-ray dose. We fixed $a_x = 1$ for the spectrum at 0 Gy, leading to the standard Elliott formula in the case of a pristine sample. We note that in Equation 3.1 we reported only the ground-state (1s) contribution of the excitonic absorption, i.e., the only one observable at room temperature. In general, the difficulty of fitting experimental absorption spectra by Equation 3.1 arises from the strong convolution of the exciton and continuum part of the spectrum. However, in our spectra after irradiation, the complete quenching of the T1 peak allows us to clearly resolve the continuum absorption.

We took advantage of this phenomenon, and first used Equation 3.1 to fit the absorption spectrum after irradiation in the energy range of the band-to-band absorption in order to extract the value of the energy gap. We obtained a value of $E_g = 2.30 \pm 0.01\ eV$, in agreement with values reported by other groups.[147] We kept the energy gap fixed to this value in the following fit procedure to reduce as much as possible the number of free parameters. Next, we fitted the spectra in the range 2.1−2.33 eV by letting E_b and Γ as free parameters. We excluded from the fit the high energy end of the spectrum (above 2.33 eV), where defect-induced surface recombination quenches the SPV signal and the proportionality between SPV and α does not hold. **Figure 3.2** shows the resulting fit (red curve) for the 0 and 200 Gy spectra, as well as the excitonic (orange and red areas) and continuum (light blue areas) components. The fit yields an exciton binding energy of 39 ± 2 meV at 0 Gy for the T1 peak and of 76 ± 7 meV at 200 Gy for the T2 peak. Both these values are comparable with the wide range of values reported in the literature so far. [148,149]

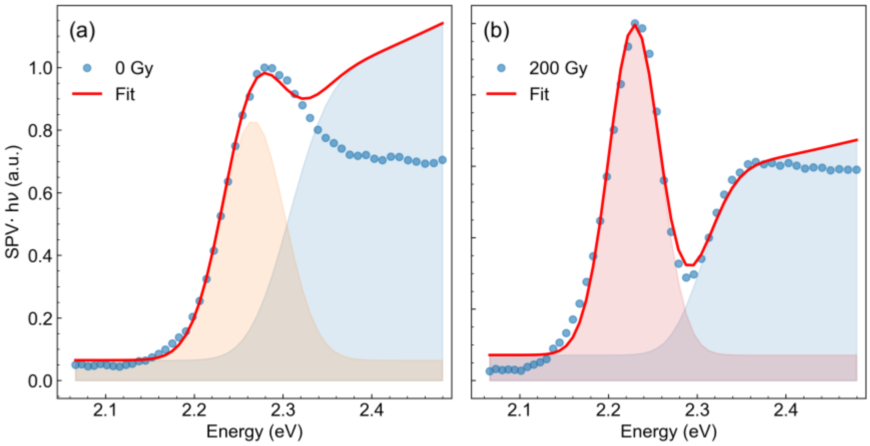

Figure 3.2 Fitting of SPS spectra by means of Elliott's formula at **(a)** 0 Gy and **(b)** 200 Gy. The blue circles represent the experimental data; the red curve shows the fit result. The blue shaded areas represent the band-to-band (continuum) fit component. The orange and red areas represent the T1 and T2 excitonic fit components, respectively. Reprinted with permission from reference[17]. Copyright 2021 American Chemical Society.

3.1.3 Compositional and structural characterization

XRD characterization

To understand whether the X-ray irradiation effects observed in SPS spectra can be ascribed to structural modifications in the sample, we carried out high-resolution X-ray diffraction (HR-XRD) analysis on a sample before and after 200 Gy irradiation. The XRD profile (**Figure 3.3a**) shows three diffraction peaks relative to the 001, 002, and 003 directions, which match the expected pattern for a $MAPbBr_3$ single crystal at room temperature. The high resolution of the XRD profiles allows to see the changes in the peak position and shape with resolution below 0.01°. **Figure 3.3b-d** shows a detail of the three XRD peaks before and after 200 Gy irradiation. These do not show any relevant difference in peak intensity or shape. Thus, we concluded that the X-ray induced T2 peak cannot be ascribed to structural modifications in the crystal.

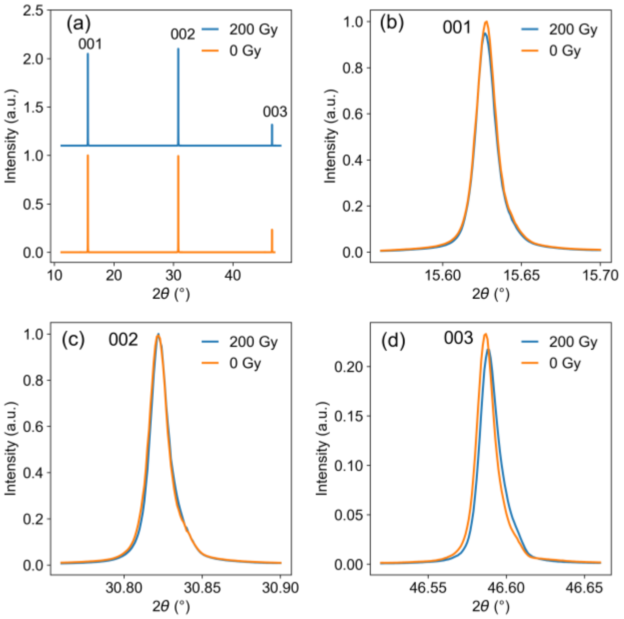

Figure 3.3 a) High resolution X-ray diffraction spectrum of a MAPbBr3 single crystal before (orange curve) and after (blue curve) 200 Gy irradiation by W target X-ray tube. Detail of 001 **(b)**, 002 **(c)** and 003 **(d)** diffraction peaks. Reprinted with permission from reference[17]. Copyright 2021 American Chemical Society.

XPS characterization

Having excluded a structural cause to the effect observed by SPS, we moved to a compositional analysis by means of X-ray photoelectron spectroscopy (XPS). This technique allows to investigate the relative amount and the chemical state of different elements on the surface, which in this material is expected to be highly sensitive to the chemical interactions with the environment. According to the TPP-2 M formula, [150,151] the inelastic mean free path of the photoelectrons in the core-level spectra measured by XPS ranges from 1.7 to 2.5 nm, thereby setting the mean probing depth of the XPS measurements around 6−7 nm. This information is complementary to the SPS results, whose probing depth is of the order of few microns.

Before performing the experiment on samples irradiated with the W target X-ray tube, we carried out an experiment to study the impact of the X-ray source in the XPS apparatus on the sample’s properties. We acquired five consecutive XPS spectra (1h time for each acquisition) on a pristine sample, for a total of 5h exposure to the XPS source. The resulting spectra for the Pb 4f and Br 3d are shown in **Figure 3.4a-b**. We observed the appearance of a metallic lead (Pb^0) component in the spectrum, as well as a decrease in in the Br/Pb ratio, in agreement with previous studies. [79,152] The N/Pb ratio was unchanged during the experiment. After the first XPS scan, the Pb^0/Pb ratio is approximately 7%. Therefore, any metallic lead detected below this limit could be due to the XPS source itself, rather than to other factors. **Figure 3.4c** shows the SPS spectra of the crystal before and after the five XPS measurements. The disappearance of T1 and the appearance of T2 are observed also in this case. This observation is key for the interpretation of the results, as will be discussed in the next section.

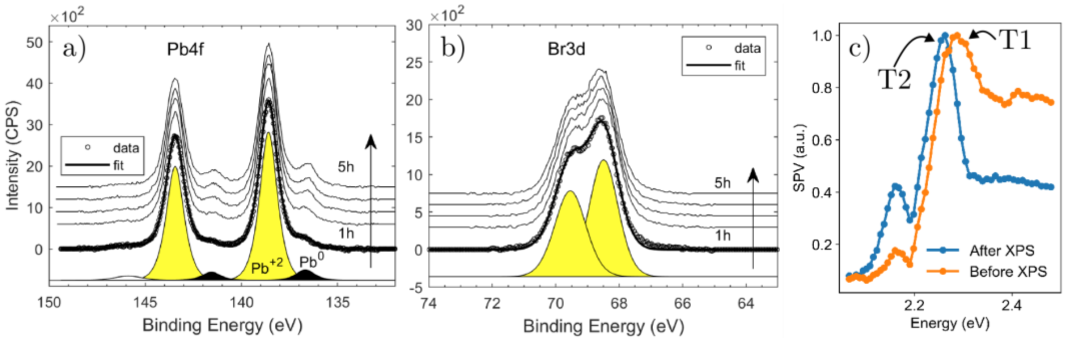

Figure 3.4 Time evolution during XPS calibration experiment to quantify the damage of the XPS beam on the crystals. Pb 4f and Pb^0 **(a)**, and Br 3d doublet **(b)** are reported. The fitting curves are displayed in yellow for Pb^{+2} and Br 3d, and in black for Pb^0. An offset was added to the curves for clarity purpose. **c)** SPS spectra of the crystal before and after the XPS measurements in (a) and (b). Reprinted with permission from reference[17]. Copyright 2021 American Chemical Society.

These results fit well with the degradation mechanism proposed by Wang et al.[79] under X-rays and in ultra-high vacuum (UHV):

$$\mathrm{CH_3NH_3PbBr_3} \xrightarrow{X-ray} \mathrm{CH_3NH_3Br} + \mathrm{Pb^0} + \mathrm{Br_2} \uparrow \qquad \text{(in UHV)} \tag{3.2}$$

Here, the loss of bromine by XPS is explained by the formation of the volatile Br$_2$ molecule that leaves the sample surface, leaving methylammonium bromide and metallic lead residuals.

We then moved to the XPS characterization after X-ray irradiation in air with the W target X-ray tube. We performed XPS scans on three samples grown from the same precursor solution and exposed to the W target X-ray source in air with increasing dose: 0 Gy (control sample), 60 Gy, and 120 Gy. The measurements were performed immediately after irradiation and repeated after 1 week of storage. **Figure 3.5a-d** shows the Pb4f, Br3d, N1s, and O1s core-level spectra measured for the three samples immediately after irradiation. All spectra were normalized to the same height for better line-shape comparison. **Figure 3.5e** shows the elemental ratios with respect to the total amount of Pb, calculated from the XPS spectra as a function of absorbed dose, both immediately after irradiation (bars in solid colour) and after 1 week of storage (bars in semi-transparent colour). The ratios were calculated relatively to the total amount of Pb using the intensity of the core-level peaks obtained by the fitting analysis of the XPS spectra. The numerical values of the elemental ratios are reported in **Table 3.1**.

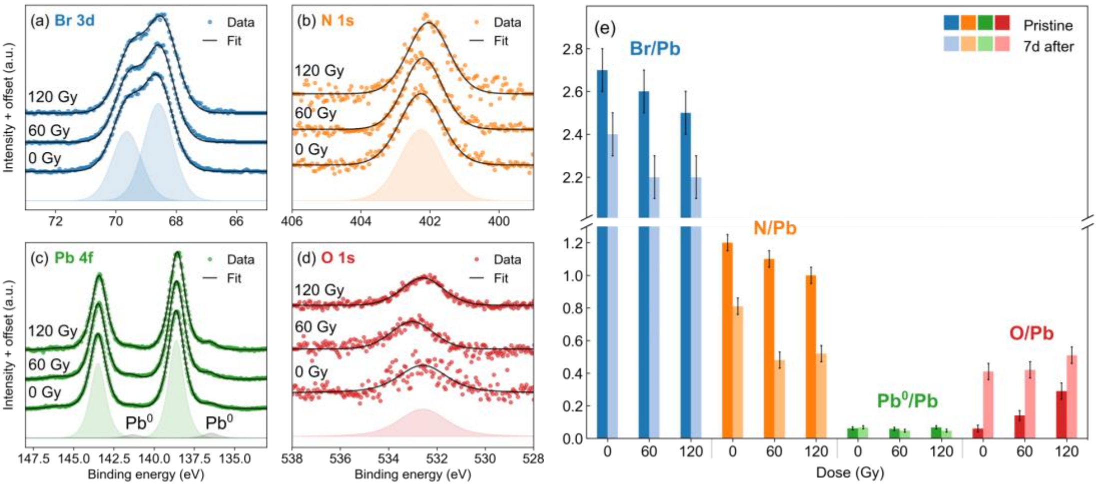

Figure 3.5 a-d) XPS spectra of Pb4f, Br3d, N1s, and O1s measured on three $MAPbBr_3$ crystals exposed to 0 Gy (control sample), 60 Gy, and 120 Gy X-ray radiation in air. Each graph shows the experimental data as dots and the fitting curve as black solid lines. The components of the fitting curves for the 0 Gy sample are displayed as shaded areas. **e)** Elemental ratios with respect to the total amount of Pb calculated from the XPS spectra as a function of absorbed dose, both immediately after irradiation (bars in solid colour), and after 1 week of storage (bars in semi-transparent colour). Reprinted with permission from reference[17]. Copyright 2021 American Chemical Society.

The amount of oxygen, negligible in the control sample, roughly doubles at every dose step, while both Br and N concentrations drop proportionally to the dose. The oxygen peak at 533 eV is ascribed to the formation of H_2O in situ.[79] The relative amount of Pb^0 is 6−7% for all samples, contrary to the increase in metallic lead observed previously for irradiation in UHV with the XPS source. This suggests that irradiation in air does not produce metallic lead, as opposed to the case of irradiation in vacuum, probably due to a more complex chemical reaction involving air molecules. Based on these observations, we propose that upon X-ray exposure in environmental conditions, $MAPbBr_3$ reacts with oxygen undergoing the chemical reaction

$$\mathrm{CH_3NH_3PbBr_3} + \frac{1}{4}\mathrm{O_2} \xrightarrow{X-ray} \frac{1}{2}\mathrm{H_2O} + \mathrm{PbBr_2} + \mathrm{CH_3NH_2}\uparrow + \frac{1}{2}\mathrm{Br_2}\uparrow \tag{3.3}$$

An equivalent degradation process was proposed by Senocrate et al. for $MAPbI_3$.[12] This reaction occurs also in dark conditions, but high energy radiation is likely to accelerate it through creation of superoxide intermediates O^{2-}, as reported by other groups in the case of visible light irradiation.[153] Such reaction is consistent with the loss of N, leaving the sample in form of gaseous CH_3NH_2, with the loss of Br, forming gaseous Br_2, and with the formation of H_2O in situ.

Dose (Gy)	Pb	Br	N	Pb^0/Pb (%)	O/Pb (%)
0	1.0	2.7 ±0.1	1.20 ±0.05	6.2	6.0
60	1.0	2.6 ±0.1	1.10 ±0.05	5.8	14.0
120	1.0	2.5 ±0.1	1.00 ±0.05	6.8	29.0
0 (7 days)	1.0	2.4 ±0.1	0.81 ±0.05	6.8	41.0
60 (7 days)	1.0	2.2 ±0.1	0.48 ±0.05	4.7	42.0
120 (7 days)	1.0	2.2 ±0.1	0.52 ±0.05	4.7	51.0

Table 3.1 Elemental ratios as measured by XPS on samples irradiated with W target X-ray source in air. The first column indicates the X-ray dose to which the sample was exposed. The following three columns indicate the concentration of Pb, Br and N relative to Pb. Note that the Pb signal includes both the Pb^0 and the Pb^{2+} contributions. The last two columns report the percentual contribution of Pb^0 to the total Pb signal and percentual ratio of oxygen amount with respect to Pb, respectively.

After 1 week of storage, all the samples show a drop in Br and N content, as well as an increase in O concentration. This is compatible with the degradation reaction 3.3 in environmental conditions proposed above, although in dark conditions. Indeed, as discussed above, such reaction occurs also in the dark, and photons have the effect of accelerating it. In general, the irradiated samples show stronger degradation after 1 week with respect to the control sample, with higher loss in Br and N content. We note, however, that 1 week of exposure to air in the dark degrades the sample more than the exposure to an X-ray dose as high as 120 Gy. This suggests that environmental reactivity is more concerning than X-ray damage for these materials.

3.1.4 Discussion and conclusions

Based on the results shown above, we now propose an interpretation for the appearance of the radiation-induced excitonic peak T2 in the absorption spectrum of $MAPbBr_3$. It is important to note that we observed the T2 peak in the SPS spectrum even after the XPS calibration experiment, where the sample was irradiated in an ultrahigh vacuum inside the XPS chamber (**Figure 3.4c**). In that case, we detected neither nitrogen loss nor increase in oxygen. Thus, the only degradation process observed by XPS for both air and vacuum irradiation is the loss of Br. Therefore, we propose bromine vacancies (V_{Br}) to be responsible for the formation of the T2 species. The only process that can be related to a recovery in the material as observed by SPS is the increase in oxygen. Therefore, we propose that environmental oxygen and water fill the bromine vacancies produced by X-ray irradiation, leading to a passivation effect and thus to a recovery of the SPS spectrum. This hypothesis is supported by recent results by Shin et al. who observed iodine vacancy filling upon exposure of $MAPbI_3$ films to air after intentional vacancy creation.[154]

The creation of V_{Br} induced by X-ray irradiation can change the dipole moment in the crystal, as suggested by Anusca et al.,[155] and thus can affect the dielectric behaviour of the material, i.e., the ability of ions in screening electron−hole Coulomb interactions. As perovskites are polar materials, Coulomb interactions among charge carriers are screened by local lattice polarization and transport properties of these crystals are better discussed in terms of polarons.[32,148] The coupling of charged carriers with the lattice polarization results in an increase of their effective mass, which can be approximated in the weak coupling regime as

$$\frac{\mu^*}{m_0} = \frac{\mu}{m_0}\left(1 + \frac{\alpha_p}{6}\right) \qquad 3.4$$

with m_0 being the free electron mass, μ the bare effective carrier mass (resulting only from band dispersion, neglecting interaction with phonon polarization), μ^* the polaronic effective mass, and α_p the dimensionless Fröhlich coupling constant.

If we assume that the Bohr model for excitons can be adopted,[32] the exciton binding energy can be written as

$$E_b = \frac{R_0 \mu}{m_0 \varepsilon_r} \qquad 3.5$$

with R_0 being the Rydberg constant, and ε_r the effective material dielectric function. By using the dielectric function accounting for ionic screening $1/\varepsilon_r$= 0.18 reported by Sendner et al.[156], and our experimental result E_b = 39 meV, we obtain $\frac{\mu^*}{m_0}$ = 0.09 for the pristine sample, in close agreement with literature values.[157] The appearance of the T2 transition after irradiation can be attributed to a bound exciton whose effective mass becomes heavier due to the interaction with the lattice, i.e., to polaronic species. If we assume that we can use Equation 3.5 for the estimation of the effective mass μ^* of this new species, using a value of E_b = 76 meV, as measured by SPS for T2, we obtain $\frac{\mu^*}{m_0}$ = 0.17. Therefore, the effective mass significantly increases due to exciton−phonon interaction. The relative Frölich coupling constant α_p, as calculated from Equation 3.4, becomes equal to 5.7, much larger than the value of 1.69 reported by Sendner et al. for this material in pristine conditions.[156]

In conclusion, X-ray irradiation creates bromine vacancies in the lattice, which induce a considerable increase in the Frölich coupling constant. While transition T1 is due to free excitons weakly coupled to phonons, transition T2 can be related to excitons strongly coupled with phonons. Lattice deformation and dynamic lattice screening prevent electron−hole radiative recombination for T2, explaining why no T2 contribution is detectable by PL spectroscopy. After 1 week of air exposure, water and oxygen content increases as observed by XPS. We propose that water and oxygen filling helps reducing bromine vacancy concentration, restoring the normal lattice screening and causing the recovery of the T1 excitonic species. This study is an important step forward in the understanding of the physical phenomena that X-ray irradiation causes to $MAPbBr_3$, one of the most promising materials for next generation ionizing radiation detectors. Our characterization of the effects of irradiation in air provides insight on the crucial aspects to be considered when designing $MAPbBr_3$-based devices for real-world applications.

3.2 Mechanical Reliability of Fullerene/Tin Oxide Interfaces in Monolithic Perovskite/Silicon Tandem Cells

In this section, I report the results of KPFM measurements on perovskite/silicon tandem solar cells. This study allowed to identify the interface that causes the problem of delamination in perovskite/silicon tandem solar cells. This work was carried out in collaboration with researchers of the Solar Center and of the Mechanics of Composites for Energy and Mobility Lab at the King Abdullah University of Science and Technology (KAUST), in Saudi Arabia: Michele De Bastiani, Rawan Jalmood, George T. Harrison, Xiaole Li, Ran Tao, Stefaan De Wolf, and others. The results were published in January 2022 on ACS Energy Letters.[18]

Part of this section is reprinted with permission from reference [18]. Copyright 2022 American Chemical Society.

3.2.1 Introduction

In the past few years, monolithic perovskite/silicon tandems, combining perovskite and silicon solar cell technologies, have enabled high power conversion efficiencies (PCEs) in a possible cost-effective way, which holds great promise for their mass production.[158,159] To date, most of the tandem research has focused on pursuing PCE increases,[160–162] often by introducing sophisticated stacks of materials. However, for commercialization, tandems need to be integrated into solar panels, which may pose significant cell-to-module related technological challenges, which urgently need to be identified and mitigated. Conventional monofacial single-junction crystalline silicon (c-Si) photovoltaic (PV) modules consist of a front glass sheet, strings of series-connected c-Si solar cells, sandwiched between two encapsulant layers (front and rear, at present usually made from ethylene vinyl acetate, EVA), and a polymeric backsheet.[163] This stack is then laminated by vacuum annealing to melt and solidify the encapsulant layers, which also aids in anchoring the strings of cells in the module. For module integration of perovskite/ silicon tandem solar cells, this process should be altered. Indeed, due to the sensitivity of perovskites to moisture, the backsheet needs to be replaced with a rear glass sheet, acting as a more effective barrier. However, classic module lamination tends to shrink the encapsulant layers upon solidification, which can be several centimeters over the module dimensions. We find this often to cause tandem-device delamination, resulting in catastrophic module failure. For lab-scale devices, this can be resolved by removing the encapsulant layers and sealing the glass/glass modules only at their edges, for instance with butyl-rubber derivatives. However, for larger modules, the absence of encapsulants may compromise the anchoring and structural stability of the strings of fragile cells. Therefore, understanding and resolving tandem delamination is a key challenge toward its commercialization.[164]

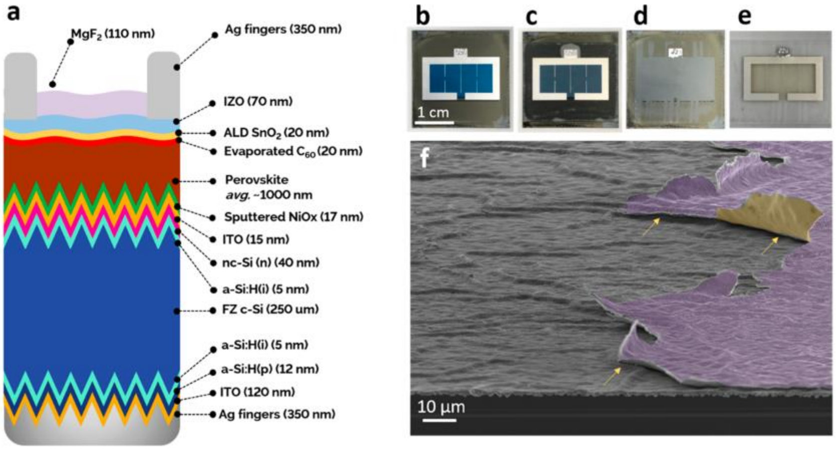

Figure 3.6 a) Schematic representation of the structure of the p-i-n tandem solar cell. **(b)** Picture of the tandem solar cell, **(c)** covered by tape, **(d)** after the peeling, with the emerging surface, and **(e)** peeled part left on the tape. **(f)** False-coloured tilted SEM image of the peeled electrode. The peeled surface presents the typical wrinkles of the perovskite surface. The purple area represents the top of the Ag/MgF2 electrode, while the yellow area the lift-off film that delaminated. The yellow arrows indicate the interface where delamination happens. Reprinted with permission from reference[18]. Copyright 2022 American Chemical Society.

In this work, we investigated the nature of delamination mechanism in state-of-the-art p-i-n perovskite-silicon tandems fabricated at the KAUST Solar Center. The solar cell structure is reported in **Figure 3.6a**, and **Figure 3.6b** shows a picture of the device. To intentionally delaminate the solar cell, the device is covered by tape (**Figure 3.6c**), which is then peeled. This process leaves an exposed layer on the device side (**Figure 3.6d**), and another on the tape side (**Figure 3.6e**). Tilted-angle scanning electron microscopy (SEM) images at the peeling interface (**Figure 3.6f**) allowed to characterize the interface between the peeled and pristine area. At the bottom of the image, the typical textured surface of the c-Si bottom cell is visibly covered by the perovskite layer. The perovskite exhibits on its surface the characteristic wrinkles induced during the crystallization process. The purple area highlights the top part of the contact (the Ag finger is covered by the MgF_2 anti-reflective coating (ARC)) that is partially lifted, while the yellow area represents the film that delaminated.

3.2.2 KPFM characterization

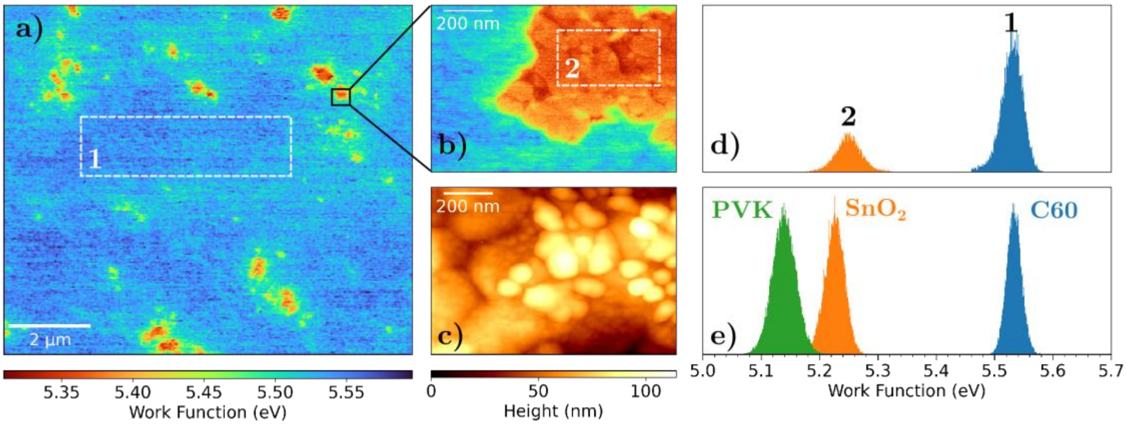

Figure 3.7 a) 10 µm^2 KPFM map of a delaminated tandem solar cell. **b, c)** 1 µm^2 close-up of one of the residuals as measured by KPFM and dynamic AFM morphology, respectively. **d)** Work function distributions of regions 1 (blue) and 2 (orange), corresponding to the regions delimited by dashed rectangles in (a) and (b). **e)** Work function distributions of calibration samples consisting of Si/ITO/perovskite (green), Si/ITO/perovskite/ C_{60} (blue), and Si/ITO/perovskite/ C_{60}/SnO_2 (orange). Reprinted with permission from reference[18]. Copyright 2022 American Chemical Society.

To identify the nature of the layers that delaminate, we investigated the exposed surface by KPFM. The measurements were performed under argon atmosphere, and in dark conditions, to avoid sample degradation during the measurement. **Figure 3.7a** shows a 10 µm^2 KPFM scan of a delaminated tandem solar cell. This map shows the nonuniformity of the delamination at the micrometer scale, with presence of low work function (WF) residuals on top of a high WF substrate. **Figure 3.7b-c** show 1 µm^2 KPFM and morphology close-up maps of one of the residuals, respectively. We note the close correlation between the WF map and morphology, confirming that the micrometer-sized islands are residuals of a different chemical species than the substrate. **Figure 3.7d** shows the distribution of the WFs measured in regions 1 (substrate) and 2 (residual), as indicated in **Figure 3.7a-b** by dashed rectangles. To assess the nature of these two species, we measured WF distributions of calibration samples consisting of Si/ITO/perovskite, Si/ITO/perovskite/ C_{60}, and Si/ITO/perovskite/ C_{60} /SnO_2 structures, shown in **Figure 3.7e** as green, blue, and orange histograms, respectively. A comparison with the distribution of the delaminated solar cell unequivocally shows that the exposed layer consists of a C_{60} film with SnO_2 residuals on top.

3.2.3 Additional measurements

KPFM results were compared with XPS and Energy Dispersive X-ray (EDX) analyses, performed at the KAUST Solar Center. Both techniques confirmed that the exposed layer after delamination is the C_{60} film, therefore confirming the weak interface to be the C_{60}/SnO_2 one. EDX maps revealed that, upon delamination, SnO_2 residuals tend to stick on the *wrinkles* that are typical of the underlying perovskite film. These wrinkles are induced by the presence of Cs in the perovskite formulation and by the textured substrate underneath.[165]

180° peel-off measurements allowed to determine the work of adhesion (WoA) of the solar cell stack. It was found that the work of adhesion of a perovskite/C_{60}/SnO_2 sample is higher than that of the peeling tape interface, indeed no delamination is observed in such sample. This suggests that the C_{60}/SnO_2 is not weak by nature, but is rather weakened during the fabrication process of the full solar cell stack. The most probable cause are the IZO and MgF_2 deposition processes, that heat up the sample up to 50°C. Such high temperatures may cause the above-mentioned weakening of the C_{60}/SnO_2 interface. This hypothesis was confirmed by WoA measurements on perovskite/C_{60}/SnO_2 samples annealed at temperatures of 50°C or higher. Annealed samples delaminated, as opposed to samples that did not undergo any annealing process.

3.2.4 Conclusions

This work allowed to identify the mechanically weak interface of perovskite/silicon tandem solar cells to be the C_{60}/SnO_2 one. This interface was found to be weakened by the morphology of the underlying perovskite layer, and by sample heating during the deposition processes of specific layers of the solar cell. This work allowed to determine the critical materials and procedures that should be adapted in order to engineer delamination-resistant perovskite/silicon tandem solar cells.

3.3 Photo-induced current transient spectroscopy investigation of two-dimensional hybrid lead halide perovskite single crystals

In this section, I show the results of Photo-induced Current Transient Spectroscopy (PICTS) applied to PEA_2PbBr_4, a 2D perovskite material. To our knowledge, this is the first defect characterization of a pure 2D perovskite material ever reported. This work was fully carried out at the Department of Physics and Astronomy of Bologna University. A manuscript with the results contained in this section is currently being prepared for publication in a scientific journal.

3.3.1 Introduction

Two-dimensional perovskites are emerging as promising materials for optoelectronic devices like light-emitting diodes[166,167] and detectors.[128,168,169] Their good stability under moisture makes them also promising as passivating materials that improve the long-term stability of 3D perovskite solar cells.[170] This has attracted a large interest in the scientific community, and the number of scientific papers on 2D perovskites has dramatically increased in the latest years. Despite such large interest, thorough studies on electronic defects in these materials are still lacking.[89] These are key to identify the chemical and structural issues to be addressed to unlock the full potential of such materials.

The groups of Bruno Ehrler and Carsten Deibel, some of the most active in the field of defect characterization in perovskites, focussed on mixed 2D/3D perovskites, that are mostly used for LEDs fabrication.[107,110] However, being mixed perovskites, their defect physics is expected to largely differ from that of pure 2D perovskites. Moreover, these studies, based on Transient Ion Drift (TID) measurements, yield ion migration parameters, rather than electronic defect parameters. Shikoh et al.[116] performed TID measurements on a 3D/2D perovskite heterostructure, but the contribution of the 2D layer is difficult to deconvolve from the one of the 3D layer, and also in this case the analysis did not yield electronic defect parameters, but rather ion migration ones. A similar study was also performed by Heo et al.[171] on a solar cell with a 2D passivation layer on top of the 3D active layer. In this case, the extracted parameters were interpreted as related to electronic defects, but a comparison with the above-mentioned studies suggests that, also in this case, they are most probably affected by ion migration in the 3D layer.

None of the above-mentioned studies was performed on pure 2D perovskite samples, without any 3D perovskite component. However, also pure 2D perovskite devices are extremely interesting for applications. Thanks to their high resistivity and low dark current, one of the most interesting fields for pure 2D active layers is for UV and X-ray detection. For example, PEA_2PbBr_4 was recently shown to be a promising material for both applications by Zhang et al.,[169] and Lédée et al.[128]

Despite this interest, what is hindering the investigation of electronic defects in these materials is that conventional DLTS is notoriously difficult to carry out on highly resistive materials.[85,102] Another problem is that researchers struggle to fabricate an effective p-n or Schottky junction on pure 2D perovskites, which is essential to carry out DLTS measurements. To overcome these issues, in this work we characterized electronic defects in 2D perovskites by means of PICTS. This technique was introduced in the ‘80s to characterize defects in CdTe and CdZnTe, in which defect characterization was limited by their high resistivity, the same as for 2D perovskites. Very recently, PICTS was used by Pecunia et al.[98] to characterize electronic defects in solar cells based on lead-free perovskite-inspired materials.

We chose PEA_2PbBr_4 as a model 2D perovskite for this study. We opted for a single crystal over a thin film, to focus only on intrinsic defects of the material, and avoid grain-boundary-related defects. Due to the extremely high resistivity of 2D MHPs in the out-of-plane direction, we were not able to extract measurable signals using a top-bottom contact geometry (i.e., with contacts on two opposite sides of the crystal). Therefore, we thermally evaporated co-planar interdigitated contacts on one surface of the single crystal, as discussed in Chapter 2. First, we electrically characterized the device in dark and under UV-light, then we moved to the PICTS investigation of defect states in the material. In addition to studying pristine samples, we also tested their X-ray radiation hardness, to observe the effect of X-ray radiation on the defect landscape of this material.

3.3.2 Electrical characterization

We first performed a characterization of the 2D perovskite device in the dark. **Figure 3.8a** shows the current-voltage (I-V) characteristics of the device, measured at different temperatures. At room temperature (dark blue curve) and below, the measured current in the investigated voltage range is below the instrumental noise of a few picoamperes. This confirms the extremely high resistivity of this material, as reported by other groups.[128,168]

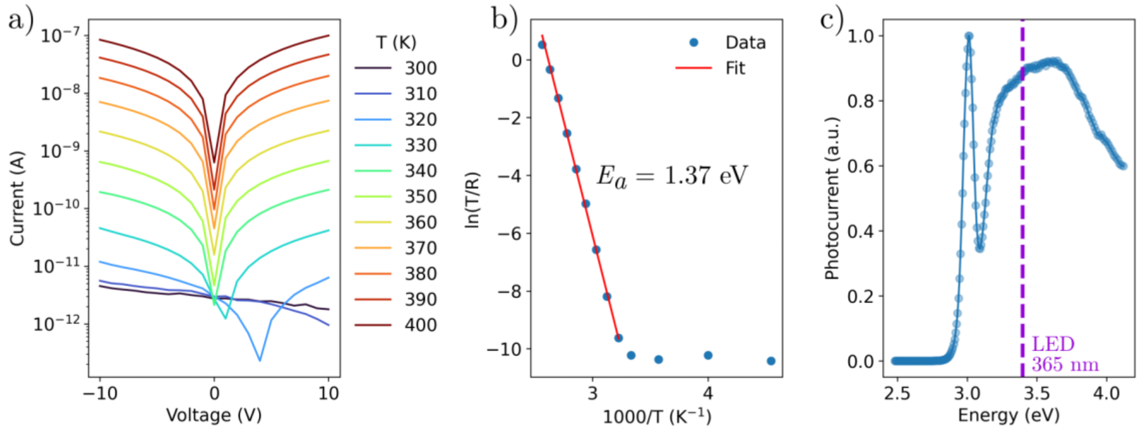

Figure 3.8 Electrical characterization of the PEA_2PbBr_4 single crystal device. **a)** I-V characteristics as a function of temperature. **b)** Nernst-Einstein fit of the resistance values obtained by linear fitting of the I-V curves in (a), the extracted activation energy for ion migration is indicated in the graph. **c)** Photocurrent spectrum of the device under 10V bias. The violet dashed line indicates the energy of the LED light used for PICTS experiments.

As the temperature increases from 300 to 400 K, the dark current increases by almost six orders of magnitude. Such behaviour has been observed for several types of both 2D and 3D perovskite materials,[64–66] and it was shown to be related to ion migration. In particular, the ionic electrical conductivity is temperature dependent via the Nernst-Einstein equation, as theoretically demonstrated by Meggiolaro et al.:[60]

$$\sigma = \frac{\sigma_0}{T} \exp\left(-\frac{E_a}{k_B T}\right) \qquad 3.6$$

where σ_0 is the conductivity at infinite temperature, and E_a is the activation energy for ion migration. This causes the exponential increase of the dark current with temperature. We extracted the resistance R as a function of temperature by linearly fitting the temperature-dependent I-V characteristics. Equation 3.6 predicts a linear behaviour of $\ln(T/R)$ as a function of T^{-1}, which is confirmed in our data, as shown in **Figure 3.8b**. We performed a linear fit in the high temperature region, which displays a linear behaviour, to extract the activation energy for ion migration in PEA_2PbBr_4. The result is 1.37 eV, which is far higher than the activation energies reported for 3D perovskites, which are typically between 0.2 and 0.8 eV.[64–66] The group of Jinsong Huang reported in various papers the absence of ion migration in quasi-2D perovskites like $BA_2MA_2Pb_3I_{10}$ (BA=butylammonium).[62,64] They based their claim on the absence of a high temperature linear activation in the Nernst-Einstein plot. However, they limited their measurements to temperatures below 300 K, where also our data show no sign of the high temperature activation. Therefore, we argue that ion migration is not fully suppressed in 2D perovskites, but it's rather hindered with respect to 3D perovskites, due to a higher activation energy. This can typically be extracted only at temperatures above 300 K.

Figure 3.8c shows the photocurrent spectrum of the sample, which was acquired with a Xenon lamp source, and with an applied bias of 10 V to the sample. The spectrum shows the typical excitonic resonance observed in the absorption spectra of low-dimensional perovskites,[172] which peaks at about 3 eV. At higher energy the onset related to band-to-band transition is visible. The light source for the PICTS measurements was a UV LED with emission centred at 365 nm. The corresponding photon energy is 3.4 eV, indicated by the violet dashed line in figure, which is well above the absorption edge of the material.

3.3.3 PICTS measurements

Intrinsic defects in PEA$_2$PbBr$_4$

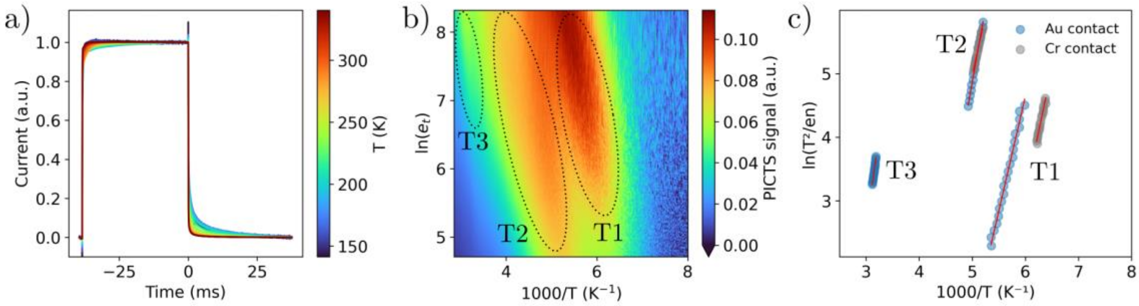

Figure 3.9 PICTS measurement on PEA$_2$PbBr$_4$. **a)** Photocurrent transients as a function of temperature, acquired with a bias of 10 V and 365 nm LED illumination. **b)** PICTS map calculated from the transients in (a). It is possible to recognize three defect signatures (surrounded by dashed lines, as guide to the eye): T1, T2, and T3. **c)** Arrhenius plots of the three defects in (b) (blue dots). The Arrhenius plots from another sample with Cr contacts are also shown as grey dots. The linear fits are represented as red solid lines.

Figure 3.9 shows the results of PICTS measurements on a PEA$_2$PbBr$_4$ single crystal with Au interdigitated electrodes. The bias applied to the sample during the measurements was 10 V (the sign of the bias is irrelevant, given the interdigitated geometry and the use of the same metal for both contacts). Given the absence of phase transitions in this material, we were able to perform the measurements in the whole temperature range available with our setup, from 78 to 400K. Due to the extremely low photocurrent signal below 140K, we discarded the measurements below this temperature, which introduced noise and did not yield any PICTS signal.

Figure 3.9a shows the photocurrent transients, which display a rise and fall time in the order of tens of milliseconds, similar to what is usually observed in semiconductors like CdTe and CZT.[86,101,102] All the photocurrent transients were normalized between 0 (dark current) and 1 (steady-state photocurrent). The PICTS map, calculated according to the procedure described in Chapter 2, is shown in **Figure 3.9b**. Three features are visible, corresponding to three defect states, labelled as T1, T2, and T3. The corresponding Arrhenius plots are reported in **Figure 3.9c** as blue dots, and the linear fits as solid red lines. To test reproducibility, we repeated these measurements on a second single crystal with interdigitated contacts made of Cr, instead of Au. The corresponding Arrhenius plots are shown in **Figure 3.9c** as grey dots. The T1 and T2 signatures are visible also in this sample, while the T3 signature is not visible, due to the convolution with the other features to be able to extract an Arrhenius plot. This confirms the good reproducibility of these measurements, as we were able to detect the same kind of defects using not only a different sample, but also a different metal contact. Reproducibility of the T1 and T2 signatures was confirmed also on other samples with Au contacts, while T3 remained somewhat elusive, being visible only in some cases. The extracted values of the activation energy and capture cross section are reported in **Table 3.2**. The three traps turn out to be relatively shallow, with activation energies between 0.3 and 0.5 eV, to be compared with the energy gap of 3.1 eV of PEA_2PbBr_4. The capture cross sections are quite large, between 10^{-12} and 10^{-14} cm^2, indicating a high trapping efficiency of these centres.

		T1	T2	T3
Au contact	E_a (eV)	0.33 ±0.05	0.40 ±0.05	0.52 ±0.08
	σ (cm^2)	$(1 \pm 0.5) \cdot 10^{-12}$	$(1.3 \pm 0.6) \cdot 10^{-13}$	$(3.4 \pm 0.6) \cdot 10^{-14}$
Cr contact	E_a (eV)	0.31 ±0.05	0.38 ±0.05	-
	σ (cm^2)	$(2.5 \pm 0.1) \cdot 10^{-13}$	$(1.4 \pm 0.4) \cdot 10^{-14}$	-

Table 3.2 Activation energy (E_a) and capture cross section (σ) of the three traps T1, T2, and T3 observed in PEA_2PbBr_4 single crystals.

Radiation tolerance of PEA_2PbBr_4

Since 2D perovskites are promising candidates for next generation ionizing radiation detectors,[128,169] we performed PICTS on the Au-contacted sample before and after high dose X-ray radiation to test its effect on the defect landscape of the material. We first performed a measurement to test the effect of aging in air, to exclude that any difference observed after X-ray irradiation was simply due to sample degradation. With this purpose, the PICTS measurements were repeated after two weeks of storage in air in the dark. The PICTS spectra for a selected rate window of 403 Hz are shown in **Figure 3.10a**. The Arrhenius plots are shown in **Figure 3.9b** with colours corresponding to the spectra. The comparison shows that the defect landscape is unchanged after two weeks of aging, as the same three features appear, with good overlap of the Arrhenius plots.

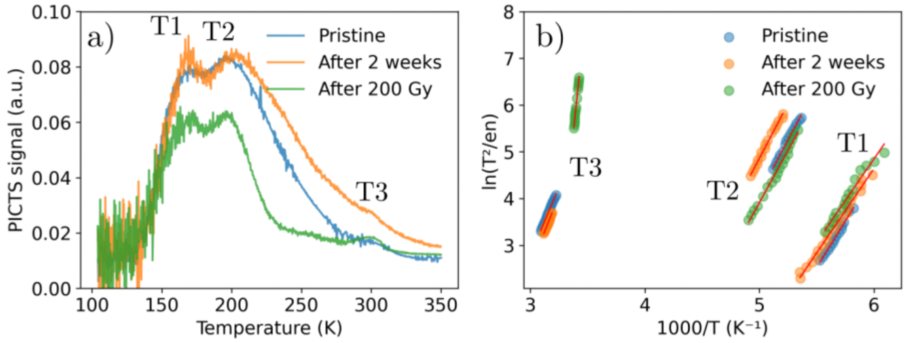

Figure 3.10 a) PICTS spectra of the Au-contacted sample at a rate window of 403 Hz, in pristine conditions (blue curve), after two weeks of aging (orange curve), and after X-ray irradiation with a 200 Gy dose (green curve). The peaks are labelled with the corresponding defect names. **b)** Arrhenius plots of the three defects. The data are shown as dots, and the linear fits as red solid lines.

		T1	T2	T3
Pristine	E_a (eV)	0.33 ±0.05	0.40 ±0.05	0.52 ±0.08
	σ (cm^2)	(1 ±0.5)$\cdot 10^{-12}$	(1.3 ±0.6) $\cdot 10^{-13}$	(3.4 ±0.6) $\cdot 10^{-14}$
After 2 weeks	E_a (eV)	0.35 ±0.05	0.38 ±0.05	0.62 ±0.08
	σ (cm^2)	(2 ±1) $\cdot 10^{-12}$	(8 ±5) $\cdot 10^{-13}$	(2.5 ±0.9) $\cdot 10^{-12}$
After 200 Gy	E_a (eV)	0.35 ±0.05	0.39 ±0.05	2.2 ±0.3
	σ (cm^2)	(3±2) $\cdot 10^{-12}$	(1.2 ±0.7)$\cdot 10^{-12}$	(2 ± 3) $\cdot 10^{12}$

Table 3.3 Activation energy (E_a) and capture cross section (σ) of the three traps T1, T2, and T3 observed in PEA_2PbBr_4 single crystals in pristine conditions, after 2 weeks of aging, and after exposure to 200 Gy X-ray dose.

The results after 200 Gy irradiation are shown in green colour in **Figure 3.10**. The extracted values of activation energy and capture cross section are reported in **Table 3.3** for the three conditions. Traps T1 and T2 remain unchanged after irradiation: the spectrum shows the peaks at the same temperatures, and the Arrhenius plots show a good overlap, as confirmed by the extracted trap parameters, while Trap T3 changes upon irradiation. Indeed, the high temperature part of the PICTS spectrum seems to be affected by ionizing radiation. The activation energy almost quadruplicates, reaching a value of 2.2 eV, and the capture cross section yields an unphysical result of 10^{12} cm^2. Such results suggest that the T3 trap after irradiation does not follow the physics of an ideal defect state, so that the Arrhenius equation that governs emission from such state does not hold. This would make meaningless the parameters extracted from the Arrhenius plot of such defect.

3.3.4 Discussion and conclusions

As discussed in Chapter 1, in 2022 M. Futscher and C. Deibel published a review paper[121] claiming that defect spectroscopy on perovskites yields ion migration parameters, rather than electronic defect parameters. Therefore, they underlined the importance of ensuring that the experimental conditions allow to exclude a relevant role of ion migration in the measurement, before claiming results on electronic defects. We note that this view is still under debate, and other groups do not agree with Futscher and Deibel, and claim that all signals observed in defect spectroscopy on perovskites are mainly related to electronic transitions.[83,92] However, we think that, given the highly mobile nature of ions in perovskites, and the long time constants of the transients often observed in defect spectroscopy on these materials (in the order of seconds, or more), it is likely that ion migration processes obscure signals from electronic transitions.

The above-mentioned debate regards solely 3D perovskites, where ion migration is known to be highly active even below room temperature. 2D perovskites are newcomers in the defect spectroscopy scenario, and this discussion has not yet been extended to this class of materials. We claim that, given the high activation energy (1.37 eV) for ion migration measured for PEA_2PbBr_4 (see **Figure 3.8b**), the signatures observed in our PICTS spectra are related to electronic defects, rather than ion migration. As will be discussed in the next section, this is probably not the case for the PICTS spectra of 3D perovskites like $MAPbBr_3$, where such activation energy is typically four times lower.

However, we note that the anomalous results obtained for the T3 signature after X-ray irradiation may be attributed to a migrating ionic specie. This result could be explained by the fact that the Arrhenius model for emission from a trap is not valid, and one should rather consider the Arrhenius model for ion migration. T3 is indeed observed in the high temperature region, where ion migration is more active. Moreover, as shown in Section 3.1, X-ray radiation can introduce ionic defects (e.g. vacancies), which may migrate in the material and give rise to ionic signals. However, these hypotheses should be tested and confirmed by further experiments.

T1 and T2 traps instead, were shown to be reproducible and to yield reliable trap parameters. Moreover, their PICTS peaks appear in a low temperature region, where ion migration is highly hindered. Therefore, we can safely assign them to electronic defect states. The large capture cross sections of T1 and T2 (10^{-12} - 10^{-13} cm^2) indicate that these defects are highly efficient trap centres, that could severely limit mobility and lifetime of the material. Indeed, devices based on 2D perovskites are currently affected by low mobility-lifetime product,[128] and trap management will be key to improve it. This work is a first step in this direction, which should be followed by the identification of the nature of these defects. This could be achieved by changing the perovskite composition during synthesis, in order to introduce on purposes excess or lack of certain elements, leading to the formation of excess interstitials or vacancies, respectively. A similar procedure has been already carried out on 3D perovskites by Deibel et al.[106]

The main result of the X-ray irradiation experiment is that X-rays do not introduce any new defect species in the material, which demonstrate a good radiation hardness of PEA_2PbBr_4. Irradiation even seems to reduce the amount of defect signatures in the spectra. Indeed, looking at the region between 220 and 270 K in **Figure 3.10**, the pristine sample shows a large tail that indicates the presence of other defect signatures, convoluted with the T1 and T2 peaks. After X-ray radiation such tail is drastically reduced, indicating a reduction in the relative concentration of such defects. Moreover, the height of the PICTS spectrum is reduced after X-ray irradiation. The relative height of the peaks is an indication of relative trap concentration, so, in theory, this indicates a reduction in the concentration of T1 and T2 of about 25% after irradiation. This information, however, should be taken with care, as calculation of trap concentration by PICTS is a delicate process, and can be affected by spurious effects not predicted by the theory.

In conclusion, in this work we performed the first ever defect characterization of a 2D perovskite sample. PICTS was proven to be an effective technique for defect characterization in high-resistivity perovskites. The technique reproducibly shows the presence of three trap states in PEA_2PbBr_4. The material also shows a good radiation hardness, as no additional defect states are observed after X-ray radiation. This work is a first step towards the identification of the defects that negatively affect mobility and lifetime in this material, paving the way for more efficient and performing 2D perovskite devices.

3.4 Photoinduced current transient spectroscopy investigation of methylammonium lead bromide single crystals

In this section, I show the results of PICTS applied to $MAPbBr_3$ 3D single crystals. To our knowledge, this is the first time PICTS was applied to a 3D perovskite material. The samples used in this study were synthesised at the Institut Néel/CEA of Grenoble, in collaboration with Julien Zaccaro, Javier Mayén Guillén, Ferdinand Lédée, Eric Gros d'Aillon, and Jean-Marie Verillhac. The PICTS characterization was carried out at the Department of Physics and Astronomy of Bologna. A manuscript with the results contained in this section is currently in preparation and will be submitted for publication in a peer-reviewed journal.

3.4.1 Introduction

As opposed to 2D metal halide perovskites (MHPs), the literature on defect spectroscopy on their 3-dimensional (3D) counterparts ($MAPbI_3$, $MAPbBr_3$, and others) is already vast. The reason lays in the large interest of the scientific community on these materials, which proved to be excellent active layers in solar cells and detectors. The most powerful defect spectroscopy technique that was applied to characterize MHPs is Deep Level Transient Spectroscopy (DLTS), which was described in Chapter 1. As already discussed in Chapter 1 and in Section 3.3, recent studies [61,106,121] have shown that when such technique is applied to mixed electronic-ionic conductors such as MHPs, ion migration processes dominate over electronic ones. The technique is then referred to as Transient Ion Drift (TID), rather than DLTS, and the output parameters of the technique are the activation energy and diffusion coefficient of mobile ionic species. The same reasoning can be applied to Thermal Admittance Spectroscopy (TAS), which was also widely adopted to characterize defect states in MHPs.[83,92,108] As already mentioned in the previous section, this interpretation is still under debate, and several research groups claim that the signatures of defect spectroscopy techniques like DLTS or TAS are related to electronic defects, and not to ion migration phenomena.[83,92]

Up to now, the above-mentioned debate has concerned almost exclusively voltage-modulated techniques like DLTS and TAS, which are typically carried out in the dark. Although Futscher and Deibel[121] mentioned light-modulated techniques like PICTS among the ones where electronic phenomena might be obscured by ionic ones, they did not go into the details of how light modulation can induce ionic motion, and neither on how ion migration parameters can be extracted by such techniques.

We note that light-modulated defect spectroscopy is of particular interest for materials like MHPs, whose main application is in optoelectronic devices, as it allows to probe defects under working conditions, i.e., under exposure to light. Up to now, no PICTS characterization of 3D MHP can be found in literature. Recently, Pecunia et al.[98] reported a PICTS characterization on perovskite-inspired materials like $AgBiI_4$, $Cs_3Sb_2I_9$, and others. However, this work interpreted all signatures measured by PICTS as electronic defects, and was recently accused by Futscher and Deibel[121] of not delivering any evidence that the nature of such signatures is electronic, rather than ionic.

In this work, we performed the first PICTS measurements on a 3D MHP. As model 3D MHP samples, we chose $MAPbBr_3$ single crystals. The use of single crystals allows to exclude contributions from grain boundaries and other defects that are present in polycrystalline samples, to focus solely on the intrinsic material's properties. The crystals were contacted in a top-bottom geometry with Cr contacts, as shown in Chapter 2. Cr was shown to be a chemically stable contact for $MAPbBr_3$, as it naturally forms a chromium oxide (CrO_x) layer during the thermal evaporation, which acts as a passivation layer that hinders reaction of the Cr metal with the perovskite.[132] This is essential for reliable and reproducible measurements, given the high reactivity of 3D MHPs with metals, even noble ones, such as Au.[173,174] We first performed basic opto-electronic measurements to discuss the impact of ion migration on PICTS measurements. We found that, as opposed to the 2D perovskite PEA_2PbBr_4, the PICTS signals in $MAPbBr_3$ are likely dominated by ions movement, rather than electronic trap states. We thus develop a model to explain how light modulation of the current in a MHP can result in characteristic signatures of ionic motion.

3.4.2 Optoelectronic characterization

Figure 3.11 shows the optoelectronic characterization of MAPbBr$_3$ single crystal devices. **Figure 3.11a** shows the current-voltage (I-V) characteristics in dark and under 3 mW/cm^2 475 nm blue LED light, measured in air and at ambient temperature. In the lower left corner, the device structure is schematized: the bottom contact is connected to ground, the voltage is referred to the top contact, and light reaches the device through the top contact. In the dark, the device shows good Ohmic behaviour, as already reported for other Cr-contacted MAPbBr$_3$ devices.[132,175,176]

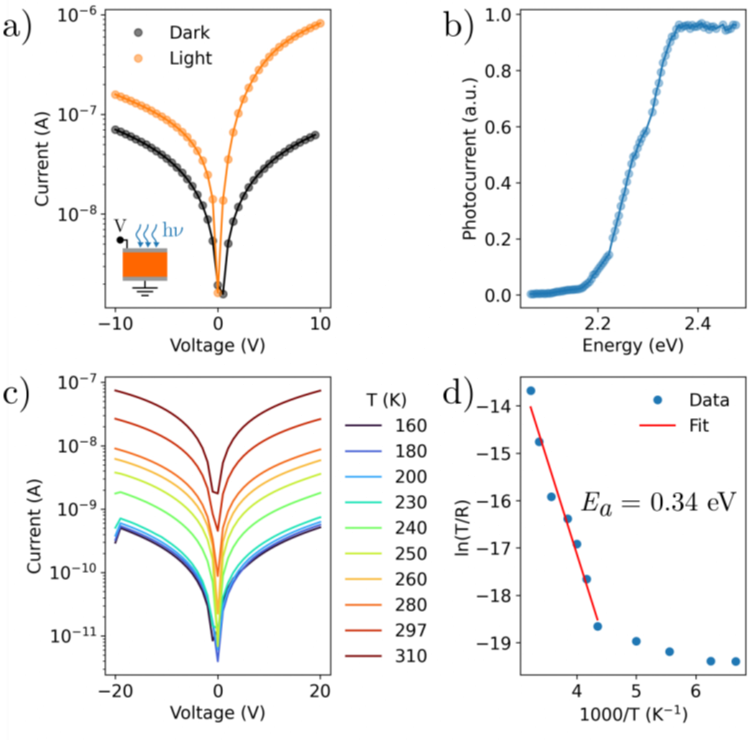

Figure 3.11 Optoelectronic characterization of MAPbBr$_3$ single crystal devices. **a)** I-V curve of a device in dark, and under 3 mW/cm^2 blue light. The sample geometry is schematized in the lower left corner. **b)** Photocurrent spectrum acquired at +5V using a Xenon lamp as light source. **c)** Temperature-dependent I-V curves measured between 160 K and 310 K. **d)** Nernst-Einstein fit of the resistance values obtained by linear fitting of the I-V curves in (c), the extracted activation energy for ion migration is indicated in the graph.

The resistivity of our devices, calculated by linearly fitting the dark current, is reproducibly in the range of 1-5 · 10^8 Ωcm, in line with the results of other groups on the same material.[177] Under light, the I-V becomes asymmetric, with the current at +10 V almost one order of magnitude higher than the one at -10 V. This can be understood by considering both the specific geometry used for these measurements, and intrinsic transport properties of this material. The

475 nm blue LED light is high above the bandgap of $MAPbBr_3$, which is around 2.3 eV (539 nm) as confirmed by the photocurrent spectrum in **Figure 3.11b**. The absorption coefficient of the material at this wavelength is around 10^5 cm^{-1},[42] corresponding to an absorption depth of around 200 nm. This means that the light-induced electron-hole pairs are generated in a layer close to the top contact, which is much thinner (200 nm) than the crystal depth (1 mm). It is known that in $MAPbBr_3$ the mobility-lifetime product of holes is much higher than that of electrons ($\mu_h \tau_h \gg \mu_e \tau_e$).[175] When a positive bias is applied at the top contact, electrons are promptly collected at the top electrode, while holes are injected in the bulk and collected at the bottom contact. Upon negative bias, holes are collected at the top, while a significant fraction of the electrons cannot reach the bottom contact due to their low $\mu\tau$, explaining the lower photocurrent under negative bias.

Figure 3.11c shows the temperature-dependent I-V curves in the dark measured between 160 K and 310 K. As for PEA_2PbBr_4 (Section 3.3.2), a thermal activated conductivity is observed above a critical temperature, in this case at 200 K. According to the procedure described in Section 3.3.2, we performed a Nernst-Einstein fit of the high temperature region of the resistance as a function of temperature, to assess the activation energy for ion migration, which we measured to be 0.34 eV. This is in perfect agreement with similar measurements performed on $MAPbBr_3$ by other research groups.[67,178] We note that this value is four times lower than the activation energy of 1.37 eV measured for the 2D perovskite PEA_2PbBr_4. This indicates that ion migration is much more active in this material, and a relevant ionic contribution to the transport properties is expected in $MAPbBr_3$ in the investigated temperature range, as opposed to PEA_2PbBr_4. For this reason, and for others that will be discussed in the following, we assign the signatures measured by PICTS on $MAPbBr_3$ to ion migration phenomena.

3.4.3 PICTS measurements

PICTS measurements were performed using 475 nm blue LED excitation in the temperature range 250-380 K. The lower limit of 250 K was chosen to avoid the cubic to tetragonal phase transition that $MAPbBr_3$ undergoes at 240 K.[25] Indeed, we found that performing measurements below this temperature can produce artefacts in the PICTS spectra. Measurements were performed at both positive and negative voltages (the convention for the voltage sign is the one illustrated in the inset of **Figure 3.11a**).

In classical PICTS theory, the change of bias voltage allows to distinguish between hole and electron traps. With positive voltage, holes are injected in the bulk and they have a much higher probability of getting trapped with respect to electrons, which are promptly collected at the top contact. Therefore, the PICTS signatures measured at positive bias are assigned to hole traps. The opposite reasoning goes for electrons, whose traps are investigated applying a negative bias.[104] This model cannot be applied in the same manner for $MAPbBr_3$, and 3D perovskites in general, because ion migration plays a significant role in shaping the photocurrent transients, and masks hole and electron trap contributions to the signals. Nonetheless, we found completely different PICTS spectra for positive and negative biases, and in the following we will discuss how to interpret this in terms of ion migration phenomena.

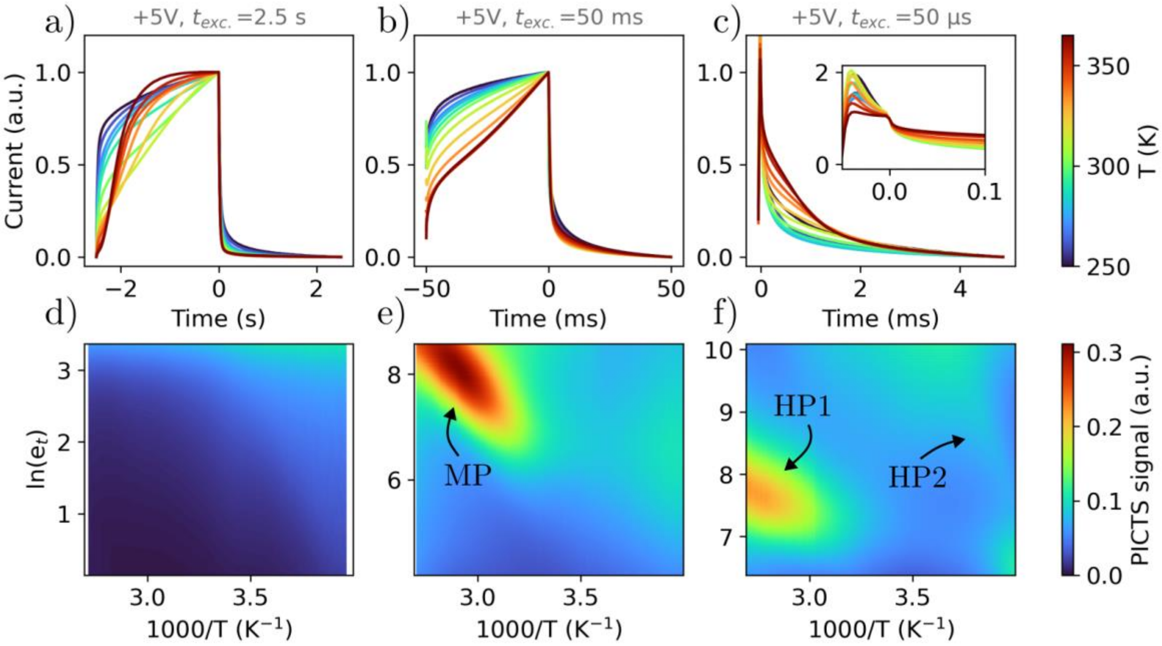

Figure 3.12 PICTS measurements on $MAPbBr_3$ devices at +5 V. Photocurrent transients measured with excitation time of **(a)** 2.5 s, **(b)** 50 ms, and **(c)** 50 μs. All current values are normalized between 0 (dark current) and 1 (current at the time when light is turned off). The PICTS maps are shown below the corresponding transients, in **(d)**, **(e)**, and **(f)**. On the maps are indicated the identified signatures, labelled as MP (Medium-frequency, Positive voltage), and HP (High-frequency, Positive voltage).

Figure 3.12 shows the photocurrent transients measured at positive voltage (+5 V) in the top row, and, in the bottom row, the corresponding PICTS maps calculated from the transients. All the current values in the transients are normalized between 0 (dark current) and 1 (current at the time when light is turned off). We found a profound difference between the photocurrent transients measured in $MAPbBr_3$, with respect to PEA_2PbBr_4. While the latter showed rise and fall times in the ms range (see **Figure 3.9a**), as typically observed in inorganic semiconductors like CdTe,[179] $MAPbBr_3$ shows slower transients, in the range of seconds. This is shown in the transients in **Figure 3.12a**, where a 2.5 s light excitation time was used. We will refer to these transients as *low-frequency* (LF) transients. Such slow response has been reported by several groups on 3D perovskites, although its nature is often not discussed.[177,180,181] In the transients of **Figure 3.12a**, the rise signal is slower than the fall signal, which is another peculiarity that differs from what is expected from purely electronic signals. Indeed, the rise time is expected to be faster, or at most equal, to the fall time, since it is related to capture processes, which are faster than emission processes.[86,121] We consider such unusual asymmetry in the rise and fall times, and the slow nature of the transients to be other indications that the PICTS signals are dominated by slow-moving species, i.e. migrating ions, rather than electronic defects. **Figure 3.12d** shows the PICTS map calculated from the transients in **Figure 3.12a**. No PICTS signature is detected in this case.

We noticed that the shape of the transients drastically changes upon modifying the excitation time. **Figure 3.12b** shows a photocurrent transient measured at +5 V, and with a 50 ms excitation time, thus decreasing the excitation time by almost two orders of magnitude. We will refer to these transients as *medium-frequency* (MF) transients. The result is a faster response of the material with respect to what is observed using a slower excitation time. For example, in the MF transient at 250 K the signal under light almost reaches a steady state during the 50 ms illumination time. At the same temperature, in the LF transient the signal takes the whole 2.5 s illumination time to get close to a steady state condition. This indicates the presence of slow phenomena that take place only if light excites the sample for a long enough time. Looking at the MF transients, it is evident how, upon increasing temperature, a new component in the rise signal arises (see for example the dark red curve at 380 K), which is probably the same phenomenon that is fully captured in the LF transients. The fact that these slow phenomena are thermally activated in such high temperature region is another hint of their ionic character. The PICTS analysis of the MF transients yields the map in **Figure 3.12e**, where a clear signature appears, labelled as MP (Medium-frequency, Positive bias).

In the attempt to characterize fast electronic trapping phenomena, we tried an even faster excitation time of 50 µs, i.e., three orders of magnitude faster than the MF measurements. The resulting transients are shown in **Figure 3.12e**, and will be referred to as *high-frequency* (HF) transients. We found again that the response time drastically changes upon changing the excitation time: as shown in the inset, the device shows a response time in the order of tens of μs if a 50 μs light pulse is used as excitation. Despite such fast rise time, we found the decay time to be two orders of magnitudes slower, so that we were forced to use a 1% duty cycle to allow the decay transient to reach the steady state. **Figure 3.12f** shows the corresponding PICTS map, which displays two signatures, one at high temperature (HP1), and one at low temperature (HP2) (HP stands for High-frequency, Positive bias). The fast nature of these signals might suggest their electronic nature. This aspect will be discussed in the following, with a comparison with literature results on other 3D perovskites. As a final remark on the PICTS measurements at positive voltages, we note that the strategy of varying the excitation time allowed to investigate a frequency space of 5 orders of magnitude, with 0.14 Hz $< \ln(e_t) < 10.1$ Hz (see the y-axis in the three PICTS maps).

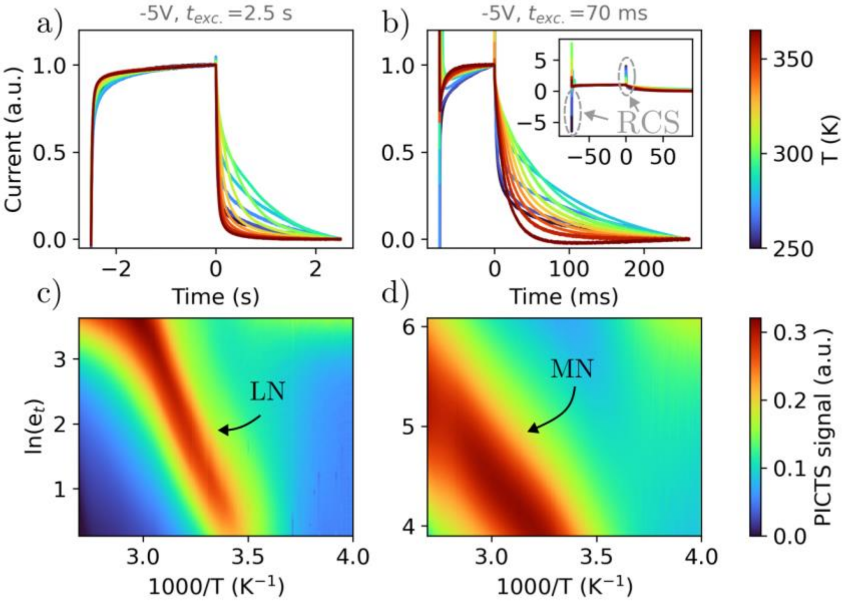

Figure 3.13 PICTS measurements on $MAPbBr_3$ devices at -5V. Photocurrent transients measured with excitation time of **(a)** 2.5 s, **(b)** 70 ms. All the current values are normalized between 0 (dark current) and 1 (current at the time when light is turned off). The inset in (b) shows the transients at full scale, and dashed grey circles indicate the reverse current spikes (RCS). The PICTS maps are shown below the corresponding transients, in **(c)**, and **(d)**. On the maps are indicated the identified signatures, labelled as LN (Low-frequency, Negative voltage), and MN (Medium-frequency, Negative voltage).

We repeated PICTS measurements with a negative -5 V bias, and the results are reported in **Figure 3.13**. Also in this case, the transients are normalized between 0 and 1, although the current direction in this case is opposite to the case of positive bias. Again, we observed a slow response at the slow excitation time of 2.5 s, as shown in **Figure 3.13a** (LF transients). However, with this polarity, the rise time is faster than the fall time, as opposed to the case of positive polarity. The LF transient analysis yields the PICTS map in **Figure 3.13c**, where a signature, labelled as LN (Low-frequency, Negative voltage), is clearly visible. Upon decreasing the excitation time to 70 ms, we measured the MF transients in **Figure 3.13b**. Again, as for positive voltage, a faster excitation time leads to a faster response time of the sample, which reaches a steady state after 70 ms for almost all temperatures. The slower de-excitation time forced us to decrease the duty cycle to allow the system to reach a steady state in the dark. The corresponding MF PICTS map is shown in **Figure 3.13d**, where another signature, named MN (Medium-frequency, Negative voltage), is clearly present.

All measurements at negative voltages show peculiar *reverse current spikes* (RCS), that are indicated in the inset of **Figure 3.13b**. By this term, we indicate the fast current spikes (with duration in the order of µs) that occur when light is turned both on and off, and that have opposite sign with respect to what is expected, given the sign of the bias. When light is turned on, the current first shows a large negative spike, and then reaches positive values, forming the rise transient. When light is turned off, a large positive spike occurs, higher than the steady state photocurrent, and then the decay transient is observed. In the MF transients, the RCSs are clear because they are than 5 times higher than the steady-state photocurrent signal. However, they can also be observed in the LF transients, where they are more hidden by the higher photocurrent at low frequencies. This effect did not allow us to measure the HF transients at negative bias. Indeed, this effect makes impossible to characterize photocurrent transients at high frequencies, since the RCS features overlap with the rise and decay photocurrent signals. The cause of the RSC features and its implications in the interpretation of the PICTS signal in an ionic framework will be discussed in the following section. We note that the RCS features may be due to electrical cross-talk between the LED circuit and the sample circuit. We rejected this possibility by observing that no RCS are visible if a black absorber is inserted between LED and sample, demonstrating that the RCS comes from a process that is internal to the sample.

Figure 3.14 shows as solid-colour dots all the PICTS signals reported in the maps above in a single Arrhenius plot, with labels indicating the name of each signature. On top of them, we overlay as semi-transparent colours the signatures measured by Reichert et al.[106] on $MAPbI_3$ solar cells, using DLTS. Their assignment of these signatures is to ionic species, that they distinguish in three families β, γ, and δ. The reason why several Arrhenius plots are shown for each family, is that each one corresponds to different stoichiometries of $MAPbI_3$, with excess methylammonium, or excess iodine. In this work, they show compelling evidence that their

DLTS signatures data are related to ion migration, rather than electronic traps. They also show that these data show a good overlap with trap signatures measured with DLTS or TAS by several other groups on MHP materials, including $MAPbBr_3$, and $FAPbI_3$. Thus, they suggest that virtually all trap signatures measured by defect spectroscopy reported in literature are related to ion migration, rather than electronic defects. Given the good overlap of our data with theirs, we consider this a further indication that the PICTS signals measured on $MAPbBr_3$ should be assigned to migrating ions.

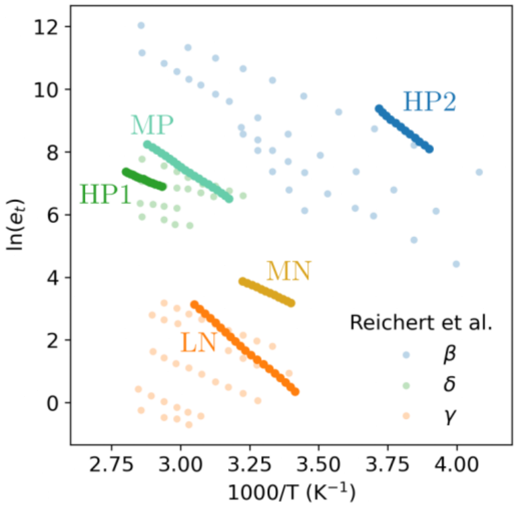

Figure 3.14 Arrhenius plots of all PICTS signatures measured on $MAPbBr_3$ single crystals (solid-colour dots). Each signature is labelled using the naming convention introduced above. The curves are overlapped with ion migration signatures measured by Reichert et al.[106] on $MAPbI_3$ solar cells using TID (semi-transparent dots). Reichert et al. labelled the families of signatures by the Greek letters β, γ, and δ. Given the ionic interpretation of our data, e_t represents an ion migration rate, rather than an electron/hole emission rate from traps.

In particular, LN is found in the same Arrhenius space as γ, HP1 and MP overlap with δ, and HP2 with β. Given the vicinity of HP1 and MP in the Arrhenius space, we propose that they might be related to the same ionic species. The only signature not overlapping with β, γ, and δ is MN, which might represent a different kind of migrating species, not reported by Reichert et al. We also note that there is good agreement with the expected charge of these ionic species. β and δ are observed as positive peaks in TID, which thus indicates they are negatively charged ions, given the p-type conductivity of $MAPbI_3$. γ, instead, is assigned to positively charged ions. Similarly, MP, HP1, and HP2 were all measured applying a positive bias to the top contact, which, as will be discussed in the following section, attracts negative ions and allows to characterize them. LN was instead measured under negative bias, and thus is related to positive ions. Our signatures generally show higher slope of the Arrhenius lines, indicating a higher activation energy for ion migration. We assign this to hindered ion migration in our single crystals, with respect to the polycrystalline samples of Reichert et al. Indeed, ion migration is known to be enhanced in presence of grain boundaries.[66]

Therefore, we assign all PICTS signatures we measured on $MAPbBr_3$ to ion migration, and thus the e_t values plotted on the vertical axis of the Arrhenius plot should be regarded as *migration rates*, rather than emission rates. We note, however, that the similarities found between PICTS and DLTS/TID are not straightforward to understand, given the totally different nature of the two techniques. PICTS measures light-induced current transients, while DLTS measures voltage-induced capacitance transients in the dark. Thus, they differ in both the probe and the measured physical quantity. In the following sections we discuss a model to understand how PICTS can probe ion migration phenomena, and how to extract quantitative ion migration parameters from such measurements. A similar modelling was developed for TID in the 90's, to explain how DLTS measurements could characterize ion movement in semiconductors containing mobile ionic impurities.[112,113]

3.4.4 Interpretation of PICTS results in terms of ion movement

The development of this model starts from two assumptions, both backed up by literature results. The first one is that the current transients measured by PICTS on $MAPbBr_3$ cannot be related to ionic currents flowing from one electrode to the other. The distance between our electrodes is approximately d =1 mm. We can consider an average ionic diffusion coefficient $D = 10^{-8}$ cm^2/s, in line with reported values in literature.[132,182] Using Einstein's relation, we can extract the ion mobility ($\mu = eD/k_BT$), which is related to the ion drift velocity (v) by $v = \mu E = \mu V/d$, where E is the electric field, and V is the applied voltage. From these considerations, one can easily find that the time needed for an ion to travel the whole d =1 mm distance in the crystal is approximately 10^3 seconds, which is orders of magnitude higher than the maximum probed time of 2.5 seconds in our transients. The second assumption is that the electronic conductivity in halide perovskites is orders of magnitude larger than the ionic one. This assumption is also supported by literature results.[58,132,183] This means that the current measured by PICTS can be considered as a purely electronic current, with negligible ionic contribution.

Our model is mainly discussed in terms of energy band diagrams, and it is schematized in **Figure 3.15**. The band diagram of the device in the dark and with no applied bias is shown in **Figure 3.15a**. We base our interpretation on the presence of a downward band bending at the $MAPbBr_3/CrO_x$ interface, due to positive ion accumulation at the contacts. In this model we will assume these ions to be fixed (i.e., not mobile), for simplicity. Such downward band bending causes the presence of a space charge region (SCR) at the perovskite/electrode interface. The existence of such native band bending is supported by literature results on both photocurrent and contact potential mapping of $MAPbBr_3$ devices.[184,185] Its existence is also confirmed in our measurements by the RCS we observed at negative bias, as will be discussed in the following.

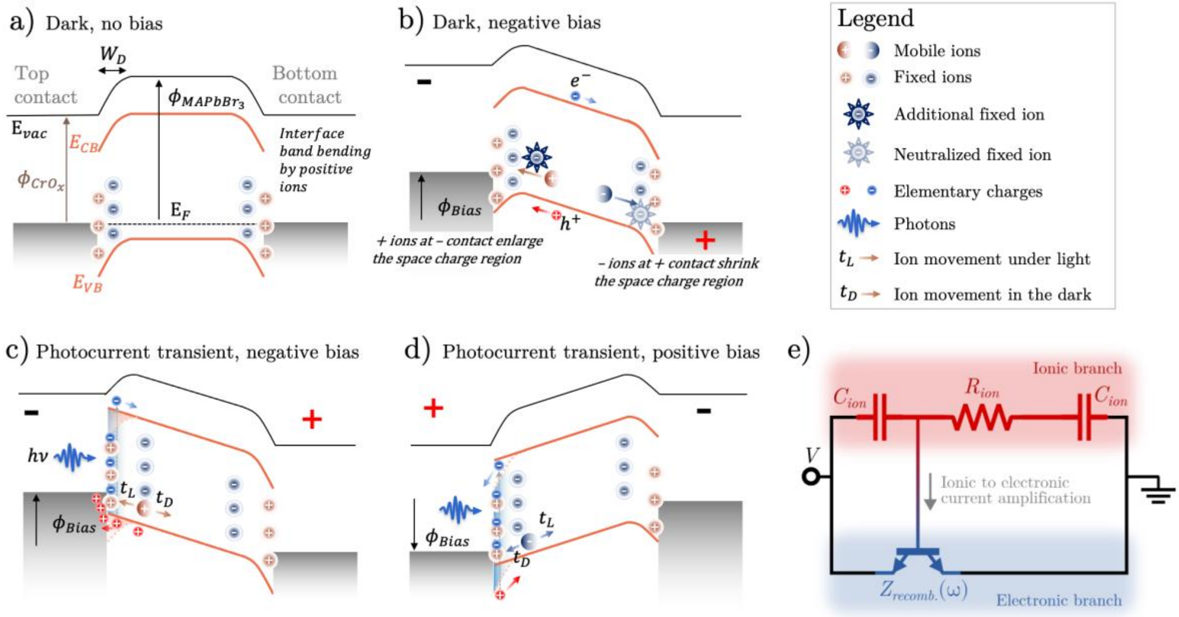

Figure 3.15 Model for interpretation of PICTS signatures in terms of ion migration. **a)** Band diagram in the dark and with no applied bias of the CrO_x-$MAPbBr_3$-CrO_x device. E_{vac} is the vacuum level energy, ϕ represents work function values, W_D is the depletion layer width, E_F is the fermi energy, E_{CB} and E_{VB} are the conduction band and valence band edges, respectively. **b)** Band diagram in the dark with negative applied bias. **c-d)** Band diagram during photocurrent transient measurements under negative and positive bias. The dashed bands represent the dark condition. The solid ones represent the situation under light. Arrows labelled t_L and t_D represent ion movement under light and in dark, respectively. **e)** Electrical scheme modelling how ion movement affects electronic conduction, based on the work of Moia et al.[186]

Figure 3.15b shows the band diagram in the dark, when a negative voltage is applied to the top contact. Holes and positive mobile ions move towards the negative contact, and electrons and negative ions towards the positive one. One should expect a non-Ohmic behaviour of a device with a SCR at the semiconductor/metal interface, which instead is not observed in our device. However, if such barrier is low enough or thin enough, an Ohmic behaviour can be observed by thermionic emission or tunnelling of charge carriers. Indeed, Shrestha et al. observed an Ohmic behaviour in their Au/$MAPbI_3$/Au and Au/$MAPbBr_3$/Au devices, despite directly observing the presence of a SCR at the MHP/metal interface via photocurrent mapping. While elementary charges are collected at the electrodes, ions can only accumulate at the perovskite-metal interface, thus modifying the band bending. Mobile positive ions bring further positive charge to the top contact, enlarging the SCR. On the contrary, at the bottom contact, negative ions shrink the SCR. If a positive bias is applied, the opposite process occurs.

Figure 3.15c shows the band diagram during the photocurrent transient measurements with negative bias. Above-band gap photons induce electron-hole pairs in the first 200-300 nm of the perovskite layer. Due to the downward band bending, photogenerated electrons initially are not collected at the positive electrode, but are confined at the top electrode interface, where they get trapped by the fixed positive ions. The negative charge of the localized electrons is screened by holes attracted from the external circuit to the top contact/perovskite interface. Such movement of holes in the circuit (in opposite direction to what is expected, given the sign of the bias) causes the reverse current spike (RCS) observed in our measurements when light is turned on (see inset of **Figure 3.13b**). Photogenerated electrons compensate fixed ions by removing the band bending, create flat band condition at the top contact, and flow towards the positive electrode, generating the photocurrent. The positive mobile ions accumulated at the top contact move in response to such light-induced change in band bending. Since the slope of the band changes from positive to negative, they are accelerated towards the top contact (arrow labelled as t_L in figure). When light is turned off, the trapped electrons at the interface are thermally released from their traps, and the corresponding screening holes flow in the external circuit in the opposite direction, yielding the RCS observed upon turning off the light (see inset of **Figure 3.13b**). Thus, the RCS are, in fact, photo-capacitive peaks related to electron trapping at the interface. The immobile positive ions at the interface are no more neutralized, and the band goes back to the downward bending condition. Therefore, the mobile positive ions are pulled back towards the bulk in response to this local change in the band (labelled as t_D in figure). In short, under negative bias, light induces changes in the band bending via photo-generated electrons, and positive ions migrate in response to such change. When light is turned off, the band bending is recovered, and ions go back to their initial position.

Figure 3.15d shows the band diagram during the photocurrent transient measurements with positive bias. In this case, no RCS are expected, as electrons naturally flow towards the top contact. Indeed, no RCS are observed in the measurements under positive voltage (see **Figure 3.12**). With this polarity, negatively charged mobile ions accumulate at the top contact. Also in this case, a fraction of the photo-electrons are trapped at the interface, and modulate the band bending, causing movement of the negative mobile ions. In this case, when light is turned on, the negative ions move towards the bulk (labelled as t_L in figure), and when light is turned off, they move towards the interface (labelled as t_D in figure).

As discussed at the beginning of this section, the measured photocurrent in $MAPbBr_3$ should *not* be regarded as an ionic current. Therefore, we can consider the measured current in these PICTS measurements to be purely electronic. Thus, the question arises: how can an electronic current show characteristic times of ion migration phenomena? This theme is vastly discussed in the literature. It is known that, although most of the current in halide perovskites is electronic, ions have a large power of modulating it. The most common example is the hysteretic behaviour of perovskite solar cells, which is due to ion migration in the perovskite layer.[13,187] Garcìa-Batlle et al. showed that moving ions cause doping in $MAPbBr_3$ single crystals, thus greatly affecting their electronic response.[132] Pockett et al. proposed that the low-frequency features observed in voltage- and light-modulated impedance spectroscopies (IS) on hybrid perovskites are not related to an ionic impedance, but to electronic carriers whose recombination impedance (Z_{rec}) is modulated by migrating ions. This model was further developed by Moia et al.,[186] to better understand the link between ionic and electronic movement. They found that their results of IS in dark and under illumination could be explained using the circuit model shown in **Figure 3.15e**. The upper branch of the circuit represents the ionic contribution, which is characterized by two capacitors at the two contact interfaces (C_{ion}), and a bulk ionic resistance (R_{ion}). The lower branch represents the electronic contribution, which is modelled by the electronic recombination impedance (Z_{rec}) (typically, a recombination resistance and capacitance in parallel). They found that Z_{rec} can be modelled as a bipolar transistor whose gate is controlled by the ionic circuit branch. This means that ion movement can amplify the current that flows in the electronic circuit branch. Note that Z_{rec} is frequency-dependent, and the frequency can be modulated by slowly-moving ionic species. Here, we adopt this model to explain how the photocurrent in PICTS measurement can yield ion migration parameters. Moving ions in the SCR close to the top contact cause a slow amplification of the electronic photocurrent, which, in turn, yields parameters that belong to the migrating ions themselves, hindering the ones of the electronic carriers.

3.4.5 Extraction of ion migration parameters

From the above-discussed band diagram model, we now extract equations that describe the light induced ionic motion in at the SCR near the top contact. These will allow to extract ion migration parameters from PICTS measurements.

When light is modulated, ions move of a distance equal to the SCR width W_D, represented in **Figure 3.15a** with a characteristic time τ that is different for each ionic species. The migration rate e_t, which is the reciprocal of τ, can be described as:

$$e_t = \frac{1}{\tau} = \frac{v_{ion}}{W_D} = \frac{\mu_{ion}E}{W_D} = \frac{eD_{ion}E}{W_D k_B T} \qquad 3.7$$

Where v_{ion} and μ_{ion} are the ionic drift velocity and mobility. In the last passage we used Einstein's relation. The diffusion coefficient is exponentially dependent on temperature according to $D_{ion} = D_0 \exp(-E_a/k_B T)$,[61,106,113] where D_0 represents the diffusion coefficient at infinite temperature, and E_a is the migration activation energy of the ionic specie. Thus, the migration rate can be expressed as

$$e_t = \frac{eE}{W_D k_B T} D_0 \exp\left(-\frac{E_a}{k_B T}\right) \qquad 3.8$$

This equation describes the Arrhenius behaviour of migrating ions inside a depletion region, already applied in the ionic description of DLTS (i.e., TID).[61,106,113] It allows to link the experimentally determined rate window e_t, i.e. the migration rate, to the underlying ion migration parameters, i.e., E_a and D_0. These can be found by the slope and intercept of the linear fit of $\ln(e_t T)$ as a function of T^{-1}. In the TID theory, Equation 3.8 is further developed, expressing the electric field in the depletion region as a function of the doping concentration. The latter can be estimated by performing a Mott-Schottky analysis of the capacitance-voltage curve of the junction under study. Since in our case the device is Ohmic, rather than a rectifying junction, this analysis cannot be performed. Therefore, we leave Equation 3.8 in this form, and we provide an estimation of E and W_D based on literature results. As an estimation of E, we consider the value of 0.3 V/µm measured by Ahmadi et al.[185] at the $MAPbBr_3$/metal interface using kelvin probe force microscopy. We then estimate a value of $W_D = 1$ µm, based on the results of Ahmadi et al., and also Shrestha et al.,[184] who characterized the band bending at the perovskite/metal interface for both $MAPbI_3$, and $MAPbBr_3$. In **Table 3.4** we report the values of activation energy and diffusion coefficient at room temperature (D_{300K}) extracted by the Arrhenius plots of **Figure 3.14**, applying the above-described model. We note that D_{300K} is affected by the values of E and W_D, which we chose based on results by other research groups, so they should be considered as a rough estimation. Specific measurements of the band bending at the $MAPbBr_3$/metal interface of our samples would be needed to confirm these values. The activation energy values are instead independent of E and W_D, so they can be considered as reliable.

Name	E_a **(eV)**	D_{300K} **(cm²/s)**	**Assignment**
LN	0.67±0.03	(2.3±0.2)· 10^{-9}	MA_i^+
MN	0.37±0.018	(2.7±0.3)· 10^{-8}	V_{Br}^+
MP	0.53±0.03	(2.3±0.2)· 10^{-7}	Br_i^-
HP1	0.34±0.017	(1.9±0.2)· 10^{-7}	Br_i^-
HP2	0.62±0.03	(1.4±0.1)· 10^{-5}	V_{MA}^-/electronic

Table 3.4 Activation energy and diffusion coefficient at room temperature of the ionic species identified by PICTS measurements of $MAPbBr_3$ single crystals. The diffusion coefficient values are obtained assuming $E = 0.3$ V/µm, and $W_D = 1$ µm. In the last column are reported our tentative assignments of the PICTS signatures with ionic migrating species.

3.4.6 Discussion and conclusions

The activation energies obtained by our PICTS measurements fall within the range of activation energies for ion migration reported by several groups on a wide range of MHP materials, between 0.2 and 0.7 eV.[59,61,98,106,108,116] We note that the lowest values of activation energies measured by PICTS well overlap with the 0.34 eV activation energy extracted by the temperature dependence of the conductivity (see **Figure 3.11d**). This agreement confirms the consistency of our results. Indeed, it is likely that conductivity versus temperature measurements, which are not able to discriminate among different ionic species, provide parameters of the ions that most easily migrate in the material, i.e. the ones with lowest activation energy.

Also the estimated diffusion coefficient values fall within the range of the ones reported in the literature.[106,182,183,188] In particular, LN, MN, MP, and HP1 fall in the range between 10^{-7} and 10^{-9} cm²/s reported in the papers of Garcìa-Batlle et al. on $MAPbBr_3$ single crystals.[132,176] The only result in contrast with values reported in literature is HP2, which, in our model, yields a diffusion coefficient higher than 10^{-5} cm^2/s. Such high diffusivity was never reported in literature for ionic species in MHPs. This suggests that HP2 might be related to an electronic trap, rather than a migrating ion species. However, we note that this hypothesis should be taken with caution, since, as discussed previously, the diffusivity values here reported have to be considered as a rough estimation.

We now provide a tentative assignment of the reported signatures to migrating ionic species in $MAPbBr_3$. As discussed in previous sections, we assign signatures measured with negative bias to positively charged ions, and features measured with positive bias to negatively charged ones. Therefore, LN and MN should correspond to positively charges species. The most mobile charged ionic species in MHPs are MA_i^+, and V_{Br}^+,[89,111,189] i.e., methylammonium interstitials and bromine vacancies, while Pb_i^{2+} is expected to be rather immobile in the lattice.[59] Reichert et al. assigned the γ signature to MA_i^+,[106] and, given the good overlap of LN with γ shown in **Figure 3.14**, we assign LN to this ionic specie. We associate the higher activation energy that we measured with respect to the one reported for γ to the absence of grain boundaries in our single crystalline samples. By exclusion, we assign MN to V_{Br}^+ migration. Given the vicinity of MP and HP1 in the Arrhenius space, we assign them to the same negatively charged ionic specie. Given the good overlap with the δ signature of Reichert et al., which was assigned to halide interstitials,[106] we assign them to Br_i^- migration. The difference in activation energy of around 0.2 eV between MP and HP1 might be related to the presence of the second HP2 signature in the high frequency PICTS map. Indeed, the presence of several features in the spectra can lead to convolutions between the peaks, that mask the real activation energy of the underlying phenomena. The HP2 feature shows a good overlap with the β signature of Reichert et al., which was assigned to V_{MA}^-, in good agreement with the negative charge expected for this defect. However, as discussed above, the estimated diffusion coefficient of HP2 is not compatible with an ionic migrating specie. Therefore, this signature needs further investigation to certainly assess its nature. The last column of **Table 3.4** summarizes the assignments just described.

It is important to note the difficulty of assigning signatures from defect spectroscopy to the underlying ionic migrating specie. This task has proven to be difficult not only by the experimental difficulty of these measurements, but also to the intrinsically complicated nature of ion migration in MHPs. As an example, as discussed above, Reichert et al.[106], assigned the β ionic specie to V_{MA}^-,[106] but recently the same group re-assigned it to V_I^+,[190] thus changing not only the moving chemical specie, but also its charge. However, β was also observed by the same group in MHPs without iodine, like $CsFAPbBr_{1-x}Cl_x$,[108] and, on the other hand, it was *not* observed in a iodine-based MHP like $FAPbI_3$.[107] This exemplifies how difficult is the task of assigning defect spectroscopy signatures to their related ionic species. Therefore, the assignments reported above should be taken with caution.

In conclusion, in this work we provided consistent evidence that PICTS characterizes ion movement in 3D MHPs like $MAPbBr_3$, rather than electron trapping. This is in contrast with 2D MHPs, as discussed in Section 3.3. We thus propose that previously published results that applied PICTS to MHP-inspired materials should be revised in view of this.[98] We found that performing PICTS at different modulation frequencies allows to access information on faster moving species, that are not accessible with low frequency measurements. We also proposed a physical model to explain how light modulation can induce photocurrent transients that show the characteristic times of ion movement. The analysis of our PICTS data based on this model provides activation energies and diffusion coefficients in agreement with those previously reported in the literature. Thus, this work proves that PICTS is a valuable technique that allows to characterize ionic parameters in MHPs, that should be used together with TID, TAS, and other defect spectroscopy techniques to investigate the complicated nature of ion migration in MHP materials.

3.5 Impact of environmental gases on the electronic and ionic properties of $MAPbBr_3$ single crystals

In this section, I show the results of the opto-electronic characterization of $MAPbBr_3$ single crystals under different environmental gases, including current-voltage characteristics and PICTS analysis. To our knowledge, this is the first time that a defect spectroscopy technique like PICTS is performed on MHP materials under atmospheres different than vacuum. The samples used in this study were synthesised in Insitut Néel/CEA of Grenoble, in collaboration with Julien Zaccaro, Javier Mayén Guillén, Eric Gros d'Aillon, and Jean-Marie Verillhac. The optoelectronic characterization was carried out at the Department of Physics and Astronomy of Bologna. Further analyses are still being carried out to complete this study for publication in a peer-reviewed journal.

3.5.1 Introduction

One of the most critical issues with MHP-based devices is their strong reactivity with environmental gases, especially oxygen and water. Several studies demonstrated that interaction with both molecules leads to severe changes in the optoelectronic properties of the devices.[11,191,192] Sometimes these effects are found to be reversible, other times they lead to irreversible changes in the MHP physical properties. Sometimes the effects are detrimental, other times they positively impact the optoelectronic properties of MHPs. Brenes et al.[193] showed that polycrystalline grains of $MAPbI_3$ emit a brighter and steadier photoluminescence (PL) in presence of oxygen or water molecules. By time-resolved PL analyses, Song et al.[194] $MAPbI_3$ and $MAPbBr_3$ thin films undergo complex multi-stage processes in presence of water molecules, which include electron doping, surface passivation, and water incorporation. Motti et al.[195] showed that in $MAPbBr_3$ thin films oxygen is able to heal sub-bandgap defect states that are formed under dry conditions. Other studies investigated the electrical properties and ionic conduction in presence of environmental gases. Senocrate et al.[12] found that in $MAPbI_3$ thin films oxygen has an effect both on electron doping and ion diffusion, especially under illumination conditions. Despite water and oxygen have a greater impact on thin films,[196] also MHP single crystals are not immune to their effect. Fang et al.[197] showed that exposure to air, oxygen, moist atmosphere and dry gases has a severe and fast impact on the PL properties of $MAPbBr_3$ single crystals. These effects are visible also in the electrical characteristics under dark and illumination conditions. All the above-mentioned studies report these effects to occur at the timescale of seconds, minutes, or hours at most. This shows that interaction with air molecules with MHPs is an extremely efficient and fast process. A deeper understanding of it could lead to applications that take advantage of the positive effects of oxygen and moisture on MHPs, but at the same time hinder the negative ones.

In this work, we carried out an optoelectronic characterization of $MAPbBr_3$ single crystals under different environmental gases. We first compared the I-V characteristics in air with the ones in dry atmospheres, and we investigated the relevance of surface currents in top-bottom electrical devices. Then, we performed a PICTS characterization under different atmospheres, to investigate the effects of different gas molecules on the ion migration phenomena of this material.

3.5.2 Electrical characterization under different atmospheres

Figure 3.16a shows the dark current-voltage (I-V) characteristics of a $MAPbBr_3$ single crystal device in ambient condition and under primary vacuum, for decreasing pressure, between $25\cdot10^{-3}$ and $6\cdot10^{-3}$ mbar. Vacuum has the effect of increasing the device resistance, which more than doubles, from 1.9 MΩ at ambient pressure to 5.1 MΩ at $6\cdot10^{-3}$ mbar. We note that the time elapsed between the ambient pressure measurement and the first measurement under vacuum ($25\cdot10^{-3}$ mbar) is less than 1 minute. This shows that the physical phenomenon causing this effect occurs quite rapidly. This points to a surface phenomenon, as it is unlikely for the crystal bulk to respond so quickly to changes in the external atmosphere. We also found the effect to be reversible, i.e., the resistance decreases back to the initial value upon returning the sample to ambient pressure. This effect was already reported by Fang et al.[197], who observed a fast change of both photoluminescence and electrical current in $MAPbBr_3$ single crystals, upon changing the environmental gas during the measurements. Given the reversible nature of this effect, they attributed it to physisorption of H_2O and O_2 molecules, rather than to chemical reactions. We agree with this interpretation, and we provide further evidence for it. The same effect is observed upon exposing the single crystal to dry argon atmosphere (**Figure 3.17b**). Argon is an inert gas, which does not chemically interact with $MAPbBr_3$, and, for this reason, is also used for long term storage of MHPs. Since the increase in resistance is observed also in such atmosphere, the chemical reaction interpretation can be ruled out. The reason why this effect occurs in argon is probably that water and oxygen molecules leave the surface of the crystal because of the drop in partial pressure of H_2O and O_2 in the atmosphere.

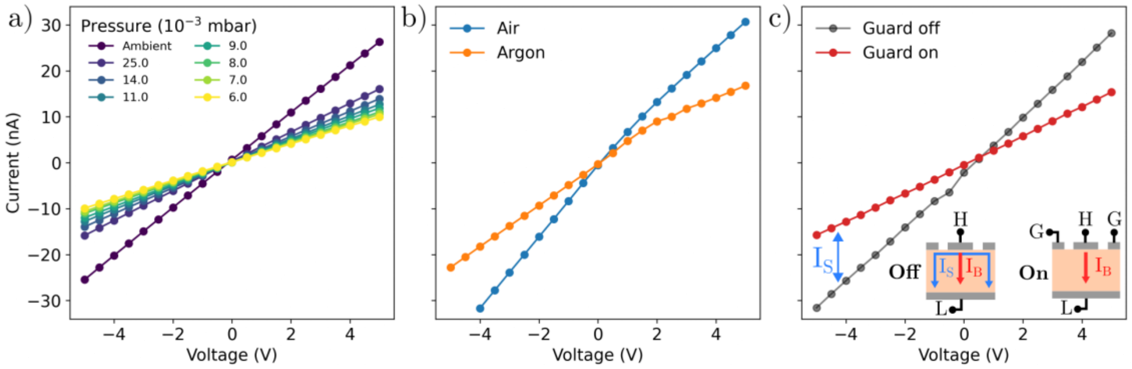

Figure 3.18 a) Dark I-V characteristics of $MAPbBr_3$ single crystal devices at ambient pressure, and under vacuum. For decreasing pressure (from 25 to 6 10^{-3} mbar), the sample resistivity increases. **b)** The same effect observed is under argon atmosphere. **c)** Dark I-V measurement in air with and without guard ring, revealing that a large part of the dark current comes from the surface. On the lower right corner is reported a schematic of the connections with and without guard ring. I_B represents the bulk current, I_S the surface current. The blue double arrow indicates the surface current contribution, which is the difference between the I-V curves with and without guard ring.

The question that naturally arises looking at these results is the following: how is it possible that in a bulk single crystal, with top-bottom contacts, surface effects like water and oxygen adsorption have such a large impact on the measured current? Indeed, one would expect most of the current in such devices to run in the bulk, which should not be affected by the external atmosphere. However, Almora et al.[198] recently showed that in $CsPbBr_3$ single crystals with top-bottom contacts most of the current arises from the surface, by performing electrical measurements with use of a guard ring. A guard ring (GR) consists of a third electrical contact that completely surrounds the top contact. The GR is connected to a unity gain buffer with high input impedance, so that no current can flow between the GR and the bottom contact. At the same time, the GR is kept at the same potential as the top contact, so that no current can flow between the two. This configuration ensures that the current from top to bottom contact can flow only through the bulk of the crystal, as the GR hinders any other lateral current contributions. Almora et al. showed that in $CsPbBr_3$ the dark current measured with a GR was only 20-40% of the current measured without a GR. This indicates that 60-80% of the total current comes from surface currents. We performed the same measurements on $MAPbBr_3$ single crystals with a GR electrode, and found similar results. The measured I-V curves in air with and without GR are shown in **Figure 3.19c**, which also contains a schematic cross-section representation of the guard ring configuration. We found the dark current to decrease of approximately 55% by using a GR, indicating that 45% of the measured current in the $MAPbBr_3$ device comes from surface currents. This demonstrates that it should be no surprise that the electrical response of $MAPbBr_3$ shows such large and fast dependence on the atmosphere surrounding the crystal, since almost half of the total current in a standard top-bottom configuration arises from the surface.

3.5.3 PICTS measurements under different atmospheres

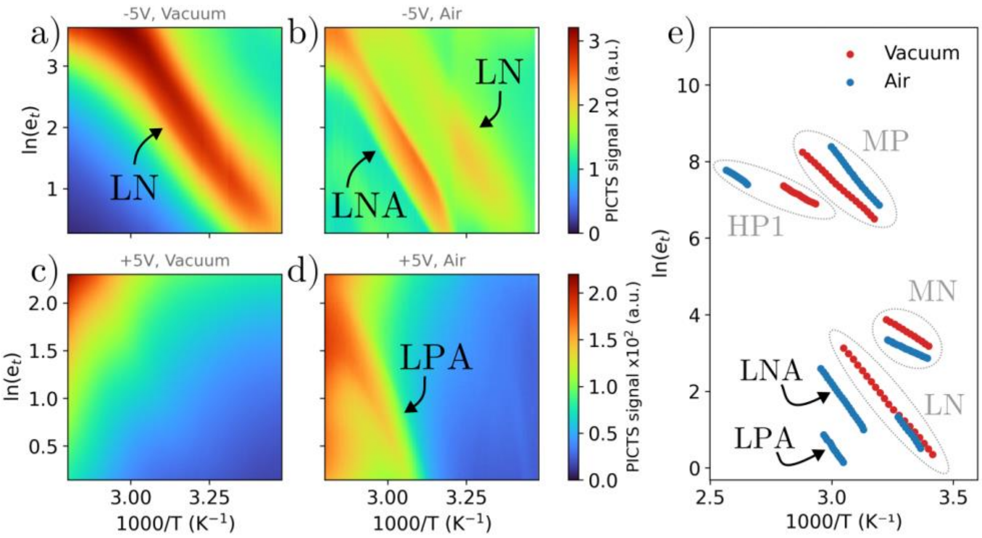

Figure 3.20 Low frequency (2.5 s excitation time) PICTS spectra of a $MAPbBr_3$ single crystal device measured with negative bias of -5 V in vacuum **(a)** and in air **(b)**, and with positive bias of +5 V in vacuum **(c)** and in air **(d)**. Each signature is labelled with the corresponding notation introduced in Section 3.4. In **(e)** are reported all the Arrhenius plots obtained at low, medium, and high frequency excitation mode, both in vacuum (red dots), and in air (blue dots). New features appear in air only with low frequency excitation, one at positive (labelled LPA: Low-Frequency, Positive Bias, Air) and one at negative bias (labelled LNA: Low-Frequency, Negative Bias, Air).

We performed a PICTS characterization in air, and compared it with results under vacuum, to assess if the atmosphere has an impact also on the moving ions in $MAPbBr_3$ crystals. We had to limit our investigation to temperatures above 273 K, i.e., 0°C, to avoid water condensation on the crystals during measurements, which could lead to sample degradation. Luckily, this is a mild limitation, as all traps measured in vacuum, except for one (HP2), appears above 273K (see **Figure 3.12** and **Figure 3.13**). We repeated the characterization in air using the same voltages and excitation times as for the vacuum measurements (see Section 3.4.3). **Figure 3.20** shows the PICTS spectra measured with 2.5 s excitation time for both positive (+5 V), and negative bias (-5 V). The PICTS measurement in vacuum at -5 V (**Figure 3.20a**) shows the LN feature already discussed in Section 3.4. When the same measurement is repeated in air (**Figure 3.20b**), a new feature appears, which we label as LNA (Low-frequency, Negative voltage, Air). The PICTS measurement in vacuum at +5 V (**Figure 3.20c)** shows no signature, as already shown in Section 3.4. When the same measurement is performed in air (**Figure 3.20d**), a feature appears, that we label LPA (Low-frequency, Positive voltage, Air). These signatures are all represented in a single Arrhenius plot in **Figure 3.20e**.

The LN feature in air clearly overlaps with the one under vacuum, indicating that they are related to the same migrating species. In the Arrhenius plot are also represented the results of the PICTS measurements in the medium and high frequency regimes, both in air and in vacuum. The MN, MP, and HP1 features are observed also in air, with no additional features. We note that these medium and high frequency features in air do not exactly overlap with the corresponding measurements under vacuum. Indeed, they show slightly different slopes and intercepts. However, their proximity in the Arrhenius space with their vacuum counterparts leads us to assigning them to the same species. **Table 3.5** shows the activation energies and diffusion coefficients at room temperature of the PICTS signatures.

Name	**Atmosphere**	E_a **(eV)**	D_{300K} **(cm^2/s)**	**Assignment**
LN	Vacuum	0.67 ± 0.03	$(2.3\pm0.2)\cdot 10^{-9}$	MA_i^+
LN	Air	0.68 ± 0.04	$(1.9\pm0.2)\cdot 10^{-9}$	MA_i^+
LN	Oxygen	0.64 ± 0.03	$(2.1\pm0.2)\cdot 10^{-9}$	MA_i^+
LNA	Air	0.79 ± 0.04	$(3.9\pm0.4)\cdot 10^{-10}$	-
LPA	Air	0.79 ± 0.04	$(7.7\pm0.7)\cdot 10^{-11}$	-

Table 3.5 Activation energies and diffusion coefficients at room temperature of the PICTS signatures measured at low frequency in vacuum, air, and oxygen atmospheres.

Air contains two chemical species that strongly interact with MHPs: oxygen, and water.[12,153,154,182,194,199,200] For this reason, we conducted more experiments to determine which of the two species is the cause of the additional low-frequency features in air. **Figure 3.21a** shows the effect of oxygen on the dark I-V curve of the device. Here the sample was first measured in air, then a primary vacuum of 10^{-3} mbar was pumped, and, finally oxygen (99.99%

purity) was introduced in the chamber. As shown previously, vacuum reduces the dark current, and we found oxygen to have the same effect, as the dark current further decreases after 45 min under oxygen atmosphere. To study the effect of water, we exposed the sample to Argon gas bubbled through distilled water, reaching a measured relative humidity of 80%. **Figure 3.21b** shows the dark I-V curve under dry argon, and the time evolution during exposure to moist argon. The effect of water is opposite to the one of oxygen, as the dark current increases by approximately 5 times after 100 min exposure to a moist atmosphere. This is a strong indication that the excess dark current measured in air is related to water absorption on the sample, rather than oxygen.

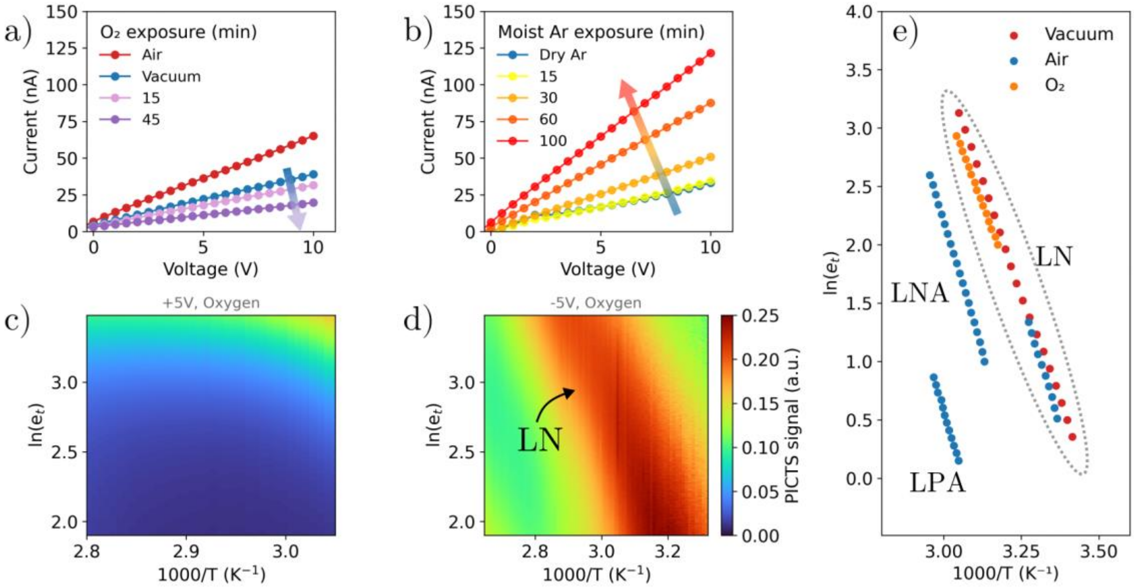

Figure 3.21 a) Dark I-V curves of a MAPbBr$_3$ single crystal device in air, under rough vacuum ($\approx 10^{-3}$ mbar), under exposure to O$_2$ gas for 15 to 45 minutes. **b)** Dark I-V curves under dry argon, and time evolution of the curves under exposure to moist argon atmosphere (relative humidity 80%) for 100 minutes. **c-d)** PICTS maps of a MAPbBr$_3$ device under oxygen atmosphere at positive and negative bias, respectively. **e)** Arrhenius plots of all ionic signatures measured with low frequency excitation (2.5 seconds) in both positive and negative bias, under vacuum, air, and oxygen atmospheres. The feature measured under oxygen perfectly overlaps with LN, observed also in vacuum and in air.

Figure 3.21c-d shows the PICTS characterization under oxygen at positive and negative bias. We limited the measurements to the ones at low frequencies, as we established that the low frequency maps are the only ones affected by air exposure. The PICTS map at +5 V shows no feature, while the one at -5 V shows a single feature. **Figure 3.21** shows an overlay with the previous results in air and vacuum. The feature at negative bias perfectly overlaps with the LN feature measured under air and vacuum. These results show that oxygen does not introduce any additional ionic migrating species in $MAPbBr_3$. The resulting ion migration parameters are reported in **Table 3.5**, and confirm the good agreement with the LN parameters. Unfortunately, we were not able to perform PICTS measurements under moist argon due to sample degradation. We noticed that after the 100 min moist argon exposure the sample's surface became opaque, probably due to the well-known degradation reaction of MHPs with water, leading to the formation of the white-coloured compound $PbBr_2$.[200]

3.5.4 Discussion and conclusions

Despite the impossibility of performing PICTS measurements under moist argon atmosphere, we have two indications that point to water as the cause of the additional PICTS features measured in air. The first is that the dark current behaves similarly when the material is exposed to air or water, as opposed to oxygen which seems to have the same effect as atmospheres like vacuum and argon. The second indication, which well agrees with the first one, is that PICTS measurements under oxygen yield the same results as under vacuum, thus leaving water as the only other candidate. However, further experiments will be needed to identify the exact ionic species that correspond to the LNA and LPA features. For the moment, we can speculate based on literature results about the interaction of water with MHPs. Ceratti et al. recently showed evidence that also protons (H^+) can migrate inside MHPs.[182] These can be released by MA^+ cations, especially in presence of environmental humidity, which speeds up the reaction. By temperature-dependent NMR and Raman measurements, they estimated the activation energy and diffusion coefficient at room temperature for H^+ to be 0.2-0.6 eV and 10^{-9}-10^{-10} cm^2/s in $MAPbI_3$, $MAPbBr_3$, and $FAPbBr_3$. Being positively charged, H^+ might be associated to the LNA signature. Despite having a slightly higher activation energy of 0.79 eV, the diffusion coefficient of $3.9\ 10^{-10}$ cm^2/s of LNA falls within the range identified by Ceratti et al. The LPA feature is instead related to a negatively charged specie, which might be, for example, OH^-. However, to our knowledge, no research group up to now has ever reported negatively charged water-related ionic species in MHPs, so for the moment this remains pure speculation. We also note that LNA and LPA could also be ionic species that do not directly stem from water molecule dissociation, like H^+ or OH^-, but vacancies or interstitials of native elements in the sample, created upon interaction with water. For example, a computational study by Kye et al.[200] predicted that moisture could induce V_{PbI_2} partial Schottky vacancy complexes in $MAPbI_3$.

In conclusion, in this work we showed by means of a guard ring that the relevant and fast changes in the electronic properties of $MAPbBr_3$ single crystal under different atmospheres can be ascribed to surface effects. These are shown to contribute to almost half of the dark current, even in top-bottom contacted devices. PICTS characterization in air revealed the presence of two additional migrating ionic species with respect to vacuum: an anion and a cation. These are the slowest migrating ions detected by PICTS on $MAPbBr_3$, with room temperature diffusion coefficients of 10^{-10}–10^{-11} cm^2/s. This shows that interaction with air molecules induces slow migration phenomena, which could severely impact the performance of the devices, creating additional hysteresis and long-term instability. Further investigation under oxygen and moist atmospheres points to water as the probable cause of the additional ionic species. This work is an important step forward in the understanding of the complex effects that environmental gases have on the electronic and ionic properties of MHPs, an aspect of fundamental importance to reach stable and reliable performance of real-world optoelectronic devices.

3.6 Impact of environmental growth conditions on the chemical and opto-electronic properties of $MAPbBr_3$ single crystals

In this section, I show the results of a comparative study between $MAPbBr_3$ single crystals grown in air, and in a dry glovebox environment. The study involved both a chemical analysis of the bare crystals, and an opto-electronic characterization of the contacted devices. The synthesis and chemical analysis of the samples was carried out in Insitut Néel/CEA of Grenoble, in collaboration with Julien Zaccaro, Javier Mayén Guillén, Eric Gros d'Aillon, and Jean-Marie Verillhac. The optoelectronic characterization was performed at the Department of Physics and Astronomy of Bologna. Further analyses are still being carried out to complete this study for publication in a peer-review journal.

3.6.1 Introduction

As discussed in the previous section, environmental oxygen and water are among the strongest agents that cause degradation of metal halide perovskite (MHP) devices. The reason is the tendency of Pb, Sn, and Ge at oxidizing in presence of water, which leads to degradation reactions like $\mathrm{AMX_3} \rightarrow \mathrm{AX} + \mathrm{MX_2}$, breaking down the perovskite structure into its constituent components.[11] This is one of the most urgent issues to be addressed in MHP devices, as it is one of the main factors hindering their commercialization.

The perovskite precursors (AX, MX_2) and solvents (DMF, DMSO, GBL) are extremely hygroscopic, which further complicates the task of avoiding water to enter the perovskite structure. Indeed, perovskite thin film fabrication is virtually always carried out in dry atmosphere inside a glovebox, where all precursors and solvents are also stored, to avoid water absorption. Usually, thin films are then coated using hydrophobic layers that protect them from moisture, once they exit the glovebox.[15] Several studies showed how water is able to infiltrate in the perovskite structure. One of the most used techniques to study this effect is Fourier Transform Infrared Spectroscopy (FTIR), as water introduces a distinct peak at 3500 cm^{-1} in infrared absorption spectra. Müller et al.[73] showed by FTIR that water is able to infiltrate in

$MAPbI_3$ in a timescale of seconds, and that the effect is reversible upon exposing the film to a dry atmosphere (e.g., N_2 or O_2). Similarly, Zhuan et al.[201] used FTIR absorption spectra to characterize the decomposition of $MAPbI_3$ into its monohydrated form $MAPbI_3 \cdot H_2O$. Similar studies were carried out also on $MAPbBr_3$, and $MAPbI_{3-x}Br_x$.[202,203]

MHP single crystals are notoriously more environmentally stable than their polycrystalline film counterparts. Wang et al.[196] found that the degradation rate under moisture scales linearly with grain size, showing that grain boundaries offer preferential sites for water molecules absorption. This implies that single crystals, which by definition constitute a single grain, are more resilient to moisture degradation. This, however, does not make MHP single crystals immune to it. Indeed, especially their surface easily undergoes degradation under moisture, as several studies demonstrated.[79,204] Despite this, MHP single crystal growth, as opposed to thin films, is virtually always carried out in air, also by the most expert research groups on high-quality perovskite single crystal growth, like the Mercouri Kanatzidis group,[205] the Osman Bakr group,[206] the Henry Snaith group,[42] and the Jinsong Huang group.[50] In this study, we carry out the entire MHP single crystal growth in a dry environment to investigate if this leads to improvement in the final device performance. As a benchmark, we used $MAPbBr_3$ single crystals. We compared two batches of single crystals, one grown in air and using precursors exposed to ambient humidity, the other grown in an argon-filled glovebox using ultra-dry precursor and solvents, that were never exposed to ambient humidity. We will refer to the crystal from the former condition as to *wet* crystals, and from the latter condition as to *dry* crystals. The details on the chemical synthesis are described in Chapter 2. We first performed a chemical characterization to look for any evidence of higher water incorporation in the wet crystals. Then, we performed an optoelectronic characterization of dry and wet devices to compare the performance of the two batches.

3.6.2 Chemical characterization

We first performed a FTIR investigation of the dry and wet samples to determine the content of oxygen- and water-related species. As discussed in the introduction, this technique has been successfully used by many research groups to assess the presence of water in MHP samples. **Figure 3.22a** shows the FTIR spectrum of dry and wet $MAPbBr_3$ powders, measured in the attenuated total reflection geometry. Powders were obtained by grinding single crystals. Powder analysis was chosen to investigate the impact of environmental growth conditions on the bulk of the crystals, rather than the surface. The dashed grey lines overlaid on the spectra represent the wavenumber of infrared absorption reported by Glaser et al.[207] for $MAPbBr_3$. The FTIR peaks of both dry and wet samples perfectly overlap with literature data, confirming the good quality of our samples. However, we did not observe any additional water or oxygen-related peak in wet samples with respect to dry samples. In particular, we did not observe in any of the two samples the broad absorption at 3500 cm^{-1} related to O-H stretch vibrations reported by several groups.

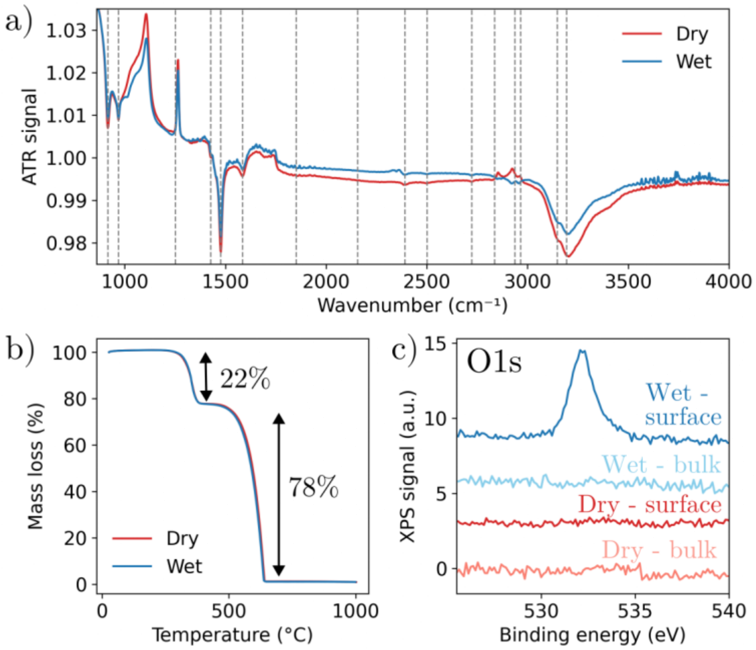

Figure 3.22 a) Attenuated Total Reflection (ATR) FTIR measurement of dry and wet $MAPbBr_3$ crystal powders. Vertical dashed grey lines correspond to the peaks reported in literature by Glaser et al. for $MAPbBr_3$.[207] **b)** Thermo-gravimetrical analysis (TGA) of dry and wet $MAPbBr_3$ powders, from room temperature up to 1000°C. **c)** XPS measurements in the O1s binding energy region, related to water. Spectra are reported for a dry and a wet sample, and for both surface and bulk. XPS measurements are courtesy of Javier Mayén Guillén.

We then moved to thermo-gravimetrical analysis (TGA), another technique that was used in literature to investigate the presence of water in MHP samples. **Figure 3.22b** shows the TGA measurements of dry and wet samples between room temperature and 1000°C. As expected from literature results,[208] the TGA curves show a first mass loss of around 22% at 300°C, due to the loss of the organic part, and a second mass loss of around 78%, due to the loss of the inorganic part. The curves of dry and wet samples overlap perfectly, showing no difference between the two growth conditions. None of the two samples shows a weight loss of a few percent below 200°C, which was previously assigned to water loss by Attique et al.[209] We conclude that, if environmental growth conditions have an impact on the amount of water-related species in $MAPbBr_3$ crystals, this is below the detectivity limit of FTIR spectroscopy and TGA. Conventional FTIR setups have a sensitivity to water in the ppm range,[210] while TGA setups typically have a sensitivity of 100 ppm weight loss.[211]

We finally performed a XPS analysis, which can typically attain higher sensitivity with respect to FTIR and TGA, below the ppm limit for light elements like oxygen.[212] XPS is a surface-sensitive technique, but it can also be used to investigate bulk properties, if the bulk is properly exposed before the measurement. To do so, we cleaved the single crystal samples during their entrance in the XPS chamber. Such cleaving process occurred under vacuum, so that the bulk was never exposed to environmental gases before the measurement. A similar procedure was also followed by Wang et al. for a XPS study of $MAPbBr_3$ single crystals.[79] **Figure 3.22c** shows the XPS spectra of dry and wet samples, acquired from both the surface and the bulk. The spectra are reported in the binding energy region around 530-535 eV, where the water-related oxygen signature (O1s) is expected. In the bulk, neither the dry nor the wet samples show any water content. On the surface, water is detected only in the wet sample. The wet sample was stored under argon atmosphere between the growth in air and the XPS measurement, so its higher surface content of water can only be ascribed to air exposure during growth, and to higher exposure of the precursors to environmental humidity. Therefore, we conclude that wet samples contain larger amount of water, only in the surface region, and in sub-ppm concentration. Dry samples, instead, if they contain any amount of water, it is below the sensitivity of the XPS technique, which is in the low ppb range.[212]

3.6.3 Opto-electronic characterization

To evaluate the effect of higher water content on the optoelectronic performance of the devices, we performed an opto-electronic characterization of a batch of 10 $MAPbBr_3$ single crystals, 5 from the wet condition and 5 from the dry one. All devices were fabricated in a top-bottom Cr electrode configuration, the same used for the studies reported in the two previous sections. After growth and evaporation, all samples, including the dry ones, were exposed to air during the polishing procedure, and were electrically tested in air. **Figure 3.23a** shows the dark current density – electric field (J-E) characteristics in air of all samples, the dry ones as red dots, and the wet ones as blue dots. It is immediately clear that dry samples show lower and more reproducible dark current values. This is better visualized in **Figure 3.23b**, which shows the resistivity values calculated by linearly fitting the dark J-E curves. Dry samples show an average resistivity of 394 MΩcm, which is almost twice the 222 MΩcm of the wet samples. Moreover, dry samples show much less dispersion in the resistivity values, with a standard deviation of 28 MΩcm, which is more than three times lower than the 97 MΩcm of wet samples.

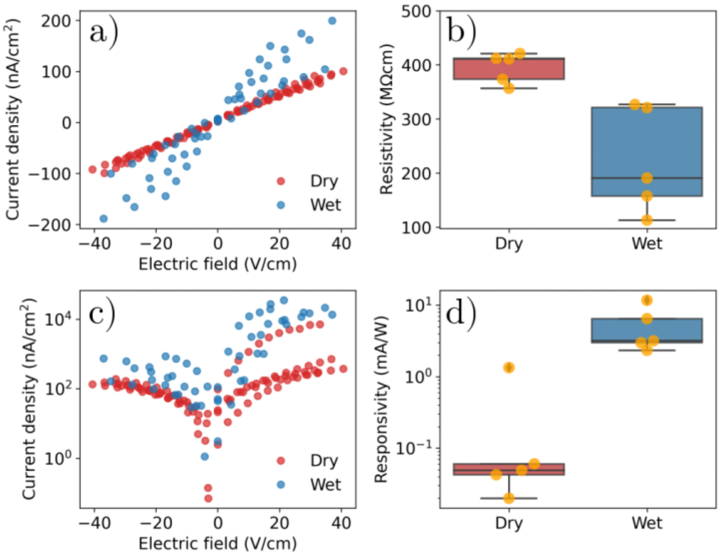

Figure 3.23 a) Dark current density – electric field (J-E) characteristics in air of ten $MAPbBr_3$ single crystals, five grown in dry conditions (red dots), and five in wet conditions (blue dots). **b)** Distribution of resistivity values calculated by linearly fitting the dark JE curves in (a). Dry samples show higher resistivity and more reproducibility. **c)** J-E curves of the same devices under 3 mW/cm^2 475 nm blue LED illumination. **d)** Responsivity of the devices calculated from the J-E curves under light in (c), at an applied field of 20 V/cm. The wet samples show a two orders of magnitude higher responsivity with respect to the dry samples.

Figure 3.23c shows the J-E curves measured under 3 mW/cm^2 475 nm blue LED illumination. Surprisingly, the wet samples outperform the dry ones, with much higher photocurrent values. **Figure 3.23d** shows the calculated responsivity at an applied electric field of 20 V/cm. Wet samples show an average responsivity of 5.3 mA/W, which is more than two orders of magnitude higher than the 0.04 mA/W responsivity of the dry samples.

3.6.4 Discussion and conclusions

The only technique that was able to detect any chemical difference between dry and wet samples was XPS, which revealed water content only on the surface of wet samples. The XPS analysis of the bulk of both classes of crystals did not reveal any water content. This indicates that crystal growth under humid conditions has no effect on the bulk of the crystal, but only on its surface. We understand these results in the following terms. Crystallization can be considered as a purification process, in which impurities, like H_2O molecules contained in the precursors and solvents, are excluded from the growing lattice and pushed towards the surface, which consequently contains a high density of such impurities. This is the most plausible explanation of our results. Another possibility is related to the moment when the crystal is extracted from the growth solution. The dry crystals are exposed to a dry atmosphere in this moment, while wet ones are exposed to humidity in the air. MHPs are known to quickly adsorb water molecules from the environment,[73,197] so wet crystals might pick up most of their water content in this moment. However, the difference in the optoelectronic performance is visible even after exposure to air of the dry samples (polishing and J-E measurements are performed in air for all samples). Therefore, we consider water incorporation during the growth process to be the most probable explanation. Dry crystals surely pick up water when exposed to the environment, but the amount incorporated water during growth seems to be higher, at least in fresh samples. Certainly, a long-term exposure to moisture will finally lead to the incorporation of enough water to hide any difference between dry and wet samples.

The optoelectronic characterization revealed that the surface water molecules have a large impact on the electrical properties of $MAPbBr_3$. This might be surprising for top-bottom electrode devices, as the bulk seems unaffected by the exposure to humidity during growth. However, as recently shown by Almora et al.[198], and by our study reported in Section 3.5, surface currents greatly contribute to the total electrical current in MHP single crystals. Therefore, it is reasonable that water contamination of the surface can have such an impact on the electrical performance of MHP devices.

The impact of growth environment on the optoelectronic properties of the devices is not straightforward, as it changes drastically between dark and light conditions. In the dark, dry $MAPbBr_3$ show higher resistivity and better reproducibility among samples. Both these features are desirable for detector applications. We ascribe the lower resistivity of wet samples to the doping effect of water molecules, a process that is well known to occur in MHPs.[194] This is also confirmed by our results reported in Section 3.5, where we observed that exposure to a highly humid atmosphere of $MAPbBr_3$ devices leads to an increase in dark current. Under visible light, the situation is opposite: wet samples show better performance, with more than two orders of magnitude higher responsivity than dry samples. It is surprising how a degrading molecule for the perovskite structure like H_2O can lead to an improvement in device performance. However, the literature is full of examples where water was found to enhance MHP device performance, when present in the correct amount. A computational study by Long et al. suggests that moderate humidity can increase the electron-hole recombination time in $MAPbI_3$.[199] The group of Samuel Stranks found that in $MAPbI_3$ thin films exposure to water allows for a bright and steady photoluminescence emission, with respect to a dry nitrogen atmosphere. Gong et al. showed that a few percent addition of water to the DMF solvent during fabrication of $MAPbI_{3-x}Cl_x$ solar cells leads to improved photoconversion efficiency. Typically, these results are explained as a passivation effect of water on intrinsic defects in the perovskite structure, like halide vacancies, which is one of the possible interpretations for the improved performance of our wet devices. We note, however, that another interpretation is possible, based on photoconductive gain effects. Photoconductive gain is an effect observed in many photoconductors, where the photocurrent signal is amplified, due to defects. If such defects create long-lived electronic states for either electrons or holes, the other photogenerated carrier is forced to flow several times in the circuit before recombining.[213] Such effect has been observed in detectors based on MHPs like $MAPbI_3$,[126] and it was observed to occur at defective states at the MHP/TiO_2 interface,[127] as well as at the MHP/graphene interface.[214] Therefore, another possibility is that H_2O introduces long-lived electronic defect states that cause a gain effect, resulting in higher responsivity under visible light. Both interpretations presented here remain plausible, and further investigations are planned to identify the correct one.

In conclusion, this study revealed that different environmental conditions during crystal growth have a relevant impact on the water content of the $MAPbBr_3$ surface, but not in the bulk. Water on the surface of crystals grown in a humid environment is found to decrease resistivity, but, at the same time, to largely improve responsivity under light. This highlights a double role of water, acting both as a positive and negative factor in the performance of MHP photodetectors. This study reveals the importance of the environment during growth of MHP single crystals, a factor that we think did not receive enough attention up to now in the literature on MHP single crystals. Moreover, this study represents a further step in understanding the complex role of water on the photo-electrical properties of MHP devices.

Conclusions

This thesis work focussed on the defect characterization of hybrid metal halide perovskite (MHP) materials and devices. The investigated defects were both intrinsic to the MHP structure, and extrinsic, i.e., due to external agents such as ionizing radiation, mechanical stress or environmental gases. In this work, I carried out different experimental activities, ranging from chemical synthesis and device fabrication, to electrical, optical and chemical analyses. These activities were carried out at the Department of Physics and Astronomy of the University of Bologna, in the Semiconductor Physics research group, and at the Insitut Néel (CNRS) and CEA of Grenoble, France.

By means of surface photovoltage spectroscopy, we found that X-ray irradiation creates a bound excitonic specie in methylammonium lead bromide ($MAPbBr_3$), with exciton binding energy of 39 meV. This result is relevant for X-ray detection applications, as a higher exciton binding energy is expected to decrease the charge collection efficiency, thus reducing device performance. By means of X-ray photoelectron spectroscopy (XPS), we found the cause of this effect to be the creation of bromine vacancies in the perovskite structure, which locally change the lattice screening, thus modifying the exciton binding energy. We found this effect to be reversible over the timescale of days, thanks to the passivation of the bromine vacancies by oxygen and water molecules. By XPS, we also found that irradiation in air causes the formation of water molecules on the surface of $MAPbBr_3$, due to a X-ray-triggered reaction of the MHP with environmental oxygen. This study demonstrated that chemical stability and interaction with the environment are crucial aspects that should be addressed to obtain stable and reliable performance by MHP X-ray detectors.

Kelvin probe force microscopy measurements allowed to identify the interface that leads to the delamination of perovskite/silicon tandem solar cells, a known issue of these devices, which often leads to device failure. Our measurements identified C_{60}/SnO_2 to be the weak interface causing delamination of the solar cells. Further measurements demonstrated that this interface is weakened by the morphology of the underlying layers, and by device heating during specific steps of the fabrication procedure. This work identified the critical materials and procedures that should be optimized to improve mechanical stability of perovskite/silicon tandem solar cells.

A consistent part of my work focussed on the development and realization of photo-induced current transient spectroscopy (PICTS) measurements on MHP single crystals, with the aim of characterizing electronic defects in these samples. PICTS measurements were carried out on 2-dimensional (2D) MHP samples (in particular, PEA_2PbBr_4), and allowed to determine three electronic trap states with activation energies of 0.33, 0.40, and 0.52 eV, and with large capture cross sections in the range 10^{-12}-10^{-14} cm^2. We found these signals to be stable upon ageing and across different samples. We also found that high-dose X-ray irradiation induces changes in the trapping parameters of one of the three defect states, but it does not introduce new electronic defect states in the material. This is the first complete defect characterization of a 2D MHP ever reported in literature, and it is a first step towards identifying the impurities that limit the opto-electronic performance of these materials.

PICTS measurements were also carried out on 3-dimensional (3D) MHPs, in particular on $MAPbBr_3$ single crystals. We found several indications that the PICTS signals measured from this material are related to ionic motion, rather than electron trapping processes. Therefore, we developed a model to interpret PICTS results in terms of migrating ionic species. We identified five ionic species, with activation energies in the range between 0.3 and 0.7 eV, and estimated their diffusion coefficients to be between 10^{-9} and 10^{-7} cm^2/s. This study proved PICTS to be a valid technique to characterize ion migration in MHPs, a critical issue afflicting these materials, which has to be addressed to achieve long-term electrical and chemical stability of MHP devices.

PICTS was also used to investigate another issue afflicting MHPs, their high reactivity under humidity and environmental gases. We found that exposure to air introduces two new migrating species in $MAPbBr_3$ single crystals, with low diffusion coefficients of $3.9 \cdot 10^{-10}$ and $7.7 \cdot 10^{-11}$ cm^2/s. Based on our tests under different atmospheres, we attributed these species to the interaction of the MHP structure with water molecules in the air. This result showed that interaction with water can not only cause chemical degradation of the perovskite structure, but also introduce electrically active slow-moving ions, which may harm device performance.

Despite the above-mentioned reactivity of MHPs to oxygen and humidity, MHP single crystal growth is usually carried out in air, as opposed to thin film deposition which is normally performed under dry atmosphere. This may possibly lead to the inclusion of degrading molecules such as oxygen and water in the MHP single crystal structure. To test this hypothesis, we performed a comparative study between MHP single crystals grown in air and under dry argon atmosphere. By means of XPS, we found that crystals grown in air tend to adsorb water molecules on the surface, while no water content was revealed in the bulk. We found that samples grown in dry atmosphere show higher resistivity and better reproducibility of the electrical characteristics. However, samples grown in air showed two orders of magnitude higher sensitivity to visible light, implying a strong positive effect of the adsorbed water on the opto-electronic response of the crystal. This study highlighted the importance of the atmosphere control during the growth of MHP single crystals, revealing a double role of water as an agent that negatively affects reproducibility, but also enhances the optoelectronic response.

In conclusion, this work constitutes a significant advancement in the characterization of a variety of defects that affect MHP materials and devices. These include X-ray-induced defects, mechanical delamination, electronic defect states, ion migration, and defects induced by chemical reactions with the environment. The identification of impurities and defects in MHPs, and the understanding of their role is a key issue in the development of stable and high performance MHP-based devices. This work paves the way to the development of methods to passivate and eliminate such impurities, and improve device performance and stability.

Appendix A

PICTS measurement protocol

In this Appendix I describe a typical procedure for PICTS measurements with the setup implemented at the Department of Physics and Astronomy of Bologna. The goal is to acquire photocurrent transients in a given temperature range, chosen by the user.

Vacuum pumping

The vacuum pump is connected to the cryostat and it is turned on. The pressure in the chamber should reach the order of 10^{-3} mbar or less to avoid moisture condensation (this can require from 10 to 60 minutes, depending on the status of the cryostat). Vacuum is typically pumped dynamically for the whole measurement time. Some samples change their optoelectronic properties upon pressure changes. In this case, it is good practice to leave the sample in vacuum for the time required to stabilise them. To do so, one can acquire current-voltage characteristics of the sample both in dark and illuminated conditions over time, until they reach a stable behaviour.

Data acquisition setup

A fixed bias is applied to the sample, and the LED is modulated at a fixed frequency f at a given duty cycle. The user sets the DAQ parameters that allow to acquire a single transient that captures both the rise and fall of the photocurrent. The software allows to set the number of samples to acquire N, and the sample rate R. The acquired time period will be $t_p = N/R$. Typically, to acquire a single period, one chooses N and R so that $t_p = 1/f$. With this DAQ system the maximum value of R can be 200 kSamples/s. For $t_p > 500$ ms, the user should consider decreasing R to at least 20 kSamples/s, to avoid creating large files that could easily overcome the 1 GB size for a single temperature scan. This is unless an extremely high time resolution is needed, even at such slow modulation frequencies. The user also needs to set the trigger slope to rising or falling. Typically, the slope is set to falling, as in PICTS measurements the time index is set to 0 when the LED is turned off. This shows a transient that starts with the decay followed by the rise, which is opposite to the conventional transient representation. To compensate for this, the user should set a suitable pre-trigger time parameter so that the rise appears before the fall. If the duty cycle is 50%, this is done by setting a pre-trigger time of $N/2$. This procedure allows to save in the data file the time position when the LED turns off, which is useful for data post-processing. To improve the signal to noise ratio, it is possible to average N_{avg} consecutive transient. It should be noted that this procedure increases the time needed for the acquisition of a transient by a factor of N_{avg}. Finally, the users should also choose the location and the name of the file that will contain the acquired data.

Cryostat cooling

When vacuum has reached a suitable value, and the user is satisfied with the quality of the transient at room temperature, the procedure for cryogenic cooling can start. If the starting temperature is below room temperature, liquid nitrogen is poured inside the cryostat through the dedicated inlet. If the starting temperature is 78 K, the user should wait until this temperature is reached (it can require 20-30 minutes). If the starting temperature is between 78K and room temperature, the user should set a temperature setpoint through the software, so that the heating element can interrupt the cooling ramp at the desired setpoint. If the starting temperature is above room temperature, LN_2 is not needed and the user can just use the heater to reach the desired starting temperature. Before moving to the next step, the user should wait until the PID feedback manages to maintain the temperature at a constant value, which can require from a few seconds to a few minutes after the setpoint temperature is reached.

Heating ramp setup

The temperature ramp can now be set. The starting temperature should be close to the current temperature. The final temperature should be higher than the current temperature, without exceeding 400 K, which is the limit of this cryogenic set up. The user must then specify the heating rate for the temperature ramp and the temperature step ΔT between consecutive acquisitions. For example, if the starting temperature is 250 K, the end temperature is 400 K, and $\Delta T = 0.5$ K, the system will acquire a transient every 0.5 K from 250 K up to 400K, resulting in 300 acquired transients in total. The heating rate and the temperature step should be chosen wisely together with the averaging number, so that temperature does not significantly change during the acquisition of a single transient. For example, let's assume the user is acquiring a transient with 1 second period (LED modulation frequency of 1 Hz), and averaging over 6 transients, resulting in a 6 seconds time for a single transient acquisition. If the user choses a heating rate of 5 K/min, temperature will increase every by 0.5 K every 6 seconds. This means that, during the acquisition of a single transient, temperature changes by 0.5 K. Assuming the user wants to acquire with a temperature resolution of $\Delta T = 0.5$ K, these settings are not ideal, as the error on temperature equals the temperature step. The solution would be to lower the heating rate to at least 0.3 or 0.2 K/min.

Data acquisition

Once all parameters are set, the measurement can start. The *start* button on the software allows to start the temperature ramp and data acquisition. A panel shows in real time the acquired transient and a temperature vs time graph. When the end temperature is reached, the acquisition stops. The user can also stop the acquisition at any time with the dedicated *stop* button.

Despite the measurement being fully automated, it is advisable for the user to stand by the setup and check the transients as the ramp takes place. This is because photocurrent typically depends on temperature, and may increase during the ramp. This could lead to the overload of the current amplifier, which causes a signal saturation that makes the data not usable. In this case, the user should decrease the amplifier gain as soon as the *overload* LED turns on. If this happens, the data should be adjusted later to compensate for the change in gain in the temperature range of interest.

Appendix B

Four-gate and integral PICTS analysis

The four-gate PICTS method consists of selecting four gates t_1, t_2, t_3, and t_4, where $t_1 < t_2 < t_3 \ll t_4$. The PICTS signal is then calculated as:

$$S_{4g}(T) = \frac{i(t_2) - i(t_3)}{i(t_1) - i(t_4)} \qquad 3.9$$

This procedure also normalises the signal so that it does not contain the pre-exponential factor. Thus, S_{4g} does not need any normalisation in the case of temperature-dependent mobility lifetime product. If the denominator in Equation 3.9 can be approximated to $i(t_1)$, i.e. if $t_1 \ll t_4$, the relation between the gates and e_t is found to be

$$e_t = \frac{\ln[(t_3 - t_1)/(t_2 - t_1)]}{t_3 - t_2} \qquad 3.10$$

which is the equivalent of Equation 2.11.

As for the two-gate method, a complete set of spectra is obtained by shifting the gates along the time axis. Balland et al.[86] found that the optimal procedure is to choose rate windows that keep constant the following ratios:

$$\alpha = \frac{t_2}{t_1}, \qquad \beta = \frac{t_3}{t_1}, \qquad \gamma = \frac{t_4}{t_1} > 9 \qquad 3.11$$

Practically, t_1 is shifted along the x-axis and the other gates are determined by Equations 3.11.

Being a form of normalised PICTS, the four-gate spectra do not contain information on the current pre-exponential factor. Thus, it is not possible to extract the trap concentration from the four-gate analysis.

On the data acquired in this thesis work, we found the four-gate method to be less reliable than the double-gate method. Sometimes, four-gate spectra did not yield any trap signatures, while double-gate spectra did. Also, the four-gate method is more sensible to noise in the raw data. Finally, the four-gate methods generally restricts the frequency space that can be examined, due to the larger amount of constraints on the gates (Equations 3.11).

The integral double-gate and four-gate methods

A possible approach to PICTS analysis on data containing high noise is to use the integral version of the double or four-gate methods. The integral double-gate spectrum is calculated as

$$S_{2g,int}(T) = \int_{t_1}^{t_2} i(t,T)\, dt \tag{3.12}$$

The four-gate integral spectrum is calculated as

$$S_{4g,int} = \frac{\int_{t_2}^{t_3} i(t,T)\, dt}{\int_{t_1}^{t_4} i(t,T)\, dt} \tag{3.13}$$

we found that both integral methods, although producing less noisy spectra, tend to introduce artefacts and to reduce spectral resolution. In particular, when two peaks are close in the temperature space, the integral methods tend to blend them in a single peak, making the real parameters of both traps inaccessible.

Bibliography

1. Best Research-Cell Efficiency Chart. https://www.nrel.gov/pv/cell-efficiency.html.
2. Basiricò, L., Ciavatti, A. & Fraboni, B. Solution-Grown Organic and Perovskite X-Ray Detectors: A New Paradigm for the Direct Detection of Ionizing Radiation. *Advanced Materials Technologies* **6**, 2000475 (2021).
3. Kim, H.-S. *et al.* Lead Iodide Perovskite Sensitized All-Solid-State Submicron Thin Film Mesoscopic Solar Cell with Efficiency Exceeding 9%. *Sci Rep* **2**, 591 (2012).
4. Lee, M. M., Teuscher, J., Miyasaka, T., Murakami, T. N. & Snaith, H. J. Efficient Hybrid Solar Cells Based on Meso-Superstructured Organometal Halide Perovskites. *Science* **338**, 643–647 (2012).
5. Wehrenfennig, C., Eperon, G. E., Johnston, M. B., Snaith, H. J. & Herz, L. M. High Charge Carrier Mobilities and Lifetimes in Organolead Trihalide Perovskites. *Advanced Materials* **26**, 1584–1589 (2014).
6. Tian, W., Zhou, H. & Li, L. Hybrid Organic-Inorganic Perovskite Photodetectors. *Small* **13**, 1702107 (2017).
7. Lin, K. *et al.* Perovskite light-emitting diodes with external quantum efficiency exceeding 20 per cent. *Nature* **562**, 245–248 (2018).
8. Zhang, Q. *et al.* Advances in Small Perovskite-Based Lasers. *Small Methods* **1**, 1700163 (2017).
9. Geng, X. *et al.* Ultrafast Photodetector by Integrating Perovskite Directly on Silicon Wafer. *ACS Nano* (2020) doi:10.1021/acsnano.9b06345.
10. He, Y., Hadar, I. & Kanatzidis, M. G. Detecting ionizing radiation using halide perovskite semiconductors processed through solution and alternative methods. *Nat. Photon.* **16**, 14–26 (2022).
11. Chen, B., Wang, S., Song, Y., Li, C. & Hao, F. A critical review on the moisture stability of halide perovskite films and solar cells. *Chemical Engineering Journal* **430**, 132701 (2022).
12. Senocrate, A. Interaction of oxygen with halide perovskites. *Journal of Materials Chemistry A* 9 (2018).

13. Yuan, Y. & Huang, J. Ion Migration in Organometal Trihalide Perovskite and Its Impact on Photovoltaic Efficiency and Stability. *Acc. Chem. Res.* **49**, 286–293 (2016).

14. Moia, D. & Maier, J. Ion Transport, Defect Chemistry, and the Device Physics of Hybrid Perovskite Solar Cells. *ACS Energy Letters* 11 (2021).

15. Uddin, A., Upama, M., Yi, H. & Duan, L. Encapsulation of Organic and Perovskite Solar Cells: A Review. *Coatings* **9**, 65 (2019).

16. Bi, E., Song, Z., Li, C., Wu, Z. & Yan, Y. Mitigating ion migration in perovskite solar cells. *Trends in Chemistry* **3**, 575–588 (2021).

17. Armaroli, G. *et al.* X-Ray-Induced Modification of the Photophysical Properties of $MAPbBr_3$ Single Crystals. *ACS Appl. Mater. Interfaces* (2021) doi:10.1021/acsami.1c16072.

18. De Bastiani, M. *et al.* Mechanical Reliability of Fullerene/Tin Oxide Interfaces in Monolithic Perovskite/Silicon Tandem Cells. *ACS Energy Lett.* 827–833 (2022) doi:10.1021/acsenergylett.1c02148.

19. Goldschmidt, V. M. Die Gesetze der Krystallochemie. *Naturwissenschaften* **14**, 477–485 (1926).

20. Giovanni, D. Optical-spin Dynamics in Organic-Inorganic Hybrid Lead Halide Perovskites. (Nanyang Technological University, 2017).

21. Stoumpos, C. C. & Kanatzidis, M. G. The Renaissance of Halide Perovskites and Their Evolution as Emerging Semiconductors. *Acc. Chem. Res.* **48**, 2791–2802 (2015).

22. Abate, A. Perovskite Solar Cells Go Lead Free. *Joule* **1**, 659–664 (2017).

23. Cao, D. H., Stoumpos, C. C., Farha, O. K., Hupp, J. T. & Kanatzidis, M. G. 2D Homologous Perovskites as Light-Absorbing Materials for Solar Cell Applications. *J. Am. Chem. Soc.* **137**, 7843–7850 (2015).

24. Stoumpos, C. C., Malliakas, C. D. & Kanatzidis, M. G. Semiconducting Tin and Lead Iodide Perovskites with Organic Cations: Phase Transitions, High Mobilities, and Near-Infrared Photoluminescent Properties. *Inorg. Chem.* **52**, 9019–9038 (2013).

25. Keshavarz, M. *et al.* Tracking Structural Phase Transitions in Lead-Halide Perovskites by Means of Thermal Expansion. *Adv. Mater.* 1900521 (2019) doi:10.1002/adma.201900521.

26. Kamminga, M. E. *et al.* Confinement Effects in Low-Dimensional Lead Iodide Perovskite Hybrids. *Chem. Mater.* **28**, 4554–4562 (2016).

27. Brenner, T. M., Egger, D. A., Kronik, L., Hodes, G. & Cahen, D. Hybrid organic—inorganic perovskites: low-cost semiconductors with intriguing charge-transport properties. *Nat Rev Mater* **1**, 15007 (2016).
28. Yang, W. S. *et al.* High-performance photovoltaic perovskite layers fabricated through intramolecular exchange. *Science* **348**, 1234–1237 (2015).
29. Grundmann, M. *The physics of semiconductors: an introduction including nanophysics and applications*. (Springer, 2016).
30. Ledinsky, M. *et al.* Temperature Dependence of the Urbach Energy in Lead Iodide Perovskites. *J. Phys. Chem. Lett.* **10**, 1368–1373 (2019).
31. Awasthi, K. *et al.* Electroabsorption Studies of Multicolored Lead Halide Perovskite Nanocrystalline Solid Films. *ACS Photonics* **5**, 2408–2417 (2018).
32. Baranowski, M. & Plochocka, P. Excitons in Metal-Halide Perovskites. *Adv. Energy Mater.* **10**, 1903659 (2020).
33. Braly, I. L. *et al.* Hybrid perovskite films approaching the radiative limit with over 90% photoluminescence quantum efficiency. *Nature Photon* **12**, 355–361 (2018).
34. Stylianakis, M. M., Maksudov, T., Panagiotopoulos, A., Kakavelakis, G. & Petridis, K. Inorganic and Hybrid Perovskite Based Laser Devices: A Review. *Materials* **12**, 859 (2019).
35. Protesescu, L. *et al.* Nanocrystals of Cesium Lead Halide Perovskites ($CsPbX_3$, X = Cl, Br, and I): Novel Optoelectronic Materials Showing Bright Emission with Wide Color Gamut. *Nano Lett.* **15**, 3692–3696 (2015).
36. Nan, G. *et al.* How Methylammonium Cations and Chlorine Dopants Heal Defects in Lead Iodide Perovskites. *Adv. Energy Mater.* **8**, 1702754 (2018).
37. Goetz, K. P., Taylor, A. D., Paulus, F. & Vaynzof, Y. Shining Light on the Photoluminescence Properties of Metal Halide Perovskites. *Adv. Funct. Mater.* **30**, 1910004 (2020).
38. Kronik, L. & Shapira, Y. Surface photovoltage spectroscopy of semiconductor structures: at the crossroads of physics, chemistry and electrical engineering. *Surf. Interface Anal.* **31**, 954–965 (2001).
39. Kronik, L. & Shapira, Y. *Surface photovoltage phenomena: theory, experiment, and applications*. vol. 37 (1999).

40. Datta, S., Ghosh, S. & Arora, B. M. Electroreflectance and surface photovoltage spectroscopies of semiconductor structures using an indium–tin–oxide-coated glass electrode in soft contact mode. *Review of Scientific Instruments* **72**, 177–183 (2001).

41. Diab, H. *et al.* Impact of Reabsorption on the Emission Spectra and Recombination Dynamics of Hybrid Perovskite Single Crystals. *J. Phys. Chem. Lett.* **8**, 2977–2983 (2017).

42. Wenger, B. *et al.* Consolidation of the optoelectronic properties of CH3NH3PbBr3 perovskite single crystals. *Nat Commun* **8**, 590 (2017).

43. Levine, I. *et al.* Deep Defect States in Wide-Band-Gap ABX $_3$ Halide Perovskites. *ACS Energy Lett.* **4**, 1150–1157 (2019).

44. Barnea-Nehoshtan, L., Kirmayer, S., Edri, E., Hodes, G. & Cahen, D. Surface Photovoltage Spectroscopy Study of Organo-Lead Perovskite Solar Cells. *J. Phys. Chem. Lett.* 6 (2014).

45. Marongiu, D., Saba, M., Quochi, F., Mura, A. & Bongiovanni, G. The role of excitons in 3D and 2D lead halide perovskites. *J. Mater. Chem. C* **7**, 12006–12018 (2019).

46. Singh, S. *et al.* Effect of Thermal and Structural Disorder on the Electronic Structure of Hybrid Perovskite Semiconductor CH $_3$ NH $_3$ PbI $_3$. *J. Phys. Chem. Lett.* **7**, 3014–3021 (2016).

47. Yaffe, O. *et al.* Excitons in ultrathin organic-inorganic perovskite crystals. *Phys. Rev. B* **92**, 045414 (2015).

48. Stranks, S. D. *et al.* Electron-Hole Diffusion Lengths Exceeding 1 Micrometer in an Organometal Trihalide Perovskite Absorber. *Science* **342**, 341–344 (2013).

49. Shi, D. *et al.* Low trap-state density and long carrier diffusion in organolead trihalide perovskite single crystals. *Science* **347**, 519–522 (2015).

50. Wei, H. *et al.* Dopant compensation in alloyed CH3NH3PbBr3−xClx perovskite single crystals for gamma-ray spectroscopy. *Nature Mater* **16**, 826–833 (2017).

51. Yukta *et al.* Efficient and Highly Stable X-ray Detection and Imaging using 2D (BA)2PbI4 Perovskite Single Crystals. *ACS Photonics* **9**, 3529–3539 (2022).

52. Uxa, Š., Grill, R. & Belas, E. Evaluation of the mobility-lifetime product in CdTe and CdZnTe detectors by the transient-current technique. *Journal of Applied Physics* **114**, 094511 (2013).

53. Almora, O., Aranda, C., Zarazua, I., Guerrero, A. & Garcia-Belmonte, G. Noncapacitive Hysteresis in Perovskite Solar Cells at Room Temperature. *ACS Energy Lett.* **1**, 209–215 (2016).

54. García-Rodríguez, R., Ferdani, D., Pering, S., Baker, P. J. & Cameron, P. J. Influence of bromide content on iodide migration in inverted MAPb(I1−xBrx)3 perovskite solar cells. *J. Mater. Chem. A* **7**, 22604–22614 (2019).

55. Eames, C. *et al.* Ionic transport in hybrid lead iodide perovskite solar cells. *Nat Commun* **6**, 7497 (2015).

56. Li, C., Guerrero, A., Huettner, S. & Bisquert, J. Unravelling the role of vacancies in lead halide perovskite through electrical switching of photoluminescence. *Nat Commun* **9**, 5113 (2018).

57. Peng, W. *et al.* Quantification of Ionic Diffusion in Lead Halide Perovskite Single Crystals. *ACS Energy Lett.* **3**, 1477–1481 (2018).

58. Pockett, A. *et al.* Microseconds, milliseconds and seconds: deconvoluting the dynamic behaviour of planar perovskite solar cells. *Phys. Chem. Chem. Phys.* **19**, 5959–5970 (2017).

59. Mosconi, E. & De Angelis, F. Mobile Ions in Organohalide Perovskites: Interplay of Electronic Structure and Dynamics. *ACS Energy Lett.* **1**, 182–188 (2016).

60. Meggiolaro, D., Mosconi, E. & De Angelis, F. Formation of Surface Defects Dominates Ion Migration in Lead-Halide Perovskites. *ACS Energy Lett.* **4**, 779–785 (2019).

61. Futscher, M. H. *et al.* Quantification of ion migration in CH $_3$ NH $_3$ PbI $_3$ perovskite solar cells by transient capacitance measurements. *Mater. Horiz.* **6**, 1497–1503 (2019).

62. Xiao, X. *et al.* Suppressed Ion Migration along the In-Plane Direction in Layered Perovskites. *ACS Energy Lett.* **3**, 684–688 (2018).

63. Ceratti, D. R. *et al.* Eppur si Muove: Proton Diffusion in Halide Perovskite Single Crystals. *Adv. Mater.* **32**, 2002467 (2020).

64. Lin, Y. *et al.* Suppressed Ion Migration in Low-Dimensional Perovskites. *ACS Energy Lett.* **2**, 1571–1572 (2017).

65. Liu, Y. *et al.* Triple-Cation and Mixed-Halide Perovskite Single Crystal for High-Performance X-ray Imaging. *Advanced Materials* **33**, 2006010 (2021).

66. Xing, J. *et al.* Ultrafast ion migration in hybrid perovskite polycrystalline thin films under light and suppression in single crystals. *Phys. Chem. Chem. Phys.* **18**, 30484–30490 (2016).

67. Duijnstee, E. A. *et al.* Understanding Dark Current-Voltage Characteristics in Metal-Halide Perovskite Single Crystals. *Phys. Rev. Applied* **15**, 014006 (2021).

68. Liu, Y. *et al.* Direct Observation of Photoinduced Ion Migration in Lead Halide Perovskites. *Adv. Funct. Mater.* **31**, 2008777 (2021).

69. Kim, G. Y., Senocrate, A., Wang, Y.-R., Moia, D. & Maier, J. Photo-Effect on Ion Transport in Mixed Cation and Halide Perovskites and Implications for Photo-Demixing**. *Angewandte Chemie* **133**, 833–839 (2021).

70. Motti, S. G. *et al.* Controlling competing photochemical reactions stabilizes perovskite solar cells. *Nat. Photonics* **13**, 532–539 (2019).

71. Shirzadi, E. *et al.* Deconvolution of Light-Induced Ion Migration Phenomena by Statistical Analysis of Cathodoluminescence in Lead Halide-Based Perovskites. *Advanced Science* **9**, 2103729 (2022).

72. Philippe, B. *et al.* Chemical and Electronic Structure Characterization of Lead Halide Perovskites and Stability Behavior under Different Exposures—A Photoelectron Spectroscopy Investigation. *Chem. Mater.* **27**, 1720–1731 (2015).

73. Müller, C. *et al.* Water Infiltration in Methylammonium Lead Iodide Perovskite: Fast and Inconspicuous. *Chem. Mater.* **27**, 7835–7841 (2015).

74. Tang, X. *et al.* Photoinduced degradation of methylammonium lead triiodide perovskite semiconductors. *J. Mater. Chem. A* **4**, 15896–15903 (2016).

75. Tsai, H. *et al.* High-efficiency two-dimensional Ruddlesden–Popper perovskite solar cells. *Nature* **536**, 312–316 (2016).

76. Zhang, Y. & Park, N.-G. Quasi-Two-Dimensional Perovskite Solar Cells with Efficiency Exceeding 22%. *ACS Energy Lett.* **7**, 757–765 (2022).

77. Yang, Y., Gao, F., Gao, S. & Wei, S.-H. Origin of the stability of two-dimensional perovskites: a first-principles study. *J. Mater. Chem. A* **6**, 14949–14955 (2018).

78. Kim, G. Y. *et al.* Large tunable photoeffect on ion conduction in halide perovskites and implications for photodecomposition. *Nature Mater* **17**, 445–449 (2018).

79. Wang, C., Ecker, B. R., Wei, H., Huang, J. & Gao, Y. Environmental Surface Stability of the $MAPbBr_3$ Single Crystal. *J. Phys. Chem. C* **122**, 3513–3522 (2018).

80. Slotcavage, D. J., Karunadasa, H. I. & McGehee, M. D. Light-Induced Phase Segregation in Halide-Perovskite Absorbers. *ACS Energy Lett.* **1**, 1199–1205 (2016).

81. Khenkin, M. V., K. M., A., Katz, E. A. & Visoly-Fisher, I. Bias-dependent degradation of various solar cells: lessons for stability of perovskite photovoltaics. *Energy Environ. Sci.* **12**, 550–558 (2019).

82. Razera, R. A. Z. *et al.* Instability of p–i–n perovskite solar cells under reverse bias. *J. Mater. Chem. A* **8**, 242–250 (2020).

83. Ni, Z. *et al.* Evolution of defects during the degradation of metal halide perovskite solar cells under reverse bias and illumination. *Nat Energy* **7**, 65–73 (2022).

84. Blood, P. & Orton, J. W. *The Electrical Characterization of Semiconductors: Majority and Minority Carriers*. (1992).

85. Balland, J. C., Zielinger, J. P., Noguet, C. & Tapiero, M. Investigation of deep levels in high-resistivity bulk materials by photo-induced current transient spectroscopy: I. Review and analysis of some basic problems. 15.

86. Balland, J. C., Zielinger, J. P., Tapiero, M., Gross, J. G. & Noguet, C. Investigation of deep levels in high-resistivity bulk materials by photo-induced current transient spectroscopy. II. Evaluation of various signal processing methods. *J. Phys. D: Appl. Phys.* **19**, 71–87 (1986).

87. Jin, H. *et al.* It's a trap! On the nature of localised states and charge trapping in lead halide perovskites. *Mater. Horiz.* **7**, 397–410 (2020).

88. Meggiolaro, D. *et al.* Iodine chemistry determines the defect tolerance of lead-halide perovskites. *Energy Environ. Sci.* **11**, 702–713 (2018).

89. Motti, S. G. *et al.* Defect Activity in Lead Halide Perovskites. *Advanced Materials* **31**, 1901183 (2019).

90. Yin, J. *et al.* Modulation of Broadband Emissions in Two-Dimensional ⟨100⟩-Oriented Ruddlesden–Popper Hybrid Perovskites. *ACS Energy Lett.* **5**, 2149–2155 (2020).

91. Keeble, D. J. *et al.* Identification of lead vacancy defects in lead halide perovskites. *Nat Commun* **12**, 5566 (2021).

92. Ni, Z. *et al.* Resolving spatial and energetic distributions of trap states in metal halide perovskite solar cells. *Science* **367**, 1352–1358 (2020).

93. Siekmann, J., Ravishankar, S. & Kirchartz, T. Apparent Defect Densities in Halide Perovskite Thin Films and Single Crystals. *ACS Energy Lett.* **6**, 3244–3251 (2021).

94. Peters, J. A., Liu, Z., De Siena, M. C., Kanatzidis, M. G. & Wessels, B. W. Defect levels in $CsPbCl_3$ single crystals determined by thermally stimulated current spectroscopy. *Journal of Applied Physics* **132**, 035101 (2022).

95. Musiienko, A. *et al.* Defects in Hybrid Perovskites: The Secret of Efficient Charge Transport. *Adv. Funct. Mater.* 2104467 (2021) doi:10.1002/adfm.202104467.

96. Cho, S. H. *et al.* Investigation of Defect-Tolerant Perovskite Solar Cells with Long-Term Stability via Controlling the Self-Doping Effect. *Adv. Energy Mater.* **11**, 2100555 (2021).

97. Polyakov, A. Y. *et al.* Trap states in multication mesoscopic perovskite solar cells: A deep levels transient spectroscopy investigation. *Appl. Phys. Lett.* **113**, 263501 (2018).

98. Pecunia, V. *et al.* Assessing the Impact of Defects on Lead-Free Perovskite-Inspired Photovoltaics via Photoinduced Current Transient Spectroscopy. *Adv. Energy Mater.* 15 (2021).

99. Li, J. V. Deep level transient spectroscopy characterization without the Arrhenius plot. *Review of Scientific Instruments* **92**, 023902 (2021).

100. Šantić, B. & Desnica, U. V. Thermoelectric effect spectroscopy of deep levels—application to semi-insulating GaAs. *Appl. Phys. Lett.* **56**, 2636–2638 (1990).

101. Fraboni, B., Cavalcoli, D., Cavallini, A. & Fochuk, P. Electrical activity of deep traps in high resistivity CdTe: Spectroscopic characterization. *Journal of Applied Physics* **105**, 073705 (2009).

102. Tapiero, M., Benjelloun, N., Zielinger, J. P., El Hamd, S. & Noguet, C. Photoinduced current transient spectroscopy in high-resistivity bulk materials: Instrumentation and methodology. *Journal of Applied Physics* **64**, 4006–4012 (1988).

103. Castaldini, A., Cavallini, A., Fraboni, B., Fernandez, P. & Piqueras, J. Deep energy levels in CdTe and CdZnTe. *Journal of Applied Physics* **83**, 2121–2126 (1998).

104. Mathew, X. Photo-induced current transient spectroscopic study of the traps in CdTe. *Solar Energy Materials and Solar Cells* **76**, 225–242 (2003).

105. Reichert, S. *et al.* Ionic-Defect Distribution Revealed by Improved Evaluation of Deep-Level Transient Spectroscopy on Perovskite Solar Cells. *Phys. Rev. Applied* **13**, 034018 (2020).

106. Reichert, S. *et al.* Probing the ionic defect landscape in halide perovskite solar cells. *Nat Commun* **11**, 6098 (2020).

107. Teng, P. *et al.* Degradation and self-repairing in perovskite light-emitting diodes. *Matter* **4**, 3710–3724 (2021).

108. Karlsson, M. *et al.* Mixed halide perovskites for spectrally stable and high-efficiency blue light-emitting diodes. *Nat Commun* **12**, 361 (2021).

109. Futscher, M. H., Gangishetty, M. K., Congreve, D. N. & Ehrler, B. Quantifying mobile ions and electronic defects in perovskite-based devices with temperature-dependent capacitance measurements: Frequency vs time domain. *J. Chem. Phys.* **152**, 044202 (2020).

110. Futscher, M. H., Gangishetty, M. K., Congreve, D. N. & Ehrler, B. Manganese Doping Stabilizes Perovskite Light-Emitting Diodes by Reducing Ion Migration. *ACS Appl. Electron. Mater.* **2**, 1522–1528 (2020).

111. McGovern, L., Futscher, M. H., Muscarella, L. A. & Ehrler, B. Understanding the Stability of MAPbBr $_3$ versus MAPbI $_3$: Suppression of Methylammonium Migration and Reduction of Halide Migration. *J. Phys. Chem. Lett.* **11**, 7127–7132 (2020).

112. Heiser, T. & Mesli, A. Determination of the copper diffusion coefficient in silicon from transient ion-drift. *Appl. Phys. A* **57**, 325–328 (1993).

113. Lyubomirsky, I., Rabinal, M. K. & Cahen, D. Room-temperature detection of mobile impurities in compound semiconductors by transient ion drift. *Journal of Applied Physics* **81**, 6684–6691 (1997).

114. Shikoh, A. S. *et al.* On the relation between mobile ion kinetics, device design, and doping in double-cation perovskite solar cells. *Appl. Phys. Lett.* **118**, 093501 (2021).

115. Li, B. *et al.* Understanding the Influence of Cation and Anion Migration on Mixed-Composition Perovskite Solar Cells via Transient Ion Drift. *Physica Rapid Research Ltrs* **15**, 2100225 (2021).

116. Shikoh, A. S. *et al.* Assessing mobile ions contributions to admittance spectra and current-voltage characteristics of 3D and 2D/3D perovskite solar cells. *Solar Energy Materials and Solar Cells* **215**, 110670 (2020).

117. Urbaniak, A., Czudek, A., Dagar, J. & Unger, E. L. Capacitance spectroscopy of thin-film formamidinium lead iodide based perovskite solar cells. *Solar Energy Materials and Solar Cells* **238**, 111618 (2022).

118. Swartz, C. H., Khakurel, N., Najar, S. R., Hossain, M. I. & Zakhidov, A. Temperature- and Bias-Dependent Degradation and Regeneration of Perovskite Solar Cells with Organic and Inorganic Hole Transport Layers. *Phys. Status Solidi A* **218**, 2000721 (2021).

119. Heo, S. *et al.* Enhancement of Piezoelectricity in Dimensionally Engineered Metal-Halide Perovskites Induced by Deep Level Defects. *Advanced Energy Materials* 2200181 (2022) doi:10.1002/aenm.202200181.

120. Ono, L. K., Liu, S. (Frank) & Qi, Y. Reducing Detrimental Defects for High-Performance Metal Halide Perovskite Solar Cells. *Angew. Chem. Int. Ed.* **59**, 6676–6698 (2020).

121. Futscher, M. H. & Deibel, C. Defect Spectroscopy in Halide Perovskites Is Dominated by Ionic Rather than Electronic Defects. *ACS Energy Lett.* **7**, 140–144 (2022).

122. Min, H. *et al.* Perovskite solar cells with atomically coherent interlayers on SnO2 electrodes. *Nature* **598**, 444–450 (2021).

123. Hou, Y. *et al.* Efficient tandem solar cells with solution-processed perovskite on textured crystalline silicon. *Science* **367**, 1135–1140 (2020).

124. Hou, Y. *et al.* Self-Powered Red/UV Narrowband Photodetector by Unbalanced Charge Carrier Transport Strategy. *Adv. Funct. Mater.* **31**, 2007016 (2021).

125. Hu, M. *et al.* Large and Dense Organic–Inorganic Hybrid Perovskite $CH_3NH_3PbI_3$ Wafer Fabricated by One-Step Reactive Direct Wafer Production with High X-ray Sensitivity. *ACS Appl. Mater. Interfaces* **12**, 16592–16600 (2020).

126. Dong, R. *et al.* High-Gain and Low-Driving-Voltage Photodetectors Based on Organolead Triiodide Perovskites. *Advanced Materials* **27**, 1912–1918 (2015).

127. Li, Y. *et al.* Defective TiO2 with high photoconductive gain for efficient and stable planar heterojunction perovskite solar cells. *Nat Commun* **7**, 12446 (2016).

128. Lédée, F., Ciavatti, A., Verdi, M., Basiricò, L. & Fraboni, B. Ultra-Stable and Robust Response to X-Rays in 2D Layered Perovskite Micro-Crystalline Films Directly Deposited on Flexible Substrate. *Advanced Optical Materials* **10**, 2101145 (2022).

129. Saidaminov, M. I. *et al.* High-quality bulk hybrid perovskite single crystals within minutes by inverse temperature crystallization. *Nat Commun* **6**, 7586 (2015).

130. Amari, S., Verilhac, J.-M., Gros D’Aillon, E., Ibanez, A. & Zaccaro, J. Optimization of the Growth Conditions for High Quality $CH_3NH_3PbBr_3$ Hybrid Perovskite Single Crystals. *Crystal Growth & Design* **20**, 1665–1672 (2020).

131. Metallography by PRESI: Analysis and Metallographic section. *Presi* https://www.presi.com/.

132. García-Batlle, M. *et al.* Moving Ions Vary Electronic Conductivity in Lead Bromide Perovskite Single Crystals through Dynamic Doping. *Adv. Electron. Mater.* **6**, 2000485 (2020).

133. Passarelli, J. V. *et al.* Enhanced Out-of-Plane Conductivity and Photovoltaic Performance in n = 1 Layered Perovskites through Organic Cation Design. *J. Am. Chem. Soc.* **140**, 7313–7323 (2018).

134. Cavalcoli, D. & Fazio, M. A. Electronic transitions in low dimensional semiconductor structures measured by surface photovoltage spectroscopy. *Materials Science in Semiconductor Processing* **92**, 28–38 (2019).

135. *Radiation oncology physics: a handbook for teachers and students*. (International Atomic Energy Agency, 2005).

136. Ikossi-Anastasiou, K. & Roenker, K. P. Refinements in the method of moments for analysis of multiexponential capacitance transients in deep-level transient spectroscopy. *Journal of Applied Physics* **61**, 182–190 (1987).

137. Kirchner, P. D. *et al.* The analysis of exponential and nonexponential transients in deep-level transient spectroscopy. *Journal of Applied Physics* **52**, 6462–6470 (1981).

138. McGovern, L. *et al.* Reduced Barrier for Ion Migration in Mixed-Halide Perovskites. *ACS Appl. Energy Mater.* **4**, 13431–13437 (2021).

139. Xu, Q. *et al.* Effect of methylammonium lead tribromide perovskite based-photoconductor under gamma photons radiation. *Radiation Physics and Chemistry* **181**, 109337 (2021).

140. Syafutra, H. *et al.* Surface Degradation Mechanism on CH3NH3PbBr3 Hybrid Perovskite Single Crystal by a Grazing E-Beam Irradiation. *Nanomaterials* **10**, 1253 (2020).

141. Yang, S. *et al.* Organohalide Lead Perovskites: More Stable than Glass under Gamma-Ray Radiation. *Adv. Mater.* **31**, 1805547 (2019).

142. Boldyreva, A. G. *et al.* Unravelling the Material Composition Effects on the Gamma Ray Stability of Lead Halide Perovskite Solar Cells: MAPbI $_3$ Breaks the Records. *J. Phys. Chem. Lett.* **11**, 2630–2636 (2020).

143. Mariano, F. The enhancement of excitonic emission crossing Saha equilibrium in trap passivated CH3NH3PbBr3 perovskite. *Communications Physics* 10 (2020) doi:https://doi.org/10.1038/s42005-020-0309-3.

144. Shi, J. *et al.* Identification of high-temperature exciton states and their phase-dependent trapping behaviour in lead halide perovskites. *Energy Environ. Sci.* **11**, 1460–1469 (2018).

145. Sestu, N. *et al.* Absorption F-Sum Rule for the Exciton Binding Energy in Methylammonium Lead Halide Perovskites. *J. Phys. Chem. Lett.* **6**, 4566–4572 (2015).

146. Elliott, R. J. Intensity of Optical Absorption by Excitons. *Phys. Rev.* **108**, 1384–1389 (1957).

147. Mannino, G. *et al.* Temperature-Dependent Optical Band Gap in $CsPbBr_3$, $MAPbBr_3$, and $FAPbBr_3$ Single Crystals. *J. Phys. Chem. Lett.* **11**, 2490–2496 (2020).

148. Meggiolaro, D., Ambrosio, F., Mosconi, E., Mahata, A. & De Angelis, F. Polarons in Metal Halide Perovskites. *Adv. Energy Mater.* **10**, 1902748 (2020).

149. Droseros, N., Tsokkou, D. & Banerji, N. Photophysics of Methylammonium Lead Tribromide Perovskite: Free Carriers, Excitons, and Sub-Bandgap States. *Adv. Energy Mater.* **10**, 1903258 (2020).

150. Tanuma, S., Powell, C. J. & Penn, D. R. Calculations of electron inelastic mean free paths. V. Data for 14 organic compounds over the 50-2000 eV range. *Surf. Interface Anal.* **21**, 165–176 (1994).

151. Nguyen-Truong, H. T. Low-energy electron inelastic mean free path in materials. *Appl. Phys. Lett.* **108**, 172901 (2016).

152. Sadoughi, G. *et al.* Observation and Mediation of the Presence of Metallic Lead in Organic–Inorganic Perovskite Films. *ACS Appl. Mater. Interfaces* **7**, 13440–13444 (2015).

153. Aristidou, N. *et al.* Fast oxygen diffusion and iodide defects mediate oxygen-induced degradation of perovskite solar cells. *Nat Commun* **8**, 15218 (2017).

154. Shin, D. *et al.* Mechanism and Timescales of Reversible p-Doping of Methylammonium Lead Triiodide by Oxygen. *Adv. Mater.* **33**, 2100211 (2021).

155. Anusca, I. *et al.* Dielectric Response: Answer to Many Questions in the Methylammonium Lead Halide Solar Cell Absorbers. *Adv. Energy Mater.* **7**, 1700600 (2017).

156. Sendner, M. *et al.* Optical phonons in methylammonium lead halide perovskites and implications for charge transport. *Mater. Horiz.* **3**, 613–620 (2016).

157. Galkowski, K. *et al.* Determination of the exciton binding energy and effective masses for methylammonium and formamidinium lead tri-halide perovskite semiconductors. *Energy Environ. Sci.* **9**, 962–970 (2016).

158. Aydin, E. *et al.* Interplay between temperature and bandgap energies on the outdoor performance of perovskite/silicon tandem solar cells. *Nat Energy* **5**, 851–859 (2020).

159. Al-Ashouri, A. *et al.* Monolithic perovskite/silicon tandem solar cell with >29% efficiency by enhanced hole extraction. *Science* **370**, 1300–1309 (2020).

160. De Bastiani, M. *et al.* Efficient bifacial monolithic perovskite/silicon tandem solar cells via bandgap engineering. *Nat Energy* **6**, 167–175 (2021).

161. Isikgor, F. H. *et al.* Concurrent cationic and anionic perovskite defect passivation enables 27.4% perovskite/silicon tandems with suppression of halide segregation. *Joule* **5**, 1566–1586 (2021).

162. Aydin, E. *et al.* Ligand-bridged charge extraction and enhanced quantum efficiency enable efficient n–i–p perovskite/silicon tandem solar cells. *Energy Environ. Sci.* **14**, 4377–4390 (2021).

163. De Bastiani, M. *et al.* All Set for Efficient and Reliable Perovskite/Silicon Tandem Photovoltaic Modules? *Solar RRL* **6**, 2100493 (2022).

164. Rolston, N. *et al.* Mechanical integrity of solution-processed perovskite solar cells. *Extreme Mechanics Letters* **9**, 353–358 (2016).

165. Bush, K. A. *et al.* Controlling Thin-Film Stress and Wrinkling during Perovskite Film Formation. *ACS Energy Lett.* **3**, 1225–1232 (2018).

166. Hu, H. *et al.* Molecular engineering of two-dimensional hybrid perovskites with broadband emission for white light-emitting diodes. *Journal of Materials Chemistry C* **6**, 10301–10307 (2018).

167. Wang, Z. *et al.* Efficient Green Quasi-Two-Dimensional Perovskite Light-Emitting Diodes Based on Mix-Interlayer. *Frontiers in Chemistry* **9**, (2022).

168. Ji, C. *et al.* 2D Hybrid Perovskite Ferroelectric Enables Highly Sensitive X-Ray Detection with Low Driving Voltage. *Adv. Funct. Mater.* **30**, 1905529 (2020).

169. Zhang, Y. *et al.* Two-dimensional (PEA)2PbBr4 perovskite single crystals for a high performance UV-detector. *J. Mater. Chem. C* **7**, 1584–1591 (2019).

170. Wu, G. *et al.* Surface Passivation Using 2D Perovskites toward Efficient and Stable Perovskite Solar Cells. *Advanced Materials* **34**, 2105635 (2022).

171. Heo, S. *et al.* Dimensionally Engineered Perovskite Heterostructure for Photovoltaic and Optoelectronic Applications. *Advanced Energy Materials* **9**, 1902470 (2019).

172. Blancon, J.-C. *et al.* Extremely efficient internal exciton dissociation through edge states in layered 2D perovskites. *Science* **355**, 1288–1292 (2017).

173. Kerner, R. A. *et al.* Low Threshold Voltages Electrochemically Drive Gold Migration in Halide Perovskite Devices. *ACS Energy Lett.* **5**, 3352–3356 (2020).

174. Besleaga, C. *et al.* Iodine Migration and Degradation of Perovskite Solar Cells Enhanced by Metallic Electrodes. *J. Phys. Chem. Lett.* **7**, 5168–5175 (2016).

175. Baussens, O. *et al.* An insight into the charge carriers transport properties and electric field distribution of $CH_3NH_3PbBr_3$ thick single crystals. *Appl. Phys. Lett.* **117**, 041904 (2020).

176. García-Batlle, M. *et al.* Coupling between Ion Drift and Kinetics of Electronic Current Transients in $MAPbBr_3$ Single Crystals. *ACS Energy Lett.* **7**, 946–951 (2022).

177. Liu, X. *et al.* Charge Transport Behavior in Solution-Grown Methylammonium Lead Tribromide Perovskite Single Crystal Using α Particles. *J. Phys. Chem. C* **122**, 14355–14361 (2018).

178. Mahapatra, A. *et al.* Reducing ion migration in methylammonium lead tri-bromide single crystal via lead sulfate passivation. *Journal of Applied Physics* **127**, 185501 (2020).

179. Brasil, M. J. S. P. & Motisuke, P. Deep center characterization by photo-induced transient spectroscopy. *Journal of Applied Physics* **68**, 3370–3376 (1990).

180. Murali, B. *et al.* Single Crystals: The Next Big Wave of Perovskite Optoelectronics. *ACS Materials Lett.* **2**, 184–214 (2020).

181. Wei, H. *et al.* Sensitive X-ray detectors made of methylammonium lead tribromide perovskite single crystals. *Nature Photon* **10**, 333–339 (2016).

182. Ceratti, D. R. *et al.* Eppur si Muove: Proton Diffusion in Halide Perovskite Single Crystals. *Adv. Mater.* **32**, 2002467 (2020).

183. Wang, H., Guerrero, A., Bou, A., Al-Mayouf, A. M. & Bisquert, J. Kinetic and material properties of interfaces governing slow response and long timescale phenomena in perovskite solar cells. *Energy Environ. Sci.* **12**, 2054–2079 (2019).

184. Shrestha, S. *et al.* Role of the Metal–Semiconductor Interface in Halide Perovskite Devices for Radiation Photon Counting. *ACS Appl. Mater. Interfaces* **12**, 45533–45540 (2020).

185. Ahmadi, M. *et al.* Spatially Resolved Carrier Dynamics at $MAPbBr_3$ Single Crystal–Electrode Interface. *ACS Appl. Mater. Interfaces* **11**, 41551–41560 (2019).

186. Moia, D. *et al.* Ionic-to-electronic current amplification in hybrid perovskite solar cells: ionically gated transistor-interface circuit model explains hysteresis and impedance of mixed conducting devices. *Energy Environ. Sci.* **12**, 1296–1308 (2019).

187. Chen, B. *et al.* Impact of Capacitive Effect and Ion Migration on the Hysteretic Behavior of Perovskite Solar Cells. *J. Phys. Chem. Lett.* **6**, 4693–4700 (2015).

188. Yang, T.-Y., Gregori, G., Pellet, N., Grätzel, M. & Maier, J. The Significance of Ion Conduction in a Hybrid Organic-Inorganic Lead-Iodide-Based Perovskite Photosensitizer. *Angew. Chem.* **127**, 8016–8021 (2015).

189. McGovern, L., Koschany, I., Grimaldi, G., Muscarella, L. A. & Ehrler, B. Grain Size Influences Activation Energy and Migration Pathways in $MAPbBr_3$ Perovskite Solar Cells. *J. Phys. Chem. Lett.* **12**, 2423–2428 (2021).

190. Tammireddy, S. *et al.* Temperature-Dependent Ionic Conductivity and Properties of Iodine-Related Defects in Metal Halide Perovskites. *ACS Energy Lett.* **7**, 310–319 (2022).

191. Wei, J. *et al.* Mechanisms and Suppression of Photoinduced Degradation in Perovskite Solar Cells. *Adv. Energy Mater.* **11**, 2002326 (2021).

192. Huang, L., Ge, Z., Zhang, X. & Zhu, Y. Oxygen-induced defect-healing and photo-brightening of halide perovskite semiconductors: science and application. *J. Mater. Chem. A* **9**, 4379–4414 (2021).

193. Brenes, R., Eames, C., Bulović, V., Islam, M. S. & Stranks, S. D. The Impact of Atmosphere on the Local Luminescence Properties of Metal Halide Perovskite Grains. *Adv. Mater.* **30**, 1706208 (2018).

194. Song, Z. *et al.* Impact of Moisture on Photoexcited Charge Carrier Dynamics in Methylammonium Lead Halide Perovskites. *J. Phys. Chem. Lett.* **9**, 6312–6320 (2018).

195. Motti, S. G. *et al.* Photoinduced Emissive Trap States in Lead Halide Perovskite Semiconductors. *ACS Energy Lett.* **1**, 726–730 (2016).

196. Wang, Q. *et al.* Scaling behavior of moisture-induced grain degradation in polycrystalline hybrid perovskite thin films. *Energy Environ. Sci.* **10**, 516–522 (2017).

197. Fang, H.-H. *et al.* Ultrahigh sensitivity of methylammonium lead tribromide perovskite single crystals to environmental gases. *Sci. Adv.* **2**, e1600534 (2016).

198. Almora, O. *et al.* Surface versus Bulk Currents and Ionic Space-Charge Effects in $CsPbBr_3$ Single Crystals. *J. Phys. Chem. Lett.* **13**, 3824–3830 (2022).

199. Long, R., Fang, W. & Prezhdo, Oleg. V. Moderate Humidity Delays Electron–Hole Recombination in Hybrid Organic–Inorganic Perovskites: Time-Domain Ab Initio Simulations Rationalize Experiments. *J. Phys. Chem. Lett.* **7**, 3215–3222 (2016).

200. Kye, Y.-H., Yu, C.-J., Jong, U.-G., Chen, Y. & Walsh, A. Critical Role of Water in Defect Aggregation and Chemical Degradation of Perovskite Solar Cells. *J. Phys. Chem. Lett.* **9**, 2196–2201 (2018).

201. Zhu, Z. *et al.* Interaction of Organic Cation with Water Molecule in Perovskite $MAPbI_3$: From Dynamic Orientational Disorder to Hydrogen Bonding. *Chem. Mater.* **28**, 7385–7393 (2016).

202. Gan, Z., Yu, Z., Meng, M., Xia, W. & Zhang, X. Hydration of mixed halide perovskites investigated by Fourier transform infrared spectroscopy. *APL Materials* **7**, 031107 (2019).

203. Li, G. *et al.* Stable fluorescent NH3 sensor based on MAPbBr3 encapsulated by tetrabutylammonium cations. *Journal of Alloys and Compounds* **835**, 155386 (2020).

204. Mannino, G. *et al.* $CsPbBr_3$, $MAPbBr_3$, and $FAPbBr_3$ Bromide Perovskite Single Crystals: Interband Critical Points under Dry N_2 and Optical Degradation under Humid Air. *J. Phys. Chem. C* **125**, 4938–4945 (2021).

205. Ryu, H. *et al.* Static Rashba Effect by Surface Reconstruction and Photon Recycling in the Dynamic Indirect Gap of $APbBr_3$ (A = Cs, CH_3NH_3) Single Crystals. *J. Am. Chem. Soc.* **142**, 21059–21067 (2020).

206. Schötz, K. *et al.* Double peak emission in lead halide perovskites by self-absorption. *J. Mater. Chem. C* **8**, 2289–2300 (2020).

207. Glaser, T. *et al.* Infrared Spectroscopic Study of Vibrational Modes in Methylammonium Lead Halide Perovskites. *J. Phys. Chem. Lett.* **6**, 2913–2918 (2015).

208. Fan, Z. *et al.* Solution-Processed $MAPbBr_3$ and $CsPbBr_3$ Single-Crystal Detectors with Improved X-Ray Sensitivity via Interfacial Engineering. *Phys. Status Solidi A* **217**, 2000104 (2020).

209. Attique, S. *et al.* Aqueous phase fabrication and conversion of Pb(OH)Br into a $CH_3NH_3PbBr_3$ perovskite and its application in resistive memory switching devices. *Green Chem.* **22**, 3608–3614 (2020).

210. Provis-Evans, C. B., Farrar, E. H. E., Grayson, M. N., Webster, R. L. & Hill, A. K. Highly Sensitive Real-Time Isotopic Quantification of Water by ATR-FTIR. *Anal. Chem.* **92**, 7500–7507 (2020).

211. Mitchell, S. Thermogravimetric Analysis (TGA–FTIR). *EAG Laboratories* https://www.eag.com/app-note/thermogravimetric-analysis-tga-ftir/ (2019).

212. Levasseur, A., Vinatier, P. & Gonbeau, D. X-ray photoelectron spectroscopy: A powerful tool for a better characterization of thin film materials. *Bull Mater Sci* **22**, 607–614 (1999).

213. Dan, Y., Zhao, X., Chen, K. & Mesli, A. A Photoconductor Intrinsically Has No Gain. *ACS Photonics* **5**, 4111–4116 (2018).

214. Wang, Y. *et al.* Hybrid Graphene–Perovskite Phototransistors with Ultrahigh Responsivity and Gain. *Advanced Optical Materials* **3**, 1389–1396 (2015).

Acknowledgements

One of the most haunting doubts that PhD students face is: “In my thesis, should I use the first person singular or plural?”. On one side, it was *me* writing the thesis, and *me* doing most part of the work. On the other side, modern research is not feasible if not in a team, and none of the results of this thesis would have been achieved without the help and collaboration from my colleagues. This might have resulted in a confused use of “I” and “we” throughout my thesis, and I apologize for this with the readers. In the following, I acknowledge all the colleagues and friends who helped and supported me throughout these years.

First, I thank Prof. Daniela Cavalcoli, my supervisor, for her guidance during these three years. She always supported me, leaving me free of experimenting, while helping me remain on the right track. I thank Prof. Beatrice Fraboni, who always supported my work, and gave me precious advice about the research directions to follow. I thank Prof. Tobias Cramer for the help with the KPFM experiments on tandem solar cells, for the interesting project on dpiX samples, and for the fruitful discussions about the interpretation of the PICTS results. I thank Laura Ferlauto, who accompanied me during the first part of my PhD, and was a precious friend and collaborator. I wish you good luck with your new career, and a happy life with your family. I thank Lorenzo Maserati, my companion for the last part of the PhD. I had a great time with you, both inside and out of the lab. You are an excellent researcher, and I’m sure you will have a great career, you deserve it. I thank Andrea Ciavatti for his patience and for the great help he gave me in the lab as well as in the interpretation of the results. I thank Alberto Piccioni and Pierpaolo Vecchi for the help and collaboration on the IMPS measurements on perovskite single crystals, which, unfortunately, I could not include in this thesis. Finally, I thank Maria Calienni and Marta Tessarolo for giving me all the technical support I needed for my work.

Moving to my exchange period in Grenoble, I thank Julien Zaccaro for accepting me in his research group, and supervising me during my activity at Institut Néel. I also thank Eric Gros d'Aillon and Jean-Marie Verilhac from the CEA of Grenoble, who always gave precious advice on the research directions to follow. I thank Ferdinand Lédée, my friend and colleague with whom I had the pleasure to spend time inside and out of the lab, both in Bologna and Grenoble. I thank Javier Mayén, my wingman during the exchange in Grenoble, it was a pleasure to work with you, but, most importantly, to spend time with you at dinners, hikes, and concerts. I thank Thibault Lemercier, who was always there for practical advice in the lab, and for having fun outside the lab. I will never forget your great *tartiflette*. I also thank the other people who made unforgettable my experience in Grenoble: Marian, Kylia, Mackrine, Maxime, Baptiste, and all the other guys from Institut Néel.

Among the external collaborators, I thank Francesco Borgatti, Alessandro Kovtun, Silvia Milita, and Gabriele Calabrese from the CNR of Bologna for the fruitful collaboration on the investigation of the effects of ionizing radiation on the optoelectronic properties of perovskite single crystals. I thank Michele De Bastiani and all other researchers from the KAUST Solar Center in Saudi Arabia for the fruitful collaboration on the investigation of the delamination effect in perovskite/Si tandem solar cells.

Last, but not least, I thank all the students who spent some time working in the lab with me during their internships. I thank Pierpaolo Vecchi, Matilde Lini, Vito Foderà, Martina Foschi, Matias Feldman, Camille Radelet, Valentina Van Der Meer, Marco Bocconi, Bernardo Maraldi, Enrico Pedretti, Lorenzo Bramucci, Daniela Mangano, and Luca Domeniconi. Your efforts were essential to the fulfilment of this thesis work.

Moving to my dear friends and colleagues at DIFA. First and foremost, a big thank you to Matteo Verdi, my companion for over 7 years during the bachelor, master, and PhD. We shared everything, from the happiest moments to the most frustrating ones. Our friendship will continue, even if we are a bit farther away from each other now. A thank you to "la vecchia guardia" of DIFA: Francesco, Alberto, Ilaria, Poss, Leo, Luca B., Filippo, Pierpaolo, and Jonathan. Your presence made my experience at DIFA a real pleasure. You were always there for having fun, but also to give me a hand when I needed it. A thank you, and a big "good luck" to "la nuova guardia" of DIFA: Irene, Lorenzo, Matteo, Lia, Camilla, Luca F., and Marco. I can see you are all talented young researchers, and I wish you to enjoy your PhD years as much as I did.

Un grande grazie va alla mia famiglia, che mi ha sempre supportato per tutto il corso dei miei studi, da quando ero un bambino sino ad ora, al più alto livello dell'educazione. Probabilmente non riuscirò mai a ringraziarvi abbastanza per tutto ciò che avete fatto per me.

Ti lascio per ultima, ma sai che sei la più importante. Grazie, Cate, per essere sempre stata al mio fianco. Per avermi sopportato nei momenti più complicati, e per avermi fatto distrarre quando ne avevo bisogno. È incredibile quanto sia cambiata la nostra vita in questi tre anni, e non vedo l’ora di vedere come andrà da ora in poi.